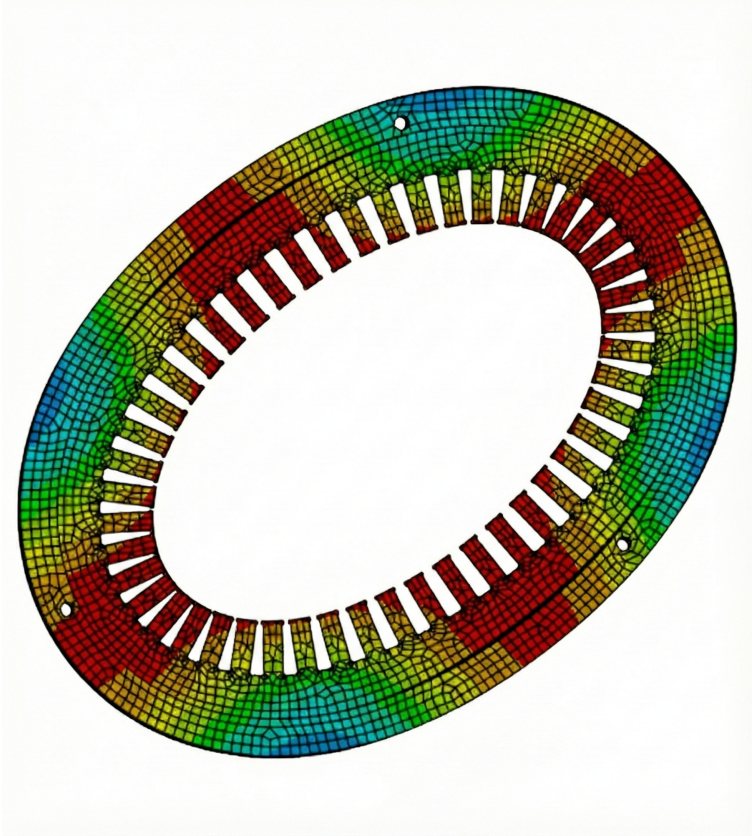

Modeling of Teeth Forces in Electrical Machines

A Comparison between different types of machines

Entong Liu

DEPARTMENT OF ELECTRICAL ENGINEERING

CHALMERS UNIVERSITY OF TECHNOLOGY
Gothenburg, Sweden 2026
www.chalmers.se

Degree project report 2026

Modeling of Teeth Forces in Electrical Machines

A Comparison Between Different Types of Machines

Entong Liu

CHALMERS
UNIVERSITY OF TECHNOLOGY

Department of Electrical Engineering
Division of Electric Power Engineering
Chalmers University of Technology
Gothenburg, Sweden 2026

Modeling of Teeth Forces in Electrical Machines
A Comparison between Different Types of Machines
Entong Liu

Supervisor: Qixuan Wang, Electric Power Engineering,
Joachim Härsjö, Volvo Cars Corporation
Examiner: Torbjörn Thiringer, Electric Power Engineering

Degree project report 2026
Department of Electrical Engineering
Chalmers University of Technology
SE-412 96 Gothenburg
Sweden
Telephone +46 31 772 1000

Cover: Modal analysis of a contact structure of stator and housing showing total deformation caused by radial forces of 2nd spatial order.

Typeset in LaTeX
Gothenburg, Sweden 2026

Modeling of Teeth Forces in Electrical Machines
A Comparison between Different Types of Machines
ENTONG LIU
Department of Electrical Engineering
Chalmers University of Technology

Abstract

Electromagnetic forces are the primary excitation sources of vibration and noise in electrical machines. Their generation mechanisms and transmission processes are closely related to pole–slot combinations, winding configurations, and structural characteristics of the machine. This thesis investigates permanent-magnet synchronous machines (PMSMs) with different pole–slot configurations, focusing on the characteristics of electromagnetic (EM) forces and their associated vibration and noise mechanisms. A comparative study is conducted between an integral-slot distributed-winding interior permanent-magnet synchronous machine (ISDW IPMSM) and fractional-slot concentrated-winding surface-mounted permanent-magnet synchronous machines (FSCW SPMSMs), highlighting their differences in electromagnetic fields, electromagnetic forces, torque ripple, and vibro-acoustic performance.

First, from a theoretical perspective, analytical models of radial and tangential air-gap electromagnetic fields and electromagnetic forces are established under both slotless and slotted conditions. The influence of different pole–slot combinations on air-gap flux density distributions and the spatio-temporal harmonic characteristics of electromagnetic forces is systematically analyzed. Based on these models, the effects of electromagnetic forces on cogging torque and load torque ripple in different machines are investigated, clarifying the impact of pole–slot combinations on torque performance.

Second, to address the discontinuous nature of force transmission from air-gap electromagnetic forces to stator tooth forces, a theoretical model of the mechanical modulation effect of stator teeth is developed. By analyzing the force transmission process from the perspectives of distributed forces and concentrated forces, the sampling and modulation characteristics exhibited by stator teeth during force transformation are revealed. The differences of this effect among various machine structures and its role in reshaping the tooth force spectrum are also clarified.

In terms of numerical simulations, two-dimensional (2D) finite-element electromagnetic simulations are employed to obtain electromagnetic field distributions, electromagnetic force waves, and torque characteristics under no-load and load conditions. Three-dimensional (3D) finite-element models are used to perform modal analysis of the stator and housing, yielding their natural frequencies and mode shapes. Furthermore, the electromagnetic forces obtained from 2D simulations are mapped onto 3D structural models to conduct coupled multiphysics harmonic response analyses.

Equivalent radiated power (ERP) is used to evaluate vibration and noise responses over the entire operating speed range.

Finally, by combining modal analysis and harmonic response results, the generation mechanisms and evolution of vibration and noise in PMSMs with different pole–slot configurations over the full speed range are systematically elucidated. The dominant electromagnetic force components and their coupling with structural modes are identified. This thesis establishes a complete physical chain from electromagnetic force generation, through stator tooth mechanical modulation, to structural vibration and noise radiation, providing theoretical foundations and engineering guidance for the low-vibration and low-noise design of PMSMs with different pole–slot combinations.

Keywords: Electromagnetic force, Pole–slot combination, DW IPMSM, FSCW SPMSM, Torque ripple, Stator tooth mechanical modulation, Air-gap flux density, Vibro-acoustic analysis, Harmonic response.

Acknowledgements

I would like to express my sincere gratitude to my supervisor at Chalmers, PhD student Qixuan Wang, for clearly defining the research topic and direction of this work. His guidance was instrumental in helping me become familiar with the research field, develop simulation and experimental skills, and navigate the project effectively. I am deeply grateful for his professional advice, patience, and comprehensive support throughout the study.

I would also like to thank my supervisor at Volvo Cars, Joachim Härsjö, for his kindness and insightful discussions. His valuable input from an industrial perspective greatly enhanced my understanding of practical engineering problems and the industrial environment.

My sincere appreciation goes to the examiner, Professor Torbjörn Thiringer, who consistently took time from his busy schedule to follow the progress of this work. His professional guidance and constructive suggestions on both simulation and academic writing were invaluable, and his support greatly facilitated my studies at Chalmers.

I would like to thank all my friends at Chalmers for sharing both challenges and joyful moments during this journey. I wish you all the very best in the future.

Finally, I am deeply grateful to my family for their long-standing trust, love, and unwavering support, which made this work possible.

Entong Liu, Gothenburg, December 2025

List of Acronyms

Below is the list of acronyms that have been used throughout this thesis listed in alphabetical order:

EM	Electromagnetic
PM	Permanent Magnet
PMSM	Permanent Magnet Synchronous Motor
IPM	Interior Permanent Magnet Synchronous Motor
SPM	Surface Permanent Magnet Synchronous Motor
MMF	Magnetomotive Force
ISDW	Integer Slot Distributed Winding
FSCW	Fractional Slot Concentrated Winding
ERP	Equivalent Radiated Power
2D FFT	2-Dimensional Fast Fourier Transform

Contents

1

Introduction

1.1 Background

With the rapid development of electrified transportation and high-performance industrial drives, vibration and noise have become critical performance metrics of electrical machines in addition to efficiency and power density. In modern permanent magnet synchronous machines (PMSMs), electromagnetic vibration is widely recognized as the dominant source of audible noise, particularly under low and medium speed operating conditions [1]. The electromagnetic forces generated in the air gap interact with the stator structure may excite structural resonances, leading to excessive vibration and noise radiation.

Extensive studies have shown that the amplitude, spatial order, and frequency of electromagnetic force harmonics play decisive roles in determining the vibro-acoustic behavior of electrical machines [2]. Low spatial-order force components are especially critical due to their strong coupling with stator structural modes [3]. Consequently, understanding the generation mechanisms of electromagnetic forces and their transmission paths to structural vibration is essential for low-noise machine design.

Accurate prediction of electromagnetic forces relies on precise modeling of the air-gap magnetic field. Although finite-element methods (FEM) provide high accuracy, analytical models remain attractive due to their physical insight and computational efficiency. Classical analytical solutions of air-gap magnetic field in PMSMs were systematically established by Zhu and Howe through a series of works, covering open-circuit, armature reaction, slotting effects, and on-load conditions [4, 5, 6, 7].

To incorporate stator slotting effects, the concept of relative air-gap permeance has been widely adopted. A landmark contribution was made by Zarko *et al.*, who introduced the complex relative air-gap permeance derived from conformal mapping, enabling accurate analytical calculation of both radial and tangential flux density components in slotted air gaps [8]. This approach significantly improved the fidelity of analytical electromagnetic force prediction and has since been widely referenced in electromagnetic vibration studies.

Furthermore, winding configuration and pole–slot combinations have been shown to strongly influence the spatial harmonic content of air-gap magnetic fields. Fractional-slot concentrated-winding (FSCW) machines, in particular, exhibit richer harmonic spectra compared with distributed-winding machines, which may exacerbate elec-

tromagnetic force harmonics and vibration issues [9].

Beyond electromagnetic field modulation caused by slotting, the mechanical transmission of air-gap forces to the stator yoke introduces an additional modulation mechanism associated with stator teeth. Early analytical vibration models commonly simplified the slotted stator as an equivalent smooth cylinder and assumed that only low spatial-order air-gap forces contribute significantly to vibration. However, recent studies have revealed that such simplifications may be invalid for machines with strong slotting effects.

Fang *et al.* demonstrated that high-order air-gap force harmonics can be transformed into low-order vibration modes through a modulation effect induced by the slotted stator structure [10]. This phenomenon was further extended to PMSMs, where stator tooth modulation was shown to significantly reshape the force spectrum acting on the stator yoke [11]. Analytical formulations have since been developed to describe this mechanical modulation process and to clarify the conditions under which it becomes prominent.

In addition, tangential electromagnetic forces and their coupling with radial forces have been identified as non-negligible excitation sources in machines with high pole numbers or FSCW configurations. Hybrid analytical–numerical models incorporating both tooth modulation and tangential effects have been proposed to improve vibration prediction accuracy [12].

The vibration and noise performance of electrical machines is ultimately governed by the interaction between electromagnetic excitation forces and the structural dynamics of the stator–housing assembly. Modal analysis provides essential information on the natural frequencies and mode shapes that can be excited by electromagnetic forces.

It has long been established that each structural mode is predominantly excited by force components with matching spatial orders [2]. Among these modes, the breathing mode (mode 0) has attracted particular attention in traction PMSMs due to its strong acoustic radiation efficiency and its frequent occurrence within the audible frequency range [3]. Recent experimental investigations on electric vehicles have confirmed that 0th mode vibration can dominate the overall acoustic behavior of traction machines.

To capture the complex coupling between electromagnetic forces and structural vibration, multiphysics approaches combining electromagnetic analysis, modal analysis, and harmonic response simulation have been widely adopted. Recent review studies have emphasized that a clear physical understanding of electromagnetic force generation, modulation, and transmission is a prerequisite for effective vibration suppression in PMSMs [1]. Nevertheless, a systematic and unified treatment of electromagnetic force generation, stator tooth modulation, and vibration response across different machine types and pole–slot combinations remains an open research topic.

1.2 Purpose

Despite substantial progress in the study of electromagnetic vibration and noise in permanent magnet synchronous machines (PMSMs), most existing works focus either on the generation of air-gap electromagnetic forces or on the structural vibration response of the stator. However, the force transmission process from the air gap to the stator teeth, together with the associated mechanical modulation mechanisms, has not yet been systematically investigated and compared across different machine topologies. In particular, for machines with significantly different pole–slot combinations and winding configurations, the characteristics of tooth electromagnetic forces and their role in vibration excitation remain insufficiently understood.

Motivated by this research gap, the primary objective of this study is to systematically characterize the formation mechanisms and spectral features of electromagnetic forces acting on stator teeth in PMSMs, and to clarify how these characteristics are influenced by pole–slot combinations and machine structures. To this end, analytical models of both radial and tangential air-gap electromagnetic forces are established, followed by an investigation of the mechanical modulation effect introduced by stator teeth during force transmission. Special attention is paid to how this modulation process reshapes the spatial and temporal harmonic contents of tooth forces and alters their potential to excite structural vibrations.

Within this framework, a comparative study is conducted between a representative integral-slot distributed-winding interior PMSM and two fractional-slot concentrated-winding surface-mounted PMSMs. By adopting a unified theoretical formulation and consistent evaluation criteria, the electromagnetic field distributions, electromagnetic force characteristics, and tooth force spectra of different machine types are systematically compared. The purpose of this comparison is to reveal both the common mechanisms and the fundamental differences in tooth force behavior induced by different pole–slot combinations, thereby providing a clear physical basis for the low-vibration and low-noise design of PMSMs.

2

Analytical model of air-gap forces

The electromagnetic (EM) force waves in a Permanent Magnet Synchronous Motor (PMSM) are the direct sources of motor vibration and torque. Therefore, it is important to carry out analytical modeling and theoretical analysis of these force waves. In this chapter, an analytical model for electromagnetic force waves is first established based on the electromagnetic field of a unit machine. The model can be then extended and applied to different motor topologies. By introducing the concept of complex relative air-gap permeance, it considers both radial and tangential electromagnetic forces acting in the air gap when slotting is present. At the end of the chapter, the time and spatial harmonics of the electromagnetic force waves for different motors under ideal sinusoidal currents are presented.

2.1 Analytical model of air-gap flux density in slotless unit machine

2.1.1 Flux distribution due to PM

Based on the source of excitation, the air-gap magnetic field can be decomposed into two components: the magnetic field generated by the rotor permanent magnets B_{PM} and the magnetic field produced by the stator winding currents B_{arm}. The structure of a slotless surface-mounted PMSM is shown in Fig. 2.1. The magnetic field distribution of the permanent magnet is symmetrically distributed along the geometric centerline of the magnet and can be expressed as

$$B_{r,PM}(\theta) = B_{r,PM}(-\theta) \tag{2.1}$$

$$B_{t,PM}(\theta) = -B_{t,PM}(-\theta) \tag{2.2}$$

where subscript r indicates radial components and subscript t indicates tangential components, θ is the mechanical angle along the air-gap and $\theta = 0$ at the geometric centerline of the magnet. Therefore, according to the properties of the Fourier series, the expansion of the radial magnetic flux density will contain only cosine terms, while the tangential magnetic flux density will contain only sine terms.

Meanwhile, due to the alternating arrangement of magnetic poles, the air-gap magnetic field also satisfies

$$B_{r,PM}(\theta) = -B_{r,PM}(\theta + \frac{T_s}{2}) \tag{2.3}$$

$$B_{t,PM}(\theta) = -B_{t,PM}(\theta + \frac{T_s}{2}) \tag{2.4}$$

where T_s is the spatial period of magnetic field, $T_s = \pi/p$, and p is the number of pole pairs.

From (2.3) and (2.4), it can be concluded that only the odd-order terms are contained in the Fourier series of the radial and tangential magnetic flux densities. Combining above discussions, the no-load air-gap magnetic field in the slotless model can be expressed as

$$B_{r,PM}(\theta, t) = \sum_{u=1,3,5}^{\infty} B_{r,u}^{\mathrm{PM}} cos(up\theta - up\omega t) \tag{2.5}$$

$$B_{t,PM}(\theta, t) = \sum_{u=1,3,5}^{\infty} B_{t,u}^{\mathrm{PM}} sin(up\theta - up\omega t) \tag{2.6}$$

where $B_{r,u}^{\mathrm{PM}}$ represents the magnitude of the uth radial flux density, $B_{t,u}^{\mathrm{PM}}$ represents the magnitude of the uth tangential flux density, ω is the mechanical frequency, θ is the mechanical angle along the air gap. The counterclockwise direction is defined as the positive direction of the motor rotation. Minus sign indicates the magnetic field rotating in the positive direction.

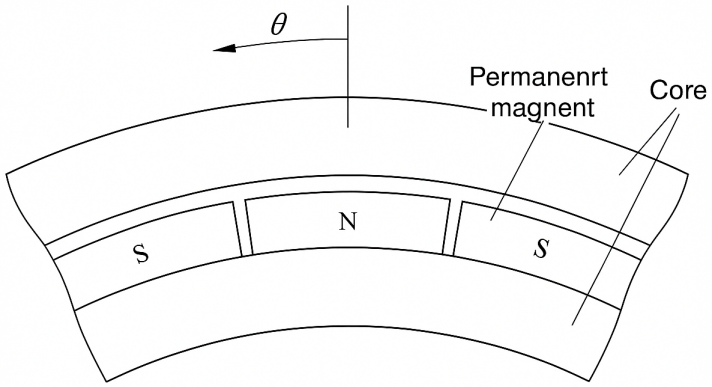

Figure 2.1: The slotless stucture of PMSM

2.1.2 Flux distribution due to Armature reaction

Different pole-slot combinations lead to various stator winding configurations, which consequently effect the components existing in the armature reaction field. To establish a unified analytical model that can accommodate various machine topologies, the concept of the unit machine is introduced as a fundamental modeling unit. The pole–slot relationship between the unit machine and the original machine can be expressed as follows

$$\frac{N_s}{p} = \frac{N_0 N_{s0}}{N_0 p_0} \tag{2.7}$$

where p_0 and N_{s0} are the pole pair and slot numbers of the unit machine, which are mutually prime, and N_0 represents the number of unit machines contained in the original machine. In the machines investigated in this work, the 10-pole 12-slot motor(10p12s) itself can be regarded as the unit machine. For the 8-pole 12-slot motor(8p12s), its unit machine corresponds to a 2-pole, 3-slot unit. For the 8-pole 48-slot motor(8p48s), the unit machine is defined as a 2-pole, 12-slot unit.

In the unit machine, the three-phase windings are spatially distributed in a periodic way. The radial air-gap magnetic fields produced by the three phases are spatially displaced by $2\pi/3$ mechanical radians and can be expressed respectively as

$$\begin{aligned} B_{r0}^{A}(\theta,t) &= \sum_{v0} G_{v0} i_A(t) \cos v_0(\theta), \\ B_{r0}^{B}(\theta,t) &= \sum_{v0} G_{v0} i_B(t) \cos v_0(\theta - \frac{2\pi}{3}), \\ B_{r0}^{C}(\theta,t) &= \sum_{v0} G_{v0} i_C(t) \cos v_0(\theta + \frac{2\pi}{3}), \end{aligned} \tag{2.8}$$

where B_{r0}^{A}, B_{r0}^{B}, B_{r0}^{C} are the radial air-gap flux densities produced by the three phase armature windings of the unit machine, respectively. The term v_0 represents the spatial harmonic order of the air-gap flux density. G_{v0} is the winding factor of the $v0$th spatial harmonic of single phase winding.

In a symmetrical three-phase winding, considering only the fundamental component of the phase currents, they can be expressed as

$$\begin{aligned} i_A(t) &= I_1 \cos(p_0\omega t + \phi_1), \\ i_B(t) &= I_1 \cos\Big(p_0\omega t - \frac{2\pi}{3} + \phi_1\Big), \\ i_C(t) &= I_1 \cos\Big(p_0\omega t + \frac{2\pi}{3} + \phi_1\Big), \end{aligned} \tag{2.9}$$

where I_1 denotes the amplitude of the fundamental current, and ω is the mechanical frequency of the unit machine and ϕ_1 is the phasor of fundamental current.

Substituting (2.9) into (2.8), the radial air-gap flux density produced by each phase armature winding of the unit machine can be derived. By linear superposition, the resultant radial air-gap flux density of the three-phase winding in the unit machine can be expressed as

$$\begin{aligned} B_{r_0}^{\mathrm{ARM}}(\theta,t) &= B_{r_0}^{A}(\theta,t) + B_{r_0}^{B}(\theta,t) + B_{r_0}^{C}(\theta,t) \\ &= \sum_{v_0} G_{v_0} I_1 \Bigg\{ \cos(p_0\omega t + \phi_1)\cos(v_0\theta) \\ &\quad + \cos(p_0\omega t - \tfrac{2\pi}{3} + \phi_1)\cos\Big[v_0\Big(\theta - \tfrac{2\pi}{3}\Big)\Big] \\ &\quad + \cos(p_0\omega t + \tfrac{2\pi}{3} + \phi_1)\cos\Big[v_0\Big(\theta + \tfrac{2\pi}{3}\Big)\Big]\Bigg\}. \end{aligned} \tag{2.10}$$

Equation (2.10) can be further simplified as

$$B_{r_0}^{\mathrm{ARM}}(\theta,t)=\sum_{v_0}G_{v_0}I_1\frac{1}{2}\Big[\Big(1+2\cos\tfrac{2\pi}{3}(v_0-1)\Big)\cos\Big(p_0\omega t-v_0\theta+\phi_1\Big) + \Big(1+2\cos\tfrac{2\pi}{3}(v_0+1)\Big)\cos\Big(p_0\omega t+v_0\theta+\phi_1\Big)\Big]. \tag{2.11}$$

It can be noticed from (2.11) that the armature-reaction radial air-gap flux density harmonics exist only when the spatial harmonic order v_0 satisfies certain specific conditions as

$$B_{r_0}^{\mathrm{ARM}}(\theta,t)=\begin{cases}\sum_{v_0}G_{v_0}\dfrac{3I_1}{2}\cos\Big(p_0\omega t-v_0\theta+\phi_1\Big), & v_0=3k+1,k\geq 0\\ \sum_{v_0}G_{v_0}\dfrac{3I_1}{2}\cos\Big(p_0\omega t+v_0\theta+\phi_1\Big), & v_0=3k-1,k\geq 0.\end{cases} \tag{2.12}$$

In (2.12), when $v_0=3k+1$, the corresponding radial air-gap flux density harmonic rotates in counterclockwise direction(positive sequence), when $v_0=3k-1$, it rotates in the opposite direction(negative sequence).

In particular, when the slot number of the unit machine N_{s0} is even, the positive and negative coil sides of each phase armature winding are spatially separated by π mechanical radians. Since the current directions in the positive and negative coil sides are opposite, the air-gap flux density produced by each phase winding satisfies the half-wave symmetry condition $B_{r0}^{\mathrm{ARM}}(\theta)=-B_{r0}^{\mathrm{ARM}}(\theta+T_{s0}/2)$. The winding configuration and single phase flux density distribution are shown in Fig. 2.2. According to the properties of Fourier series, the spatial air-gap flux density under this condition contains only odd-order harmonics,

$$B_{r_0}^{\mathrm{ARM}}(\theta,t)=\begin{cases}\sum_{v_0}G_{v_0}\dfrac{3I_1}{2}\cos\Big(p_0\omega t-v_0\theta+\phi_1\Big), & v_0=6k+1,k\geq 0\\ \sum_{v_0}G_{v_0}\dfrac{3I_1}{2}\cos\Big(p_0\omega t+v_0\theta+\phi_1\Big), & v_0=6k-1,k\geq 0.\end{cases} \tag{2.13}$$

In (2.13), when $v_0=6k+1$, the corresponding radial air-gap flux density harmonic rotates in counterclockwise direction(positive sequence), when $v_0=6k-1$, it rotates in the opposite direction(negative sequence).

Considering the uniformity and conciseness of the expression for the armature-reaction radial air-gap magnetic field, (2.12) and (2.13) can be further simplfied as

$$B_{r_0}^{\mathrm{ARM}}(\theta,t)=\sum_{v_0}G_{v_0}\frac{3I_1}{2}\cos\Big(p_0\omega t-v_0\theta+\phi_1\Big),\quad \begin{cases}v_0=3k+1, & k\in\mathbb{Z}, \quad N_{s0}\text{ is odd},\\ v_0=6k+1, & k\in\mathbb{Z}, \quad N_{s0}\text{ is even}.\end{cases} \tag{2.14}$$

where v_0 is a positive integer. A negative sign in front of v_0 indicates a positive-sequence rotating field, while a positive sign indicates a negative-sequence rotating field.

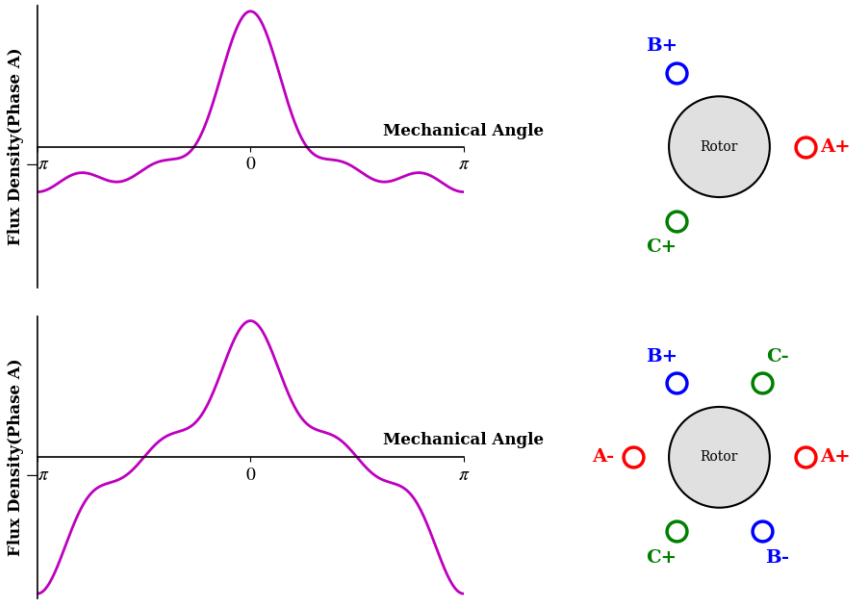

Figure 2.2: The typical winding configuration and air-gap flux density distribution of single phase when $N_{s0} = 3$ and $N_{s0} = 6$. When N_{s0} is even, the winding configuration ensures that the flux density distribution is half-wave symmetric. When N_{s0} is odd, it is impossible to guarantee this property.

As the original machine is composed of N_0 unit machines arranged circumferentially, the general expression of its armature-reaction radial air-gap magnetic field is given by

$$\begin{aligned} B_r^{\mathrm{ARM}}(\theta,t) &= \sum_{v_0} G_{v_0} \frac{3I_1}{2} \cos\Big(N_0 p_0 \omega t - N_0 v_0 \theta + \phi_1\Big), \\ &= \sum_{v} B_{r,v}^{\mathrm{ARM}} \cos\Big(p\omega t - v\theta + \phi_1\Big), \\ &\begin{cases} v = (3k+1)N_0, & k \in \mathbb{Z}, \quad N_{s0} \text{ is odd}, \\ v = (6k+1)N_0, & k \in \mathbb{Z}, \quad N_{s0} \text{ is even}. \end{cases} \end{aligned} \tag{2.15}$$

where $B_{r,v}^{\mathrm{ARM}}$ denotes the amplitude of the vth radial air-gap flux density harmonic, v represent the spatial harmonic order in terms of original machine.

Since the tangential air-gap field satisfies the same time–space periodicity as the radial one, it has identical harmonic orders but different amplitudes and phases. Hence, the tangential field can be written as

$$\begin{aligned} B_t^{\mathrm{ARM}}(\theta,t) &= \sum_{v} B_{t,v}^{\mathrm{ARM}} \sin\Big(p\omega t - v\theta + \phi_1\Big), \\ &\begin{cases} v = (3k+1)N_0, & k \in \mathbb{Z}, \quad N_{s0} \text{ is odd}, \\ v = (6k+1)N_0, & k \in \mathbb{Z}, \quad N_{s0} \text{ is even}. \end{cases} \end{aligned} \tag{2.16}$$

where $B_{t,v}^{\mathrm{ARM}}$ denotes the amplitude of the vth tangential air-gap flux density harmonic.

From (2.16), the time and spatial order of the harmonics contained in the armature reaction air-gap flux densities presented in different machines can be derived in Table 2.1 as

Table 2.1: Time and spatial order of flux densities for various types of machines in slotless model

Type of machine	Time order	Spatial Order	
10p12s	p	$v = v_0$	$v_0 = 6k - 1, k \in \mathbb{Z}$
8p48s	p	$v = pv_0$	$v_0 = 6k + 1, k \in \mathbb{Z}$
8p12s	p	$v = pv_0$	$v_0 = 3k + 1, k \in \mathbb{Z}$

Due to the configuration of the three-phase windings, the phase sequence of the 10p12s machine is opposite to that of the other two machines, and therefore the value of v_0 differs. From Table 2.1, it can be noticed that the minimum spatial order of the air-gap flux density for the 10p12s machine is 1, rather than its pole pair number $p = 5$ (which also corresponds to the harmonic that produces the constant torque). This implies that electromagnetic forces with lower spatial orders may exist in this kind of machine. Furthermore, for the 8p12s machine, since the slot number of its unit machine $N_{s0} = 3$ is odd, there are even spatial harmonics existing in the air-gap flux density, it will present a more abundant harmonic content in the air-gap flux density distribution.

2.2 Analytical model of air-gap flux density in slotted unit machine

Next, the influence introduced by the slot openings will be investigated. The effects of slot openings on the air-gap flux density are illustrated in Fig. 2.3. Reference [8] points out that by assuming the slot shape to be ideally parallel and further applying mathematical methods such as conformal transformation, a complex relative permeance function can be introduced on the basis of the slotless model to account for the slotting effect. The air-gap magnetic field component considering the slotting effect can thus be expressed as

$$B_{sr}(\theta, t) = B_r(\theta, t)\lambda_a(\theta) + B_t(\theta, t)\lambda_b(\theta) \tag{2.17}$$

$$B_{st}(\theta, t) = B_t(\theta, t)\lambda_a(\theta) - B_r(\theta, t)\lambda_b(\theta) \tag{2.18}$$

where $B_r(\theta, t)$ and $B_t(\theta, t)$ represent the radial and tangential air-gap flux densities of the slotless model, respectively. $B_{sr}(\theta, t)$ and $B_{st}(\theta, t)$ represent the radial and tangential air-gap flux densities of the slotted model, respectively. $\lambda_a(\theta)$ and $\lambda_b(\theta)$

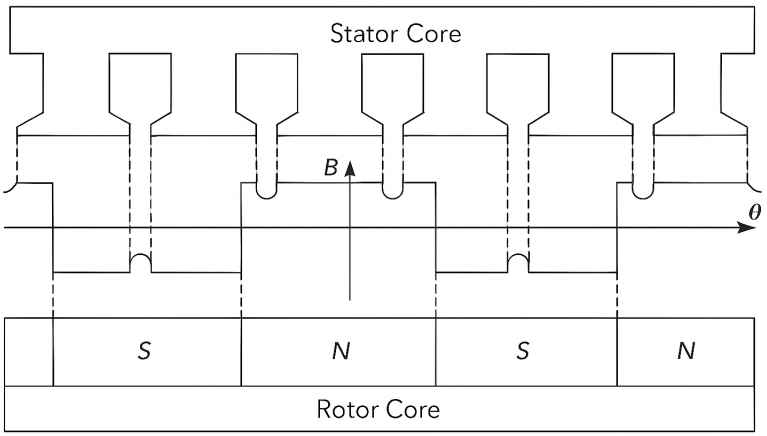

Figure 2.3: The slotted stucture of PMSM

are the real and imaginary parts of the complex relative permeance of the air gap, and can be expressed as

$$\lambda_a = \lambda_0 + \sum_i \lambda_{ai} \cos(iN_s\theta) \tag{2.19}$$

$$\lambda_b = \sum_i \lambda_{bi} \sin(iN_s\theta) \tag{2.20}$$

where λ_{ai} and λ_{bi} represent the amplitudes of the real and imaginary parts of the complex relative air-gap permeance harmonics. i denotes the spatial order of the complex relative air-gap permeance harmonics, and N_s is the number of stator slots of the machine.

2.2.1 Flux distribution due to PM

Substituting (2.5)-(2.6) and (2.19)-(2.20) into (2.17)-(2.18), the radial and tangential no load air-gap flux densities considering slot opening effect can be derived as

$$\begin{aligned}
B_{sr}^{\mathrm{PM}}(\theta,t) &= \sum_{u=1,3,5}^{\infty}\sum_{i=0}^{\infty}\frac{1}{2}B_{r,u}^{\mathrm{PM}}\lambda_{ai}\left[\cos\Big((up+iN_s)\theta-up\omega t\Big)+\cos\Big((up-iN_s)\theta-up\omega t\Big)\right] \\
&+ \sum_{u=1,3,5}^{\infty}\sum_{i=0}^{\infty}\frac{1}{2}B_{t,u}^{\mathrm{PM}}\lambda_{bi}\left[\cos\Big((up+iN_s)\theta-up\omega t\Big)-\cos\Big((up-iN_s)\theta-up\omega t\Big)\right] \\
&= \sum_{u=1,3,5}^{\infty}\sum_{i=0}^{\infty}\left(\frac{1}{2}B_{r,u}^{\mathrm{PM}}\lambda_{ai}+\frac{1}{2}B_{t,u}^{\mathrm{PM}}\lambda_{bi}\right)\cos\Big((up+iN_s)\theta-up\omega t\Big) \\
&+ \sum_{u=1,3,5}^{\infty}\sum_{i=0}^{\infty}\left(\frac{1}{2}B_{r,u}^{\mathrm{PM}}\lambda_{ai}-\frac{1}{2}B_{t,u}^{\mathrm{PM}}\lambda_{bi}\right)\cos\Big((up-iN_s)\theta-up\omega t\Big)
\end{aligned} \tag{2.21}$$

$$
\begin{aligned}
B_{st}^{\mathrm{PM}}(\theta,t) &= \sum_{u=1,3,5}^{\infty}\sum_{i=0}^{\infty}\frac{1}{2}B_{t,u}^{\mathrm{PM}}\lambda_{ai}\left[\sin\Big((up+iN_s)\theta-up\omega t\Big)+\sin\Big((up-iN_s)\theta-up\omega t\Big)\right],\\
&- \sum_{u=1,3,5}^{\infty}\sum_{i=0}^{\infty}\frac{1}{2}B_{r,u}^{\mathrm{PM}}\lambda_{bi}\left[\sin\Big((up+iN_s)\theta-up\omega t\Big)-\sin\Big((up-iN_s)\theta-up\omega t\Big)\right]\\
&= \sum_{u=1,3,5}^{\infty}\sum_{i=0}^{\infty}\left(\frac{1}{2}B_{t,u}^{\mathrm{PM}}\lambda_{ai}-\frac{1}{2}B_{r,u}^{\mathrm{PM}}\lambda_{bi}\right)\sin\Big((up+iN_s)\theta-up\omega t\Big)\\
&+ \sum_{u=1,3,5}^{\infty}\sum_{i=0}^{\infty}\left(\frac{1}{2}B_{t,u}^{\mathrm{PM}}\lambda_{ai}+\frac{1}{2}B_{r,u}^{\mathrm{PM}}\lambda_{bi}\right)\sin\Big((up-iN_s)\theta-up\omega t\Big)
\end{aligned}
\tag{2.22}
$$

Since the primary focus of this study is on the spatial and time components of the air-gap magnetic flux density harmonics rather than their magnitudes, considering the conciseness of the expression, (2.21) and (2.22) can be further simplified as

$$
B_{sr}^{\mathrm{PM}}(\theta,t)=\sum_{u=1,3,5}^{\infty}\sum_{i=-\infty}^{\infty}B_{r,ui}^{\mathrm{PM}}\cos\Big((up+iN_s)\theta-up\omega t\Big) \tag{2.23}
$$

$$
B_{st}^{\mathrm{PM}}(\theta,t)=\sum_{u=1,3,5}^{\infty}\sum_{i=-\infty}^{\infty}B_{t,ui}^{\mathrm{PM}}\sin\Big((up+iN_s)\theta-up\omega t\Big) \tag{2.24}
$$

where $B_{r,ui}^{\mathrm{PM}}$ and $B_{t,ui}^{\mathrm{PM}}$ are the amplitudes of the corresponding spatial–temporal harmonics of the radial and tangential air-gap flux densities, respectively.

2.2.2 Flux distribution due to Armature reaction

Substituting (2.15)-(2.16) and (2.19)-(2.20) into (2.17)-(2.18), the radial and tangential air-gap flux densities by armature reaction considering slot opening effect can be derived as

$$
\begin{aligned}
B_{sr}^{\mathrm{ARM}}(\theta,t) &= \sum_{v}\sum_{i=0}^{\infty}\frac{1}{2}B_{r,v}^{\mathrm{ARM}}\lambda_{ai}\left[\cos\Big(p\omega t-(v-iN_s)\theta+\phi_1\Big)+\cos\Big(p\omega t-(v+iN_s)\theta+\phi_1\Big)\right]\\
&+ \sum_{v}\sum_{i=0}^{\infty}\frac{1}{2}B_{t,v}^{\mathrm{ARM}}\lambda_{bi}\left[\cos\Big(p\omega t-(v-iN_s)\theta+\phi_1\Big)-\cos\Big(p\omega t-(v+iN_s)\theta+\phi_1\Big)\right]\\
&= \sum_{v}\sum_{i=0}^{\infty}\left(\frac{1}{2}B_{r,v}^{\mathrm{ARM}}\lambda_{ai}+\frac{1}{2}B_{t,v}^{\mathrm{ARM}}\lambda_{bi}\right)\cos\Big(p\omega t-(v-iN_s)\theta+\phi_1\Big)\\
&+ \sum_{v}\sum_{i=0}^{\infty}\left(\frac{1}{2}B_{r,v}^{\mathrm{ARM}}\lambda_{ai}+\frac{1}{2}B_{t,v}^{\mathrm{ARM}}\lambda_{bi}\right)\cos\Big(p\omega t-(v+iN_s)\theta+\phi_1\Big)
\end{aligned}
\tag{2.25}
$$

$$
\begin{aligned}
B_{st}^{\mathrm{ARM}}(\theta,t) &= \sum_{v}\sum_{i=0}^{\infty}\frac{1}{2}B_{t,v}^{\mathrm{ARM}}\lambda_{ai}\left[\sin\Big(p\omega t-(v-iN_s)\theta+\phi_1\Big)+\sin\Big(p\omega t-(v+iN_s)\theta+\phi_1\Big)\right]\\
&-\sum_{v}\sum_{i=0}^{\infty}\frac{1}{2}B_{r,v}^{\mathrm{ARM}}\lambda_{bi}\left[\sin\Big(p\omega t-(v-iN_s)\theta+\phi_1\Big)-\sin\Big(p\omega t-(v+iN_s)\theta+\phi_1\Big)\right]\\
&=\sum_{v}\sum_{i=0}^{\infty}\left(\frac{1}{2}B_{t,v}^{\mathrm{ARM}}\lambda_{ai}-\frac{1}{2}B_{r,v}^{\mathrm{ARM}}\lambda_{bi}\right)\sin\Big(p\omega t-(v-iN_s)\theta+\phi_1\Big)\\
&+\sum_{v}\sum_{i=0}^{\infty}\left(\frac{1}{2}B_{t,v}^{\mathrm{ARM}}\lambda_{ai}+\frac{1}{2}B_{r,v}^{\mathrm{ARM}}\lambda_{bi}\right)\sin\Big(p\omega t-(v+iN_s)\theta+\phi_1\Big)
\end{aligned}
\tag{2.26}
$$

considering the conciseness of the expression, (2.25) and (2.26) can be further simplified as

$$
B_{sr}^{\mathrm{ARM}}(\theta,t)=\sum_{v}\sum_{i=-\infty}^{\infty}B_{r,vi}^{\mathrm{ARM}}\cos\Big(p\omega t-(v+iN_s)\theta+\phi_1\Big) \tag{2.27}
$$

$$
B_{st}^{\mathrm{ARM}}(\theta,t)=\sum_{v}\sum_{i=-\infty}^{\infty}B_{t,vi}^{\mathrm{ARM}}\sin\Big(p\omega t-(v+iN_s)\theta+\phi_1\Big) \tag{2.28}
$$

where $B_{r,vi}^{\mathrm{ARM}}$ and $B_{t,vi}^{\mathrm{ARM}}$ are the amplitudes of the corresponding spatial–temporal harmonics of the radial and tangential armature reaction air-gap flux densities, respectively. The coefficient preceding θ indicates the rotation direction of the magnetic field. A positive coefficient corresponds to forward rotation of the machine, while a negative coefficient corresponds to reverse rotation. The value of v depends on N_{s0} as presented in (2.15) and (2.16).

2.2.3 Total flux distribution in different machines

Under the assumption of qualitative analysis, the effect of core saturation can be neglected, and the resultant air-gap magnetic field can be regarded as the linear superposition of PM and armature reaction fields as

$$
\begin{aligned}
B_{sr}(\theta,t) &= \sum_{u=1,3,5}\sum_{i=-\infty}^{\infty}B_{r,ui}^{\mathrm{PM}}\cos\Big((up+iN_s)\theta-up\omega t\Big)\\
&+\sum_{v}\sum_{i=-\infty}^{\infty}B_{r,vi}^{\mathrm{ARM}}\cos\Big(p\omega t-(v+iN_s)\theta+\phi_1\Big)
\end{aligned}
\tag{2.29}
$$

$$
\begin{aligned}
B_{st}(\theta,t) &= \sum_{u=1,3,5}\sum_{i=-\infty}^{\infty}B_{t,ui}^{\mathrm{PM}}\sin\Big((up+iN_s)\theta-up\omega t\Big)\\
&+\sum_{v}\sum_{i=-\infty}^{\infty}B_{t,vi}^{\mathrm{ARM}}\sin\Big(p\omega t-(v+iN_s)\theta+\phi_1\Big)
\end{aligned}
\tag{2.30}
$$

According to (2.29) and (2.30), the temporal and spatial orders of the air-gap flux density for different motors can be derived and arranged as shown in Table 2.2.

Table 2.2: Time and spatial order of flux densities for various types of machines in slotted model

Type of machine	Source	Time order	Spatial Order		
10p12s	PM	up	$iN_s + up$	$u = 2k_1 + 1$	
	ARM	p	$iN_s + v_0$	$v_0 = 6k_2 - 1$	
8p48s	PM	up	$iN_s + up$	$u = 2k_1 + 1$	$k_1 \in \mathbb{Z}_{\geq 0}$
	ARM	p	$iN_s + pv_0$	$v_0 = 6k_2 + 1$	$k_2, i \in \mathbb{Z}$
8p12s	PM	up	$iN_s + up$	$u = 2k_1 + 1$	
	ARM	p	$iN_s + pv_0$	$v_0 = 3k_2 + 1$	

From Table 2.2, it can be seen that slots opening has no modulation effect on the temporal components of the air-gap magnetic field. The temporal orders of the armature reaction field contain only harmonics of the pole-pair number, whereas the temporal components of the permanent excited field are multiples of pole-pair number.

Slots opening imposes a modulation effect on both the armature reaction field and the permanent excited field. It can be proved that the spatial orders of any machine are multiples of the greatest common divisor of the number of slots and the pole-pair number $k\,\mathrm{GCD}(p, N_s)$. Therefore, for the 8p48s and 8p12s machines, the minimum spatial order of the air-gap flux is equal to the pole-pair number p. In contrast, for the 10p12s machine, the minimum spatial order of the air-gap flux is 1 rather than the pole-pair number $p = 5$. Hence, for some fractional-slot concentrated-winding machines, the air-gap magnetic field contains spatial harmonics with orders lower than the fundamental component (which corresponds to the pole-pair number).

2.3 Analytical model of air-gap force density

After deriving the expression of the air-gap flux density, the radial and tangential electromagnetic force waves in the air gap can be calculated using the Maxwell stress tensor method. The relationship between the electromagnetic force waves and the air-gap flux density can be expressed as

$$p_{sr}(\theta, t) = \frac{1}{2\mu_0}\Big(B_{sr}(\theta, t)^2 - B_{st}(\theta, t)^2\Big) \tag{2.31}$$

$$p_{st}(\theta, t) = \frac{1}{\mu_0} B_{sr}(\theta, t) B_{st}(\theta, t) \tag{2.32}$$

where p_{sr} and p_{st} are the radial and tangential force densities of air-gap electromagnetic forces, respectively. Inserting (2.29) and (2.30) into (2.31) and (2.32), the

compositions of electromagnetic force waves can be expressed as

$$\begin{aligned} p_{sr}(\theta,t) &= \frac{1}{2\mu_0}\Big(B_{sr}^{\mathrm{PM}}(\theta,t)^2 - B_{st}^{\mathrm{PM}}(\theta,t)^2\Big) \\ &+ \frac{1}{2\mu_0}\Big(B_{sr}^{\mathrm{ARM}}(\theta,t)^2 - B_{st}^{\mathrm{ARM}}(\theta,t)^2\Big) \\ &+ \frac{1}{\mu_0}\Big(B_{sr}^{\mathrm{PM}}(\theta,t)B_{sr}^{\mathrm{ARM}}(\theta,t) - B_{st}^{\mathrm{PM}}(\theta,t)B_{st}^{\mathrm{ARM}}(\theta,t)\Big) \\ &= p_{sr}^{\mathrm{PM}\times\mathrm{PM}}(\theta,t) + p_{sr}^{\mathrm{ARM}\times\mathrm{ARM}}(\theta,t) + p_{sr}^{\mathrm{PM}\times\mathrm{ARM}}(\theta,t) \end{aligned} \tag{2.33}$$

$$\begin{aligned} p_{st}(\theta,t) &= \frac{1}{\mu_0}\Big(B_{sr}^{\mathrm{PM}}(\theta,t)B_{st}^{\mathrm{PM}}(\theta,t)\Big) \\ &+ \frac{1}{\mu_0}\Big(B_{sr}^{\mathrm{ARM}}(\theta,t)B_{st}^{\mathrm{ARM}}(\theta,t)\Big) \\ &+ \frac{1}{\mu_0}\Big(B_{sr}^{\mathrm{PM}}(\theta,t)B_{st}^{\mathrm{ARM}}(\theta,t) + B_{st}^{\mathrm{PM}}(\theta,t)B_{sr}^{\mathrm{ARM}}(\theta,t)\Big) \\ &= p_{st}^{\mathrm{PM}\times\mathrm{PM}}(\theta,t) + p_{st}^{\mathrm{ARM}\times\mathrm{ARM}}(\theta,t) + p_{st}^{\mathrm{PM}\times\mathrm{ARM}}(\theta,t) \end{aligned} \tag{2.34}$$

where the superscript PM × PM denotes the electromagnetic forces generated by the interaction between PM fields, the superscript ARM × ARM denotes the electromagnetic forces generated by the interaction between armature reaction fields and the superscript PM × ARM denotes the electromagnetic forces generated by the interaction between PM and armature reaction fields.

From the above equations, the electromagnetic forces in the air gap can be decomposed into three components. In the following, the explicit expressions of each component are derived, and their temporal and spatial characteristics are analyzed.

2.3.1 EM forces generated by PMs

The EM forces due to the interaction between PM fields can be expressed as

$$\begin{aligned} p_{sr}^{\mathrm{PM}\times\mathrm{PM}}(\theta,t) = \sum_{u_1}\sum_{u_2}\sum_{i_1}\sum_{i_2} p_{sr,u_1u_2i_1i_2}^{\mathrm{PM}\times\mathrm{PM}} \cos\Bigg\{\Big[(u_1 \overset{1}{\pm} u_2)p + (i_1 \overset{1}{\pm} i_2)N_s\Big]\theta - \\ (u_1 \overset{1}{\pm} u_2)p\omega t\Bigg\} \end{aligned} \tag{2.35}$$

$$\begin{aligned} p_{st}^{\mathrm{PM}\times\mathrm{PM}}(\theta,t) = \sum_{u_1}\sum_{u_2}\sum_{i_1}\sum_{i_2} p_{st,u_1u_2i_1i_2}^{\mathrm{PM}\times\mathrm{PM}} \sin\Bigg\{\Big[(u_1 \overset{1}{\pm} u_2)p + (i_1 \overset{1}{\pm} i_2)N_s\Big]\theta - \\ (u_1 \overset{1}{\pm} u_2)p\omega t\Bigg\} \end{aligned} \tag{2.36}$$

where $p_{sr,u_1u_2i_1i_2}^{\mathrm{PM}\times\mathrm{PM}}$ and $p_{st,u_1u_2i_1i_2}^{\mathrm{PM}\times\mathrm{PM}}$ are the amplitudes of the radial and tangential EM force densities generated by PMs, respectively.

From the above expressions, it can be seen that the radial and tangential EM forces in the air gap share the same temporal and spatial harmonic components, differing only in amplitude and phase. The spatial orders can be further written as

$$|2kp + iN_s|, \quad k, i \in \mathbb{Z} \tag{2.37}$$

where $|2kp|$ originates from the PM fields, and $|iN_s|$ originates from the slotting modulation effect. According to the properties of the greatest common divisor, the minimum non-zero spatial order of the air-gap electromagnetic force is $\mathrm{GCD}(2p, N_s)$. Moreover, any spatial order must be an integer multiple of this minimum value, i.e., $k\,\mathrm{GCD}(2p, N_s)$. The temporal orders can be further expressed as

$$|2kp|, \quad k \in \mathbb{Z} \tag{2.38}$$

The frequencies are $|2kp|$ times the mechanical frequency, which corresponds to even multiples of the electrical frequency. The temporal components originate solely from the rotation of the rotor permanent magnets, and the slotting effect does not modulate the temporal orders of the electromagnetic force waves.

2.3.2 EM forces generated by Armature Reactions

The EM forces due to the interaction between Armature Reaction fields can be expressed as

$$\begin{aligned} p_{sr}^{\mathrm{ARM\times ARM}}(\theta, t) = \sum_{v_1} \sum_{v_2} \sum_{i_1} \sum_{i_2} p_{sr,v_1 v_2 i_1 i_2}^{\mathrm{ARM\times ARM}} \cos \Bigg\{ (p \overset{1}{\pm} p)\omega t - \\ \Big[(i_1 \overset{1}{\pm} i_2) N_s + (v_1 \overset{1}{\pm} v_2) \Big] \theta \Bigg\} \end{aligned} \tag{2.39}$$

$$\begin{aligned} p_{st}^{\mathrm{ARM\times ARM}}(\theta, t) = \sum_{v_1} \sum_{v_2} \sum_{i_1} \sum_{i_2} p_{st,v_1 v_2 i_1 i_2}^{\mathrm{ARM\times ARM}} \sin \Bigg\{ (p \overset{1}{\pm} p)\omega t - \\ \Big[(i_1 \overset{1}{\pm} i_2) N_s + (v_1 \overset{1}{\pm} v_2) \Big] \theta \Bigg\} \end{aligned} \tag{2.40}$$

where $p_{sr,v_1 v_2 i_1 i_2}^{\mathrm{ARM\times ARM}}$ and $p_{st,v_1 v_2 i_1 i_2}^{\mathrm{PM\times PM}}$ are the amplitudes of the radial and tangential EM force densities generated by Armature Reactions, respectively.

From the above expressions, it can be seen that the radial and tangential EM forces in the air gap share the same temporal and spatial harmonic components, differing only in amplitude and phase. Substituting the conditions in (2.15) and (2.16) into

above equations, the spatial orders can be further written as

$$
\begin{aligned}
&|(v_{0,1} \overset{1}{\pm} v_{0,2})N_0 + (i_1 \overset{1}{\pm} i_2)N_s| \\
=&\begin{cases}
\left|\Big[3(k_1 \overset{1}{\pm} k_2) + (1 \overset{1}{\pm} 1)\Big]N_0 + (i_1 \overset{1}{\pm} i_2)N_s\right|, & N_{s0} \text{ is odd}, \\
\left|\Big[6(k_1 \overset{1}{\pm} k_2) + (1 \overset{1}{\pm} 1)\Big]N_0 + (i_1 \overset{1}{\pm} i_2)N_s\right|, & N_{s0} \text{ is even}.
\end{cases} \\
=&\begin{cases}
\begin{cases}
\Big|\Big(3k+2\Big)N_0 + iN_s\Big|, & k,i \in \mathbb{Z}, \quad N_{s0} \text{ is odd}, \\
\Big|3kN_0 + iN_s\Big|
\end{cases} \\
\begin{cases}
\Big|\Big(6k+2\Big)N_0 + iN_s\Big|, & k,i \in \mathbb{Z}, \quad N_{s0} \text{ is even}, \\
\Big|6kN_0 + iN_s\Big|
\end{cases}
\end{cases}
\end{aligned}
\tag{2.41}
$$

where the terms with N_0 originates from the Armature Reaction fields, and it can be either 1 or p depending on the number of unit machines. $|iN_s|$ originates from the slotting modulation effect. It can be proved that the minimum non-zero spatial order of the air-gap electromagnetic force is $\mathrm{GCD}(2p, N_s)$. Moreover, any spatial order must be an integer multiple of this minimum value, i.e., $k\,\mathrm{GCD}(2p, N_s)$.

The temporal orders are either 0 or $2p$, which are also even multiples of the electrical frequency. The slotting effect does not modulate the temporal orders of the electromagnetic force waves.

2.3.3 EM forces generated by interaction between PM and Armature Reaction

The EM forces due to the interaction between the interaction between PM and Armature Reaction fields can be expressed as

$$
\begin{aligned}
p_{sr}^{\mathrm{PM\times ARM}}(\theta,t) = \sum_u \sum_v \sum_{i_1} \sum_{i_2} p_{sr,uvi_1i_2}^{\mathrm{PM\times ARM}} \cos\Bigg\{\Big[(i_1 \overset{1}{\pm} i_2)N_s + up \overset{1}{\pm} v\Big]\theta - \\
(u \overset{1}{\pm} 1)p\omega t\Bigg\}
\end{aligned}
\tag{2.42}
$$

$$
\begin{aligned}
p_{st}^{\mathrm{PM\times ARM}}(\theta,t) = \sum_u \sum_v \sum_{i_1} \sum_{i_2} p_{st,uvi_1i_2}^{\mathrm{PM\times ARM}} \sin\Bigg\{\Big[(i_1 \overset{1}{\pm} i_2)N_s + up \overset{1}{\pm} v\Big]\theta - \\
(u \overset{1}{\pm} 1)p\omega t\Bigg\}
\end{aligned}
\tag{2.43}
$$

where $p_{sr,uvi_1i_2}^{\mathrm{PM\times ARM}}$ and $p_{st,uvi_1i_2}^{\mathrm{PM\times ARM}}$ are the amplitudes of the radial and tangential EM force densities generated by the interaction of PM and Armature reaction, respectively.

From the above expressions, it can be seen that the radial and tangential EM forces in the air gap share the same temporal and spatial harmonic components, differing only in amplitude and phase. The spatial orders can be further written as

$$|up \pm v_0 N_0 + iN_s|, \quad i \in \mathbb{Z} \tag{2.44}$$

where $|up|$ originates from the PM fields, $|v_0 N_0|$ originates from the Armature Reaction fields, and $|iN_s|$ originates from the slotting modulation effect. It can be proved that the minimum non-zero spatial order of the air-gap electromagnetic force is $\mathrm{GCD}(2p, N_s)$. Moreover, any spatial order must be an integer multiple of this minimum value, i.e., $k\,\mathrm{GCD}(2p, N_s)$. The temporal orders can be further expressed as

$$|2kp|, \quad k \in \mathbb{Z}_{\geq 0} \tag{2.45}$$

The frequencies are $|2kp|$ times the mechanical frequency, which corresponds to even multiples of the electrical frequency. The slotting effect does not modulate the temporal orders of the electromagnetic force waves.

2.3.4 Total force distribution in different machines

According to (2.35)-(2.45), the temporal and spatial orders of the air-gap electromagnetic force density can be organized into Table 2.3.

Table 2.3: Time and spatial order of force densities

Source	Time order	Spatial Order
PM × PM	$(u_1 \overset{1}{\pm} u_2)p$	$(i_1 \overset{1}{\pm} i_2)N_s + (u_1 \overset{1}{\pm} u_2)p$
ARM × ARM	$p \overset{1}{\pm} p$	$(i_1 \overset{1}{\pm} i_2)N_s + (v_1 \overset{1}{\pm} v_2)$
PM × ARM	$(u \overset{1}{\pm} 1)p$	$(i_1 \overset{1}{\pm} i_2)N_s + up \overset{1}{\pm} v$

In the spatial harmonics of different machines, the values of terms v_1 and v_2 associated with armature reaction vary due to different pole–slot combinations, which leads to differences in the expressions of spatial harmonics. Expressions in Table. 2.3 are still too general to extract a clear quantitative relationship between the temporal and spatial orders. Therefore, in order to obtain the specific insight into each type of machine, the temporal and spatial harmonic orders for different machines can be derived separately from (2.13) and (2.14), as shown in Table 2.4-Table 2.6.

Table 2.4: Time and spatial order of force densities in 10p12s machine

Source	Time order	Spatial Order	
PM × PM	$2kp$	$iN_s + 2kp$	$k, i \in \mathbb{Z}$
ARM × ARM	0	$iN_s + 6k$	$k, i \in \mathbb{Z}$
	$2p$	$iN_s + 6k + 2$	
PM × ARM	$2k_1 p$	$iN_s + 2k_1 p + 6k_2$	$k_1 \in \mathbb{Z}_{\geq 0}, k_2, i \in \mathbb{Z}$

Table 2.5: Time and spatial order of force densities in 8p48s machine

Source	Time order	Spatial Order	
PM × PM	$2kp$	$iN_s + 2kp$	$k, i \in \mathbb{Z}$
ARM × ARM	0	$iN_s + 6kp$	$k, i \in \mathbb{Z}$
	$2p$	$iN_s + (6k+2)p$	
PM × ARM	$2k_1p$	$iN_s + 2k_1p + 6k_2p$	$k_1 \in \mathbb{Z}_{\geq 0}, k_2, i \in \mathbb{Z}$

Table 2.6: Time and spatial order of force densities in 8p12s machine

Source	Time order	Spatial Order	
PM × PM	$2kp$	$iN_s + 2kp$	$k, i \in \mathbb{Z}$
ARM × ARM	0	$iN_s + 3kp$	$k, i \in \mathbb{Z}$
	$2p$	$iN_s + (3k+2)p$	
PM × ARM	$2k_1p$	$iN_s + 2k_1p + 3k_2p$	$k_1 \in \mathbb{Z}_{\geq 0}, k_2, i \in \mathbb{Z}$

In summary, based on the analysis in the previous three sections, the temporal orders of the EM force densities in each type of machine are all even multiples of the pole-pair number, i.e., integer multiples of the pole number. The spatial orders are integer multiples of the greatest common divisor between the slot number and the pole number, i.e., $k\,\mathrm{GCD}(N_s, 2p)$.

Regarding the sources of electromagnetic forces, the temporal–spatial orders of the force components originating from the interaction between PMs are identical for all three machines. This is because the mechanism by which the rotating rotor magnets generate force waves is the same across these machines.

However, the spatial expressions of the force waves generated by the interaction between armature reactions(ARM × ARM) and by the interaction between the PM and the armature reaction(PM × ARM) differ. The harmonic orders caused by armature reaction can be understood from the analysis of the unit machine. For the 8p48s and 8p12s machines, each consists of p unit machines; therefore, when the slotting effect is ignored ($i = 0$), the lowest order of non-zero spatial harmonic of the flux density caused by armature reaction is the pole-pair number p. Moreover, due to the different slot numbers of the unit machines, the 8p12s machine contains richer spatial harmonic orders of flux density—integer multiples of the pole-pair number—whereas the 8p48s machine contains only odd multiples of the pole-pair number. Consequently, in the electromagnetic force density related to armature reaction, both machines have spatial harmonic orders that are multiples of the pole-pair number, but the 8p48s machine includes only even multiples, while the 8p12s machine contains richer harmonic components, i.e., both even and odd multiples.

For the 10p12s machine, its unit machine is the machine itself, so the number of unit machines N_0 is 1. When slotting is ignored, the spatial harmonic orders of the flux density are independent of the pole-pair number. This directly leads to the lowest non-zero spatial harmonic order of flux density being 1, rather than p as in

integral-slot machines. The presence of such low-order harmonic components and absent of pole-pair number p cause this machine to exhibit a much richer set of EM force spatial harmonics when the force originates from armature reaction. In other words, this machine can be regarded as being driven by harmonics.

3

Vibration analysis: From air-gap force to noise and vibration

In the previous chapter, an analytical model of the EM forces in the air gap has been established. This chapter discusses how the electromagnetic forces acting on the stator teeth contribute to the generation of tangential torque ripple as well as axially induced forced vibrations in the motor.

3.1 Tangential force and Torque ripple

The tangential EM force waves are the excitation source of the motor torque. Both the constant component and the pulsating component of the torque can be obtained by performing a circumferential loop integral of the tangential EM force waves along the air-gap, and can be expressed as

$$T_{em}(t) = L_{ef} \oint_l r\, p_{st}(\theta, t)\, \mathrm{d}l = r^2 L_{ef} \int_0^{2\pi} p_{st}(\theta, t)\, \mathrm{d}\theta \tag{3.1}$$

where L_{ef} is the effective length of the machine, $p_{st}(\theta, t)$ is the tangential EM force density, r is the radius of the circumferential air-gap path at which the tangential force wave is evaluated, and l denotes the circular integration path of radius r.

The above equation represents the integral of the tangential electromagnetic force wave $p_{st}(\theta, t)$ with respect to the spatial position over the range 0 to 2π. According to the properties of integration of sinusoidal functions, when the spatial order is non-zero, the integral evaluates to zero. This implies that non-zero spatial-order tangential force waves contribute neither to the constant qorque nor to the torque ripple. For the zero-order tangential electromagnetic force wave, its contribution to the steady or pulsating torque component depends on its temporal order. A tangential electromagnetic force wave with a temporal order of zero contributes to the constant torque, whereas a tangential electromagnetic force wave with a non-zero temporal order becomes the source of torque ripple.

Table 3.1: Time and spatial order of tangential EM forces and corresponding generated torque

Spatial Order	Time order	Torque
Zero	Zero	Constant torque
Zero	Non-zero	Torque ripple
Non-zero	Zero	No torque
Non-zero	Non-zero	No torque

3.1.1 Cogging torque under no-load conditions

When the motor operates under no-load conditions, no armature current flows in the stator windings, and the torque in the air gap is produced solely by the interaction between PMs. The resulting torque ripple under this condition is the cogging torque. According to (2.36) and (3.1), the cogging torque can be expressed as

$$\begin{aligned} T_{cog} &= r^2 L_{ef} \int_0^{2\pi} p_{st}^{\mathrm{PM\times PM}}(\theta, t)\,\mathrm{d}\theta \\ &= \sum_{u_1}\sum_{u_2}\sum_{i_1}\sum_{i_2} r^2 L_{ef} \int_0^{2\pi} p_{st,u_1u_2i_1i_2}^{\mathrm{PM\times PM}} \sin\left\{\Big[(u_1 \pm u_2)p + (i_1 \pm i_2)N_s\Big]\theta - \right. \\ &\left. (u_1 \pm u_2)p\omega t\right\}\mathrm{d}\theta \end{aligned} \tag{3.2}$$

According to the above analysis, if torque ripple exists, then

$$\Big\{(u_1 \pm u_2)p + (i_1 \pm i_2)N_s = 0 \mid (u_1 \pm u_2)p \neq 0\Big\} \tag{3.3}$$

Equation (3.3) implies that when cogging torque is present, i_1 and i_2 cannot both be zero. This demonstrates that the generation of cogging torque necessarily involves the participation of the stator teeth.

In the above equation, let $u_1 \pm u_2 = 2u$ and $i_1 \pm i_2 = -i$, where $u, i \in \mathbb{Z}$. Then,

$$u = i\frac{N_s}{2p} = i\frac{N_s/\mathrm{GCD}(2p, N_s)}{2p/\mathrm{GCD}(2p, N_s)} \tag{3.4}$$

u becomes an integer only when $i = k\frac{2p}{\mathrm{GCD}(2p,N_s)}, \quad k \in \mathbb{Z}$. In this case,

$$u = k\frac{N_s}{\mathrm{GCD}(2p, N_s)}. \tag{3.5}$$

This implies that the spatial harmonic order becomes zero only if the following relationship is satisfied

$$u_1 \pm u_2 = k\frac{2N_s}{\mathrm{GCD}(2p, N_s)}. \tag{3.6}$$

At this time, the temporal order of the cogging torque is

$$\Big|(u_1 \pm u_2)p\Big| = k\frac{2pN_s}{\mathrm{GCD}(2p, N_s)} = k\,\mathrm{LMC}(2p, N_s), \quad k \in \mathbb{N}. \tag{3.7}$$

3.1.2 Torque ripple under load conditions

When the machine operates under load, the tangential EM force originates not only from the interaction between PMs, but also from the interactions among Armature Reactions and from the interactions between the PM and the Armature Reaction. The torque ripple caused by the former has been explained in the previous section, and the following analysis focuses on the torque ripples arising from the latter two types of EM forces.

As can be observed from Table 2.4 - Table.2.6, for each type of machine, the temporal–spatial expressions of the latter two electromagnetic forces can in fact be combined into a single form, as shown in Table 3.2.

Table 3.2: Time and spatial order of $p_{st}^{\mathrm{ARM\times ARM}}$ and $p_{st}^{\mathrm{ARM\times PM}}$ in different machines

Type of machine	Time order	Spatial Order	
10p12s	$2k_1p$	$iN_s + 2k_1p + 6k_2$	$k_1 \in \mathbb{Z}_{\geq 0}, k_2, i \in \mathbb{Z}$
8p48s	$2k_1p$	$iN_s + 2k_1p + 6k_2p$	$k_1 \in \mathbb{Z}_{\geq 0}, k_2, i \in \mathbb{Z}$
8p12s	$2k_1p$	$iN_s + 2k_1p + 3k_2p$	$k_1 \in \mathbb{Z}_{\geq 0}, k_2, i \in \mathbb{Z}$

For 10p12s machine, if torque ripple exists, then

$$\left\{ iN_s + 2k_1p + 6k_2 = 0 \mid 2k_1 \neq 0 \right\} \tag{3.8}$$

$$2k_1p = iN_s + 6k_2 \tag{3.9}$$

where $k_1 \in \mathbb{Z}^+$, $i, k_2 \in \mathbb{Z}$. N_s must be a multiple of 3 in a three phase machine, then

$$k_1 = \frac{3(\frac{iN_s}{6} + k_2)}{p} = \frac{3k_3}{p} = k_3 \frac{3/\mathrm{GCD}(3,p)}{p/\mathrm{GCD}(3,p)} \tag{3.10}$$

where $k_3 \in \mathbb{Z}$. k_1 becomes an integer only when $k_3 = k\frac{p}{\mathrm{GCD}(3,p)}$, $k \in \mathbb{Z}$. In this case,

$$k_1 = k\frac{3}{\mathrm{GCD}(3,p)} = 3k \tag{3.11}$$

In this case, the temporal order of the torque ripple is

$$2k_1p = 6kp, \quad k \in \mathbb{Z}^+ \tag{3.12}$$

Similarly, for the other two machines, it can also be shown that the temporal order of the torque ripple associated with the armature reaction under load is $6kp$

3.2 Radial force and Forced vibration

3.2.1 Modal analysis and natural frequency

Radial force is commonly regarded as the primary source of electromagnetic vibration in rotating machines. The vibration can be regarded as the linear superposition

of a series of forced vibrations excited by sinusoidal electromagnetic forces of different spatial orders. The vibration modes and orders of the machine are defined according to the shape and order of the corresponding radial force. Fig. 3.1 shows the circumferential modes of the circular stator, each corresponding to a specific spatial order of the radial force.

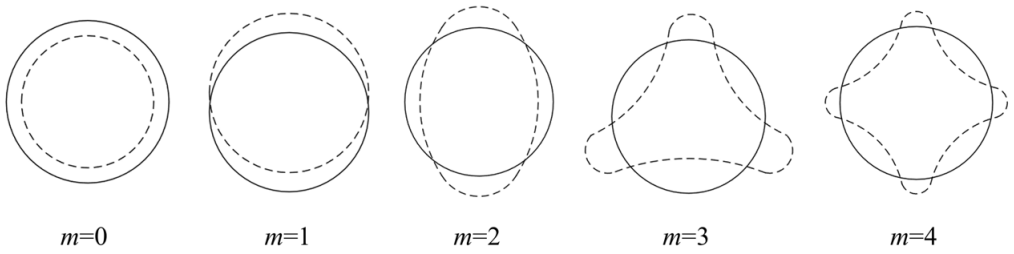

Figure 3.1: Circumferential modes of circular stator

In electric machines, the spatial order of the radial EM force determines which stator vibration mode can be effectively excited, due to the orthogonality of the mode shapes. Each circumferential mode of the stator is associated with a distinct natural frequency. When a radial force component of matching spatial order is applied near the corresponding natural frequency, resonance occurs, resulting in a significantly amplified vibration response for that specific mode. Consequently, the frequency response of each stator mode can be modeled as a band-pass function centered at its natural frequency. The overall stator vibration can therefore be expressed as the superposition of modal responses, each governed by the product of the modal frequency response and the corresponding spatial-order component of the radial force. This relationship is given by

$$x(\omega) = \sum_{m} H_m(\omega)\, p_m(\omega), \tag{3.13}$$

where $H_m(\omega)$ denotes the frequency response function of the m-th circumferential stator mode, $p_m(\omega)$ represents the m-th spatial-order component of the radial electromagnetic force, and $x(\omega)$ is the total vibration response of the stator.

For a vibration system, the vibration response is governed by

$$\mathbf{M}\ddot{\mathbf{x}}(t) + \mathbf{C}\dot{\mathbf{x}}(t) + \mathbf{K}\mathbf{x}(t) = \mathbf{p}(t), \tag{3.14}$$

where $\mathbf{x}$ and $\mathbf{p}$ denote the vibration displacement vector and excitation force vector, and $\mathbf{M}$, $\mathbf{K}$, and $\mathbf{C}$ are the mass, stiffness, and damping matrices, respectively.

By solving the above equation, (3.13) can be further expressed as a function of the modal shapes and the excitation force, namely,

$$x(j\omega) = \sum_{m=1}^{N} \frac{\psi_m^{\mathrm{T}}\, \mathbf{p}(j\omega) \cdot \psi_m}{f_m^2 + 2j\omega\zeta_m f_m - \omega^2}, \tag{3.15}$$

where ψ_m is the mass-normalized mode shape of the m-th mode. ω and f_m denote the excitation angular frequency and the natural frequency of the m-th mode, and ζ_m is the corresponding damping ratio.

3.2.2 Spatial order and vibration amplitude

From previous section, the vibration response of the stator can be regarded as a function of the excitation frequency f, the structural mode m, and the EM force p_m. However, when the natural frequencies of the stator-housing assembly do not lie within the operating frequency range of the machine, the excitation frequency no longer dominates the vibration behavior. In such cases, the influence of the modal characteristics and the spatial distribution of the excitation force can be assessed by analyzing the static deformation pattern under forces of different spatial orders. This approach enables a clear evaluation of how the mode shape and the corresponding excitation component contribute to the resulting vibration.

Assuming a uniform mass distribution of the stator, with the stator teeth and windings equivalent to additional mass attached to the stator. The stator is modeled as a slotless ring structure, and only the deformation of the stator yoke is considered. Under these assumptions, the static deformation of the stator can be simplified as the bending deformation of a simply supported beam subjected to a sinusoidally distributed load. The amplitude of the deformation caused by radial electromagnetic force can then be expressed as

$$Y_{m=0} = \frac{R_y R P_{m=0}}{E T_y} \tag{3.16}$$

$$Y_{m\geq 2} = \frac{12 R_y^3 R P_{m\geq 2}}{E T_y^3 (m^2-1)^2} \tag{3.17}$$

where R is the inner radius of stator, R_y is the average yoke radius, T_y is the thickness of yoke, E is Young's modulus, P_m is the magnitude of mth radial force, and subscript m here denotes number of mode order.

It can be concluded that the deformation is inversely proportional to the 4th power of mode order, which indicates that the amplitude will drop rapidly with mode order. For integer-slot machines or machines with a unit motor number greater than one (8p48s and 8p12s), the minimum non-zero spatial order of the electromagnetic force is $2p$. This indicates that the minimum forced-vibration mode that can be excited by the electromagnetic force is also of order $2p$. In most cases, this value is greater than four, resulting in very small vibration amplitudes for the corresponding modes. In contrast, fractional-slot machines (10p12s) exhibit a minimum non-zero spatial force order of two, which leads to significantly larger vibration amplitudes. Furthermore, when the mass and structural characteristics are comparable, the natural frequencies of non-zero-order modes increase with increasing modal order. Consequently, the operating frequency range of many integer-slot machines lies below their lowest relevant natural frequency, making resonance less likely to occur compared with fractional-slot machines. Therefore, integer-slot machines are generally regarded as having better NVH performance for the same torque capability.

3.3 Mechanical modulation by stator teeth: From air-gap force to tooth force

In the previous chapter, the analytical model of the electromagnetic force was established in the air gap, yielding a continuous force distribution spatially along the circumference. However, the direct excitation that induces forced vibrations in the stator is the radial electromagnetic force acting on the stator tooth surface. Due to the presence of stator slot openings, the electromagnetic force on the teeth is inherently discontinuous. Therefore, the air-gap force model and the temporal–spatial harmonics extracted from it cannot be directly used as excitation sources for stator vibration. To obtain accurate temporal–spatial harmonics on the stator teeth, it is necessary to develop a dedicated model for the tooth-surface electromagnetic force. There are two ways to view and derive the electromagnetic force on the stator teeth, which will be discussed separately below.

3.3.1 Concentrated force and aliasing of EM force

Usually, the modulation effect of stator teeth on the air-gap EM force waves is regarded as a down-sampling process in space, with the stator tooth number as the spatial sampling frequency. Within the interval corresponding to each stator tooth, the force density distributed on the tooth surface is integrated along the circumferential direction to obtain the concentrated force on each tooth. This force is then mapped onto the midline of the tooth tip, transmitted through the stator tooth to the stator yoke, and ultimately induces vibration. As illustrated in Fig. 3.2, the concentrated force on each tooth can be expressed as

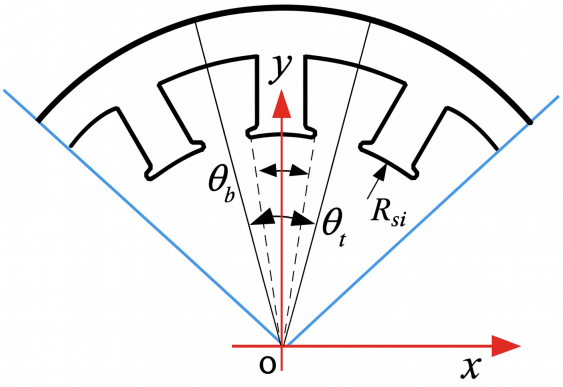

Figure 3.2: Integral path of one tooth

$$F_{sr,i}(t) = R_{si} L \int_{\frac{2\pi}{N_s} i - \frac{1}{2}\theta_b}^{\frac{2\pi}{N_s} i + \frac{1}{2}\theta_b} p_{sr}(\theta, t)\, d\theta \tag{3.18}$$

where R_{si} is the inner radius of slot teeth, L is the stack length of the motor. θ_b is the angular span occupied by each stator tooth, and $\theta_b = k_e \theta_t = k_e \frac{2\pi}{N_s}$, where k_e is the embrace coefficient which describes the ratio between tooth width and tooth

pitch. Then (3.19) becomes

$$F_{sr,i}(t) = R_{si}L \int_{\frac{2i-k_e}{N_s}\pi}^{\frac{2i+k_e}{N_s}\pi} p_{sr}(\theta, t)\, d\theta \tag{3.19}$$

The above expression indicates that the magnitude of the concentrated radial force acting on each tooth depends on the slot number N_s and the embrace coefficient k_e.

According to the sampling theorem, the stator with N_s teeth can exhibit only vibration modes up to the $\frac{N_s}{2}$th order. If the order of the radial air-gap force exceeds $N_s/2$, aliasing will occur after being sampled by the stator teeth, and the high-order components will be shifted into lower-order radial forces.

$$m_s = \begin{cases} m, & m \leq N_s/2 \\ |nN_s - m|, & m > N_s/2 \end{cases} \tag{3.20}$$

where m_s is the mode order on the stator yoke, m is the mode order in air-gap, n ensures that $|nN_s - m|$ does not exceed $N_s/2$.

The aliasing effect of the stator teeth can be illustrated by Fig. 3.3. The second mode EM force in the air gap remains in the second mode after being modulated by the 12 stator teeth. The 10th-order electromagnetic force in the air gap is aliased after the 12-tooth modulation and also appears as a second mode. The 12th-order EM force is modulated to a 0th-order mode, which is also referred to as the breathing mode.

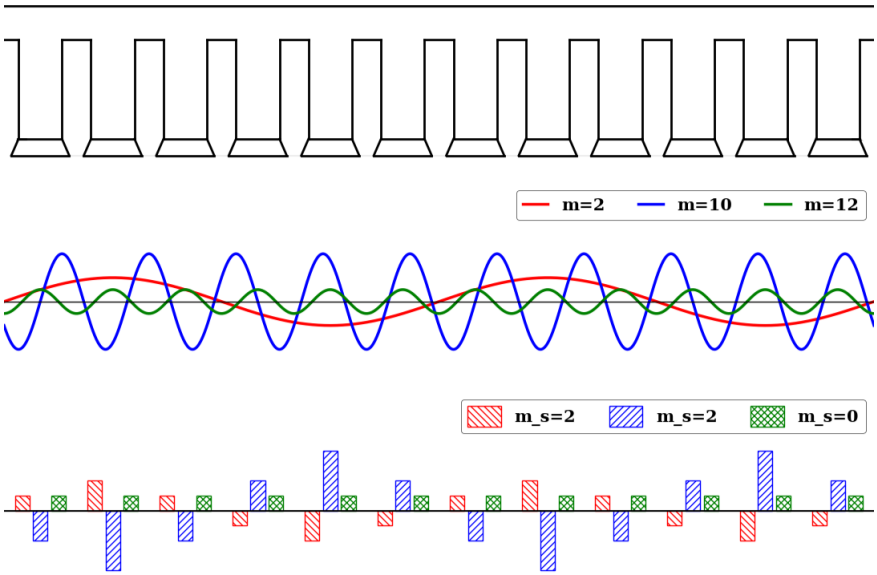

Figure 3.3: Illustration of the aliasing effect of motor stator teeth. (a) Slotted stator. (b) Air-gap radial forces with $v = 2$, 10 and 12. (c) Equivalent concentrated radial force distributions along the tooth.

3.3.2 Distributed force and modulation of EM force

A second approach regards the stator-tooth force as a distributed load acting on the tooth-tip surface rather than as a concentrated force. This representation preserves the spatial variation of the air-gap EM force within each tooth segment. Similar to the modulation of flux density caused by the stator teeth, the radial EM force is also mechanically modulated by the slotting. This modulation can be described by multiplying the original air-gap force by a square-wave function that equals 1 over the tooth regions and 0 over the slot openings, as

$$p_{sr}^{\mathrm{mod}}(\theta,t) = p_{sr}(\theta,t)\, m(\theta) \tag{3.21}$$

$$m(\theta) = \begin{cases} 1, & \frac{2\pi}{N_s} i - \frac{k_e}{2}\frac{2\pi}{N_s} \le \theta \le \frac{2\pi}{N_s} i + \frac{k_e}{2}\frac{2\pi}{N_s}, \quad \text{tooth region} \\ 0, & \frac{2\pi}{N_s} i + \frac{k_e}{2}\frac{2\pi}{N_s} \le \theta \le \frac{2\pi}{N_s}(i+1) - \frac{k_e}{2}\frac{2\pi}{N_s}, \quad \text{slot opening} \end{cases} \tag{3.22}$$

where $p_{sr}^{\mathrm{mod}}(\theta,t)$ denotes the modulated tooth-force wave, $m(\theta)$ is the modulation function, and i is the stator-tooth index ranging from 0 to $N_s - 1$. Since (3.22) is periodic, it can be expanded in a Fourier series as

$$\begin{aligned} m(\theta) &= k_e + \sum_{w=1}^{\infty} \frac{2}{w\pi} \sin\Big(w\pi k_e\Big) \cos\Big(wN_s\theta\Big) \\ &= \sum_{w=0}^{\infty} M_{w,k_e} \cos\Big(wN_s\theta\Big) \end{aligned} \tag{3.23}$$

where M_{w,k_e} denotes the magnitude of wth harmonic of teeth modulation function. Substituting (3.23) into (3.21),

$$p_{sr}^{\mathrm{mod}}(\theta,t) = \sum_m \sum_n \sum_w \frac{1}{2} p_{sr,mn} M_{w,k_e} \cos\Big[(m \pm wN_s)\theta - nt\Big] \tag{3.24}$$

where $p_{sr,mn}$ is the magnitude of air-gap EM force with spatial order as m and temporal order as n. (3.24) indicates that the stator's modulation effect scales the original (m,n)-order electromagnetic force harmonic by a factor of M_{w,k_e}, and shifts it in space by wN_s. The variation of $|M_{w,k_e}|$ with respect to w and k_e is illustrated in Fig. 3.4.

Overall, the magnitude of M_{w,k_e} decreases as w increases, indicating that the low-order slotting components(fundamental components) dominate the modulation effect. For a fixed harmonic order w, the magnitude of M_{w,k_e} varies w times as the embrace coefficient k_e changes. Moreover, according to (3.23), when $w = 0$, the air-gap EM force is affected only by the amplitude modulation introduced by slotting. In this case, $M_0 = k_e$, and no spatial shift is produced. From the above discussion, the variation of a given teeth modulated harmonic with respect to k_e can be used to identify which air-gap harmonics contribute to that modulated component. The detailed analysis will be presented in Chapter 5.

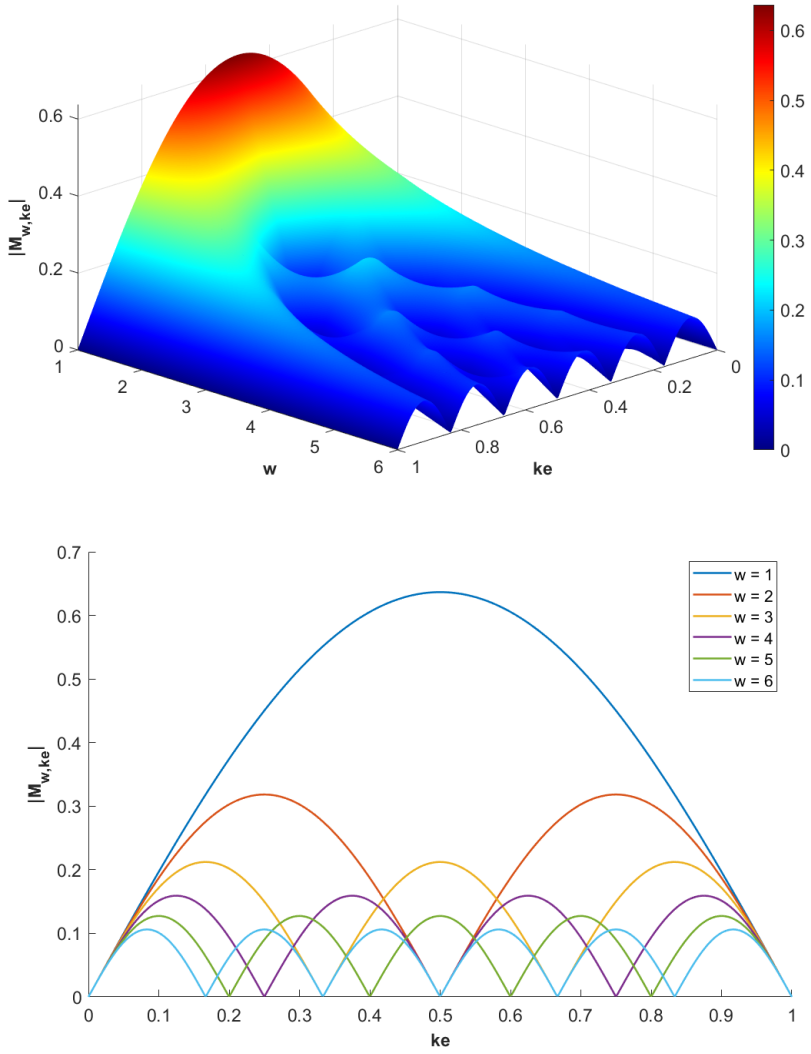

Figure 3.4: The variation of $|M_{w,k_e}|$ with respect to w and k_e

4

Case Setup

4.1 Machine configurations

4.1.1 Sizing

This study investigates three different electric machines: an 8p12s FSCW SPM machine, a 10p12s FSCW SPM machine, and an 8p48s ISDW IPM machine. Among them, the two SPM machines share identical stator and rotor geometries; they differ only in the winding configuration and the number of permanent-magnet pole pairs. The geometric parameters of the machines are listed in Table 4.1.

Table 4.1: Key geometric parameters of the investigated machines

Parameter	**SPM Machine**	**IPM Machine**
Air-gap length (mm)	4.55	1.10
Stator inner diameter (mm)	41.4	85.2
Stator outer diameter (mm)	62.3	125.0
Permanent magnet thickness (mm)	4.0	–
Rotor outer diameter (mm)	36.85	84.1
Effective axial length (mm)	119.0	129.4
Embrace ratio	0.93	0.76

4.1.2 Winding configurations

The winding configuration constitutes the most significant difference among the three investigated machines. All winding layouts are designed following the principle of maximizing the winding factor corresponding to the working harmonic (pole-pair-order harmonic). The winding configurations of the three machines are shown in Fig. 4.1.

For the 8p12s and 8p48s machines, the selected winding configurations are designed to maximize the fundamental harmonic component of the unit machine, which is also the pth harmonics of the entire machine. By contrast, for the 10p12s machine, the winding configuration is optimized to enhance the fifth-order spatial harmonic of the unit machine, whose rotating direction is opposite to that of the fundamental harmonic.

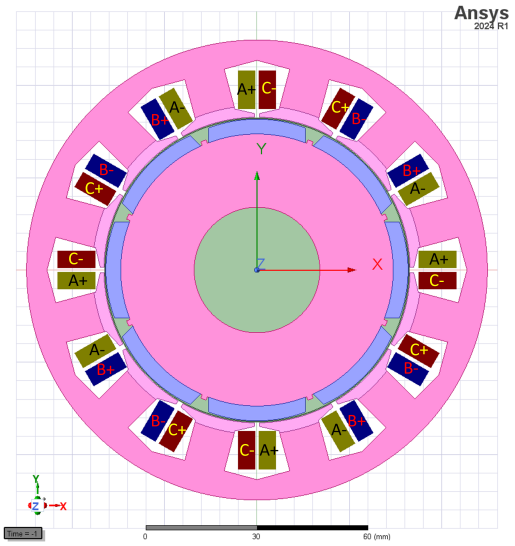

(a) Winding configuration for 8p12s motor

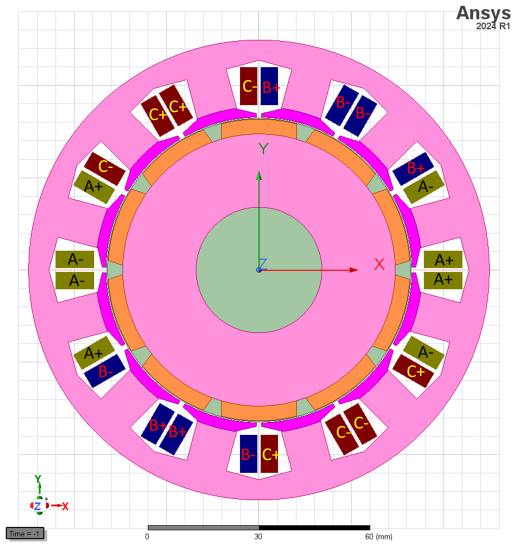

(b) Winding configuration for 10p12s motor

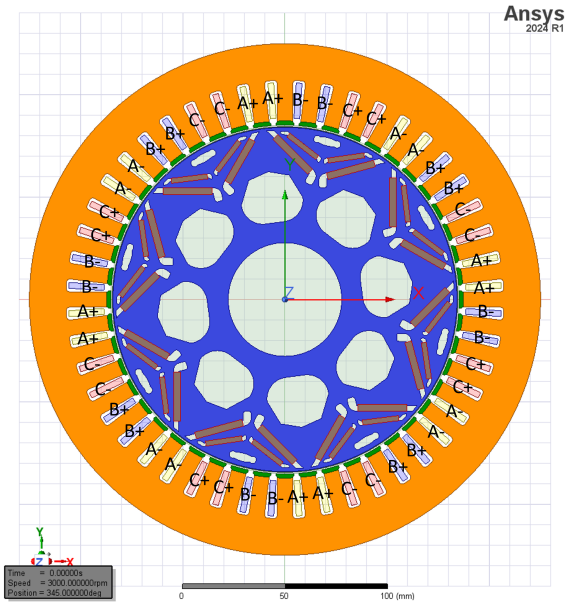

(c) Winding configuration for 8p48s motor

Figure 4.1: Winding Configurations

4.2 2D Electromagnetic simulation setup

4.2.1 Materials

Materials used in this study are shown in Table. 4.2.

Table 4.2: Material specifications of the investigated machines

Component	IPM Machine	SPM Machine
Winding conductor	Copper	Copper
Stator core material	NO25_C	SURA M235-35A
Rotor core material	NO25_C	SURA M235-35A
Permanent magnet	N36Z_20	NdFeB
Housing material	Aluminum	Aluminum

In this study, iron core losses are not taken into account, and the corresponding B–H-curve of NO25_C and SURA M235-35A are presented in Fig. 4.2.

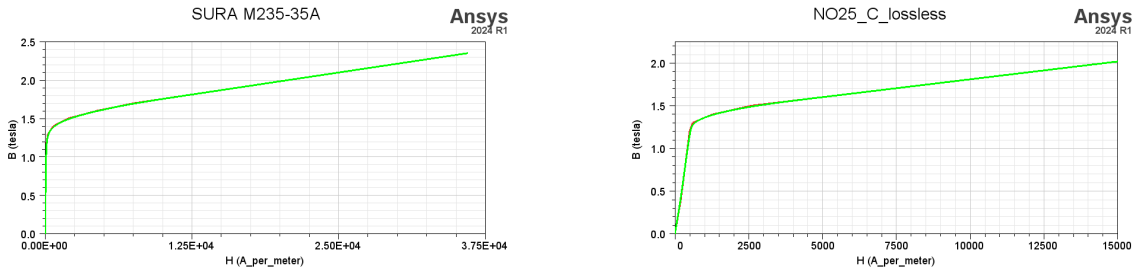

(a) SURA M235-35A B–H-curve **(b)** NO25_C B–H-curve

Figure 4.2: Material Characteristics

4.2.2 Meshing

The mesh of the entire computational domain and the refined mesh in the air-gap region are illustrated in Fig. 4.3. The maximum element size of the global mesh is set to 10 mm, while a finer mesh with an element size of 0.5 mm is applied in the vicinity of the stator teeth. The electromagnetic field in the air gap is obtained by sampling along a circular poly-line located within the air gap and adjacent to the stator teeth. For the SPM machine, this circular path is discretized into 960 segments, corresponding to a maximum resolvable spatial harmonic order of 480. For the IPM machine, the circular path consists of 1920 segments, enabling the extraction of spatial harmonics up to the 960th order.

4.2.3 Simulation setup

The simulation operating conditions for both the IPM and SPM machines are summarized in Table 4.3. The winding excitation is set to current excitation in this study. The current harmonics introduced by pulse-width modulation (PWM) are

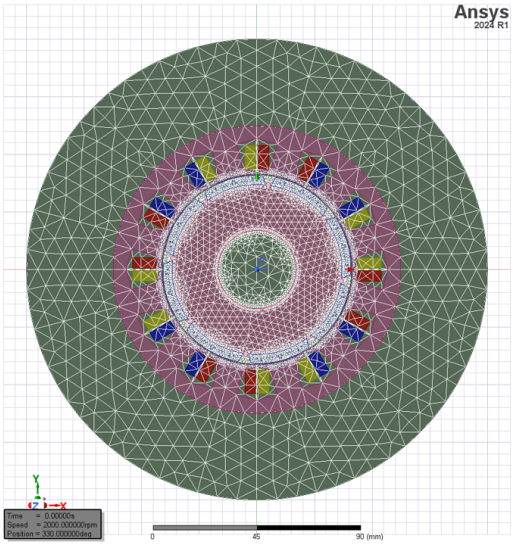

(a) Full mesh 8p12s

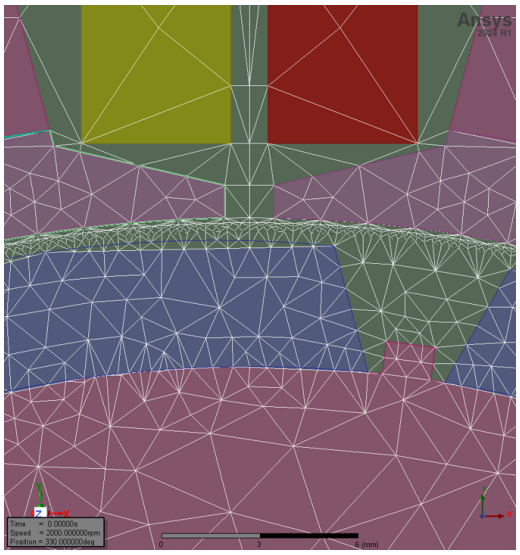

(b) Detailed mesh 8p12s

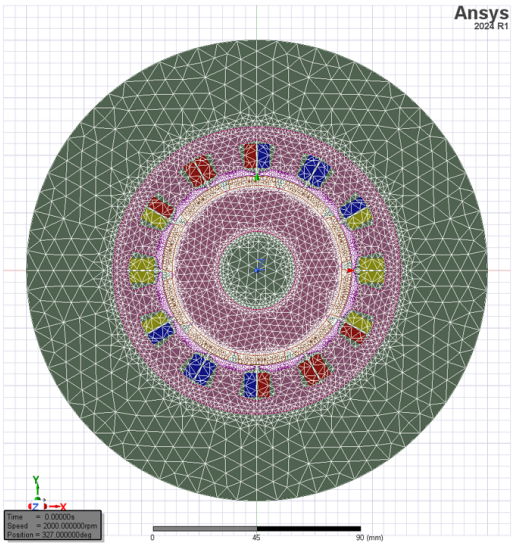

(c) Full mesh 10p12s

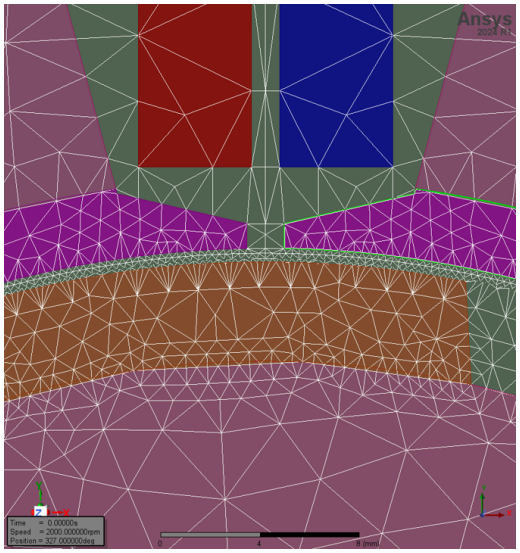

(d) Detailed mesh 10p12s

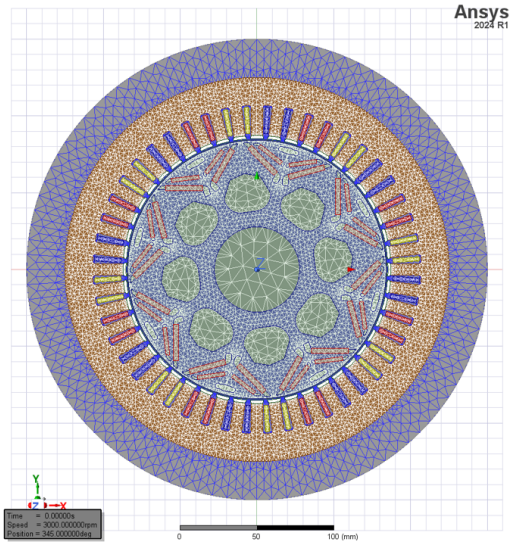

(e) Full mesh 8p48s

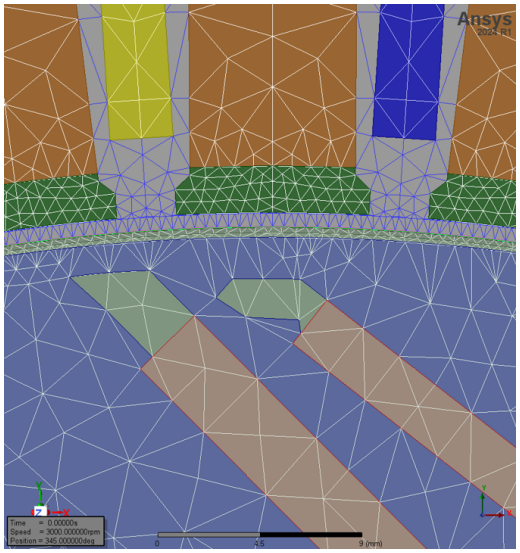

(f) Detailed mesh 8p48s

Figure 4.3: Full mesh and detailed mesh in air-gap

neglected, and the currents flowing through the windings are assumed to be ideal sinusoidal waveforms. Unless otherwise specified, the air-gap electromagnetic fields are extracted under the operating conditions listed in Table 4.3.

In addition to the on-load electromagnetic field, the no-load magnetic field and the armature reaction field are also investigated using both slotted and slotless models. For the extraction of the no-load magnetic field, the armature current is set to zero. For the armature reaction field, the permanent magnets are replaced by air. The slotless model is obtained by filling the slot regions with material identical to the stator core, except for the winding regions, as illustrated in Fig. 4.4.

Table 4.3: Simulation operating conditions of the investigated machines

Parameter	**IPM Machine**	**SPM Machine**
Phase current amplitude (A)	500	34.9
Rotational speed (rpm)	3000	2000
Current angle (deg)	135	135
Simulation time	1 mechanical revolution	1 mechanical revolution
Time step	electrical revolution/120	electrical revolution/120

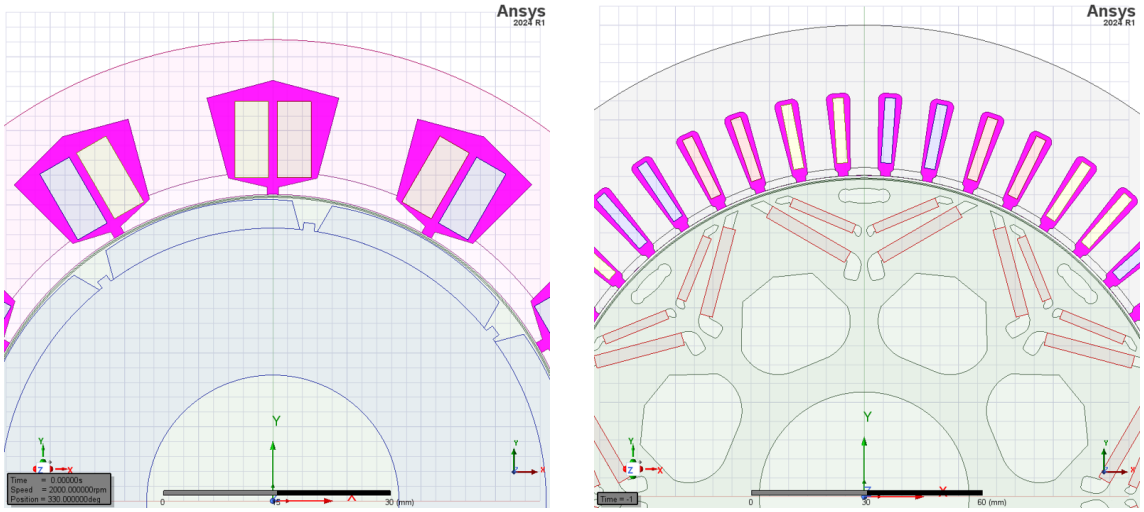

(a) Slotless model of SPM **(b)** Slotless model of IPM

Figure 4.4: Slotless Model

4.3 3D Modal analysis setup

A three-dimensional modal analysis is performed for the assembled stator-housing structure. For all three machines, the housing is simplified as a thin cylindrical shell with an identical thickness of 13 mm, an axial length of 200 mm, and an aluminum-alloy material. An interference fit is assumed between the stator and the housing; therefore, the contact interface is defined as *bonded*, indicating that

no relative displacement or sliding is allowed across the interface. A *fixed support* boundary condition is applied to one end face of the housing, as shown in Fig. 4.5. This boundary condition represents the practical mounting of the motor on a rigid base and eliminates the first six rigid-body modes associated with translational and rotational degrees of freedom. The mesh element size is set to 2 mm and 4 mm respectively. The first 50 natural modes are computed to facilitate modal characterization and subsequent coupling with the electromagnetic simulation results for harmonic response analysis. The simulation settings are summarized in Table 4.4.

Table 4.4: Structural modeling and modal analysis settings

Parameter	**SPM Machine**	**IPM Machine**
Housing geometry	Thin cylindrical shell	Thin cylindrical shell
Housing thickness (mm)	13	13
Housing length (mm)	200	200
Housing material	Aluminum alloy	Aluminum alloy
Boundary condition	Fixed support on one end face	Fixed support on one end face
Stator–housing contact	Bonded	Bonded
Mesh element size (mm)	2	4
Number of modes	First 50 modes	First 50 modes

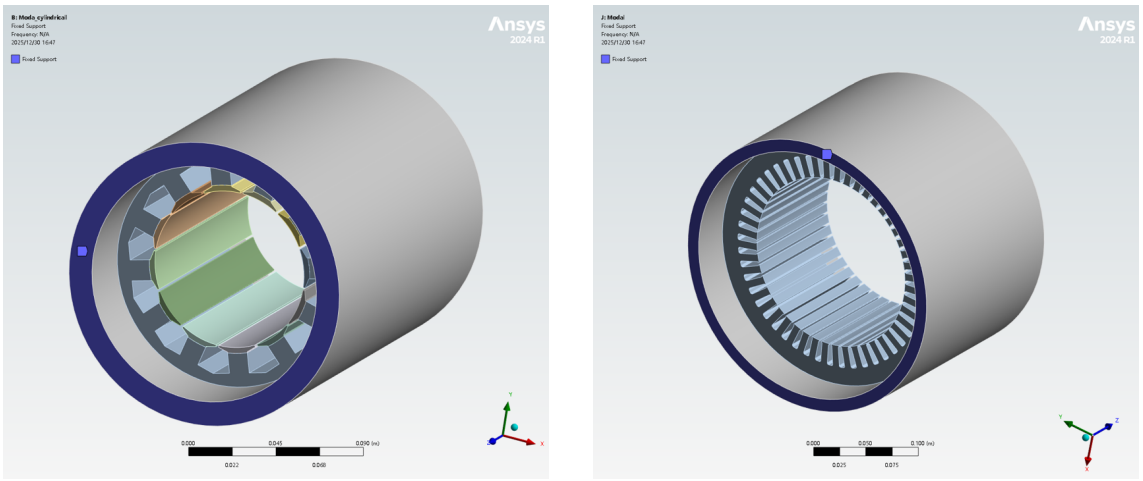

(a) Fixed support in SPM **(b)** Fixed support in IPM

Figure 4.5: Stator-housing structure and fixed support

4.4 Coupled field FEA and Harmonic response

The electromagnetic forces acting on the stator tooth surfaces are obtained from 2D electromagnetic simulations. These forces are treated as concentrated forces, and the frequency responses of the forces acting on each tooth are mapped onto the corresponding stator teeth of the 3D structural model. By combining the mapped electro-

magnetic forces with the results of the modal analysis, the coupled electromagnetic–mechanical vibration response can be obtained.

Based on this framework, a speed sweep is performed in the electromagnetic simulations while keeping the phase current unchanged. Consequently, the harmonic vibration responses of the machines over the entire speed range under constant torque operation can be derived in the form of waterfall plots. The simulation settings are summarized in Table 4.5.

Table 4.5: Speed sweep and frequency analysis settings for the investigated machines

Parameter	**8p48s**	**8p12s**	**10p12s**
Speed range (rpm)	500-8000	200-2000	200-2000
Speed step (rpm)	500	200	200
Frequency range	0-120f_m	0-240f_m	0-300f_m
Frequency step	4f_m	8f_m	10f_m

5

Analysis

In this chapter, the models and theories presented in Chapters 2 and 3 are validated and analyzed using the results of FEM simulations. A comparative analysis of the EM field, EM force, mechanical vibration, and torque ripple in different types of electrical machines will be carried out.

5.1 Flux density in slotless models

5.1.1 Flux density produced by PM

Firstly, the magnetic field produced by the rotor PMs in a slotless machine model is examined. Fig. 5.1 shows the instantaneous air-gap flux distribution for several machine types. The flux varies periodically along the circumference, and one mechanical revolution contains p flux periods, where p is the pole-pair number. This indicates that the PM-excited air-gap flux in the slotless model has a spatial fundamental harmonic of order p.

Fig. 5.2 shows the spatial distribution of the radial air-gap flux density along the circumference at a given time instant, as well as its temporal variation at the centerline of stator tooth over one mechanical period. The flux density waveforms in one mechanical period exhibit similar shapes, implying that the temporal and spatial harmonics of the air-gap flux density have the same harmonic orders. Moreover, these harmonics appear at integer multiples of the pole-pair number p.

A two-dimensional FFT is applied to the radial and tangential air-gap flux densities in both time and space, and the resulting spatiotemporal harmonic components for the three machines are shown in Fig. 5.3. For all machines, the flux-density harmonics lie along the diagonal, indicating that the temporal and spatial harmonics share the same orders, consistent with the earlier analysis. This also shows that different winding configurations do not affect the distribution of the PM-generated field. It is further observed that the 8p48s machine exhibits slightly lower air-gap flux density, particularly in the tangential component. This reduction arises from the rotor structure: in the IPM machine, the permanent magnets are not directly exposed to the air gap, causing the main part of magnet flux to return through the rotor yoke rather than entering the air gap.

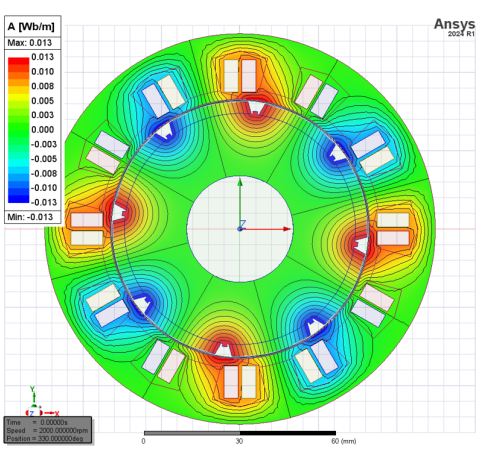

(a) Flux lines in 8p12s motor

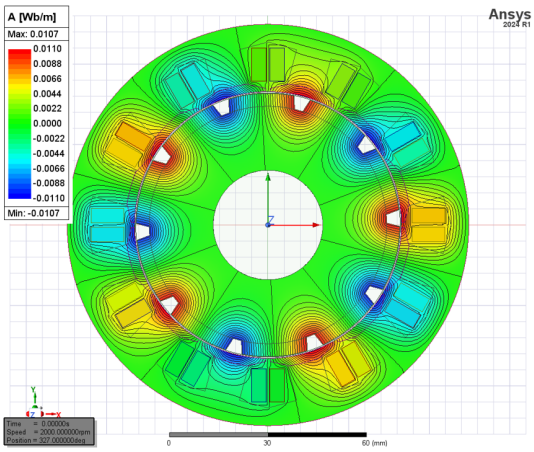

(b) Flux lines in 10p12s motor

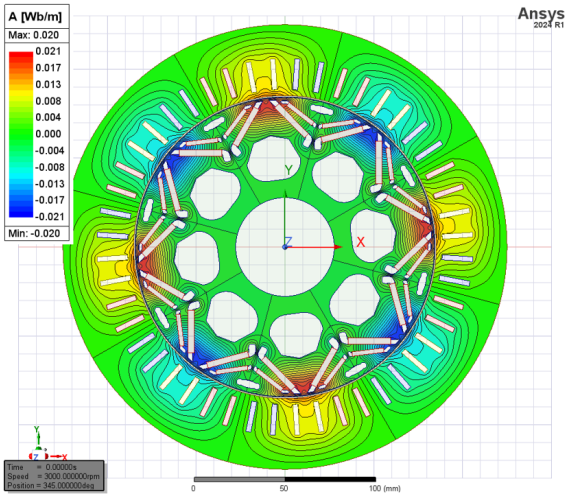

(c) Flux lines in 8p48s motor

Figure 5.1: Flux distributions by PM in slotless models

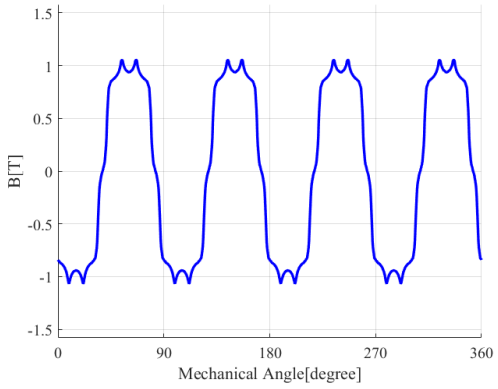

(a) Spatial distribution of B_r^{PM} in 8p12s motor

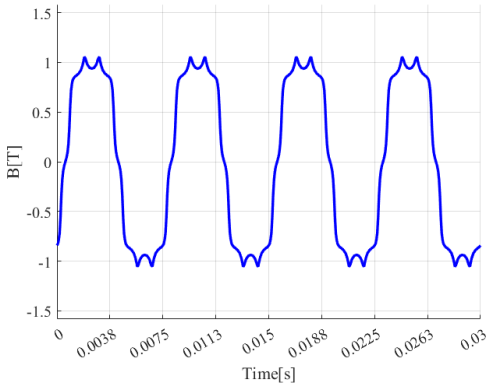

(b) Temporal distribution of B_r^{PM} in 8p12s motor

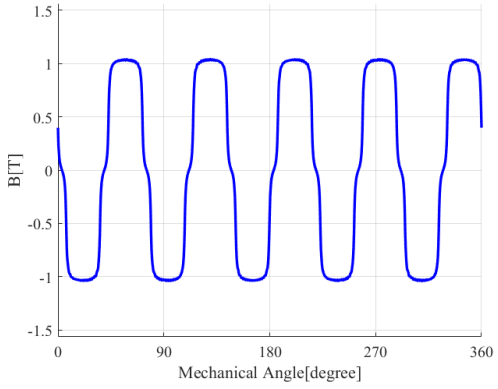

(c) Spatial distribution of B_r^{PM} in 10p12s motor

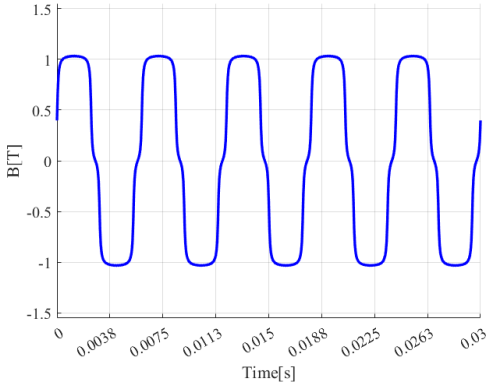

(d) Temporal distribution of B_r^{PM} in 10p12s motor

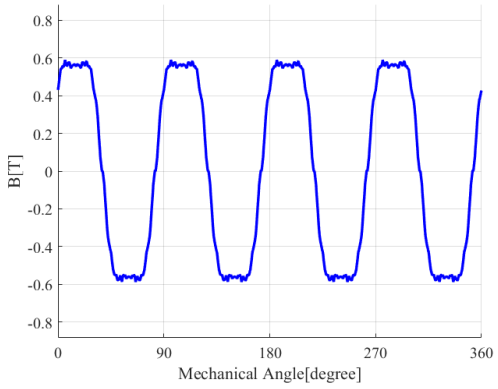

(e) Spatial distribution of B_r^{PM} in 8p48s motor

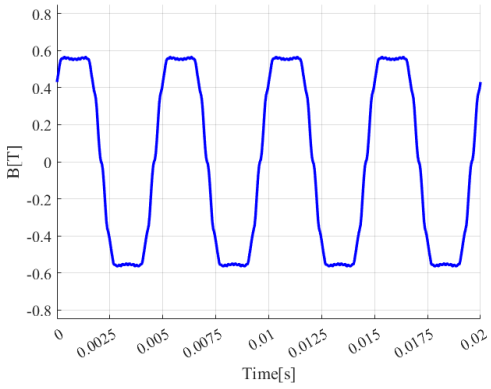

(f) Temporal distribution of B_r^{PM} in 8p48s motor

Figure 5.2: Spatial and Temporal distribution of the PM excited radial flux density in slotless models

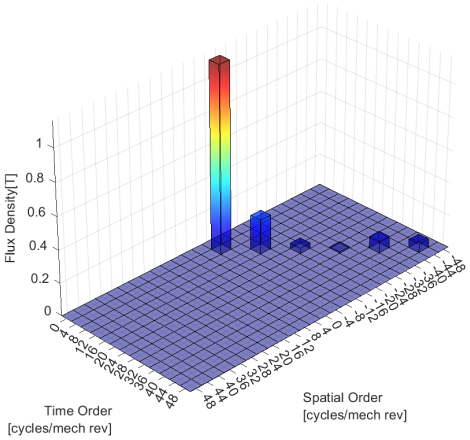

(a) Spatial and Temporal harmonics of B_r^{PM} in 8p12s motor

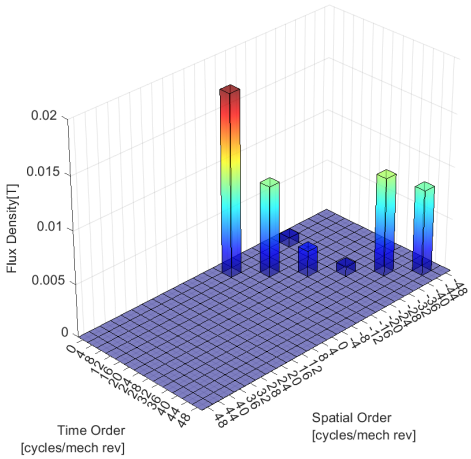

(b) Spatial and Temporal harmonics of B_t^{PM} in 8p12s motor

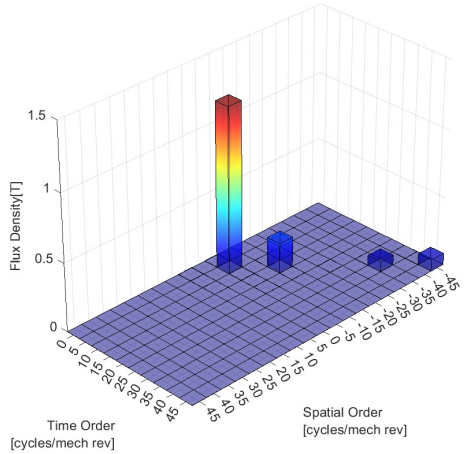

(c) Spatial and Temporal harmonics of B_r^{PM} in 10p12s motor

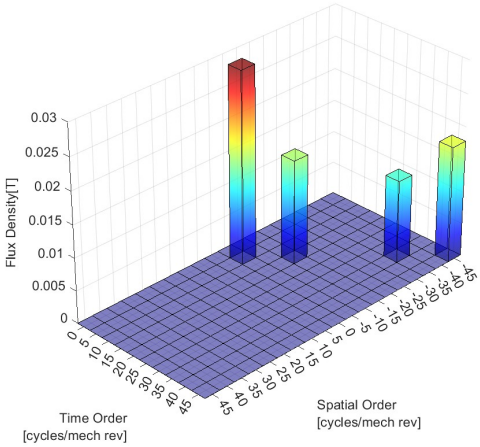

(d) Spatial and Temporal harmonics of B_t^{PM} in 10p12s motor

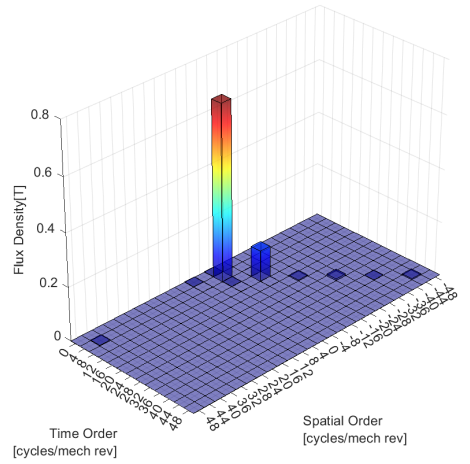

(e) Spatial and Temporal harmonics of B_r^{PM} in 8p48s motor

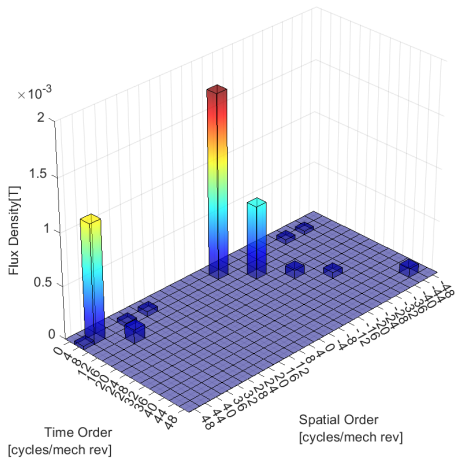

(f) Spatial and Temporal harmonics of B_t^{PM} in 8p48s motor

Figure 5.3: Spatial and Temporal harmonics of flux density excited by PM in slotless motors

5.1.2 Flux density produced by Armature Reaction

The distribution of the armature-reaction field in the slotless model is examined next. Fig. 5.4 presents the instantaneous flux distribution produced by the armature currents in the three slotless machine models. In the 8p12s and 8p48s machines, the air-gap field contains p spatial periods, corresponding to the pole-pair number. However, in the 10p12s machine, only one spatial period appears around the entire circumference. This behavior is determined by the number of unit machines associated with the armature field. The first two machines contain p unit machines, each generating a fundamental spatial harmonic of order one; the superposition of these p phase-shifted components results in a pth-order field. In contrast, the 10p12s machine consists of only one unit machine, and therefore retains a first-order air-gap field as its lowest spatial harmonic.

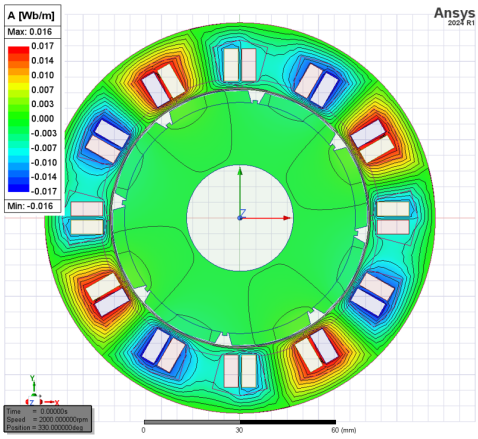

(a) Flux lines in 8p12s motor

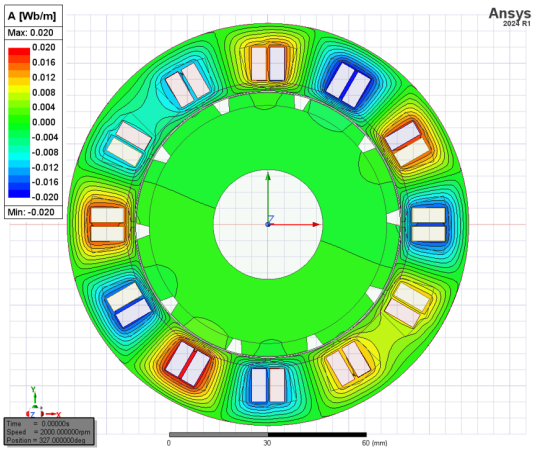

(b) Flux lines in 10p12s motor

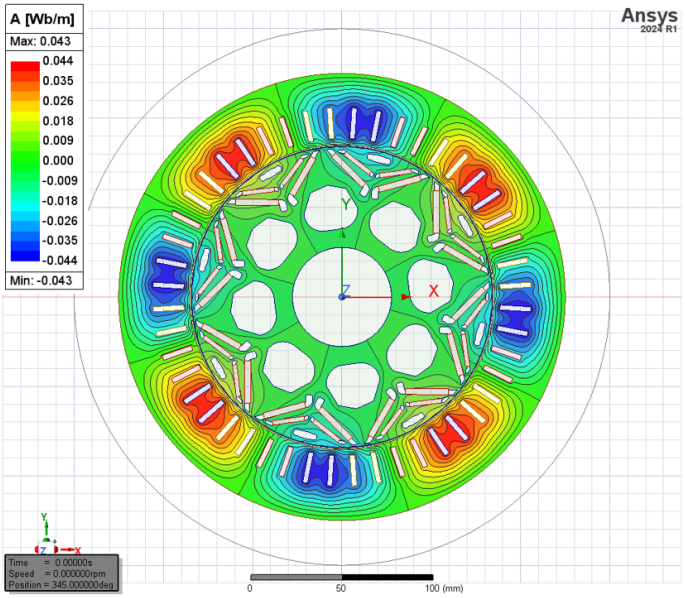

(c) Flux lines in 8p48s motor

Figure 5.4: Flux distributions by Armature Reaction in slotless models

Fig. 5.5 shows the spatial distribution of the Armature Reaction field along the circumference at a given instant and its temporal variation at the stator tooth centerline over one mechanical period. The spatial distributions follow the periodicity predicted earlier for all three machines. Although both the 8p12s fractional slot machine and the 8p48s integer slot machine exhibit a spatial period of p, the flux density waveform of the 8p48s machine is half-wave symmetric, while that of the 8p12s machine is not. As a result, the armature reaction field of the 8p48s machine contains no even order spatial harmonics, whereas even order components appear in the 8p12s machine. The temporal distributions are approximately sinusoidal and contain p periods within one mechanical cycle for all three machines, indicating that the dominant temporal harmonic is of order p.

Fig. 5.6 presents the 2-D FFT results of the armature-reaction field in the slotless models. The dominant components appear at the temporal order p. For the 8p12s machine, the lowest spatial order is $p = 4$, and harmonics with the same temporal order are separated by $3kp$ in space. In the 10p12s machine, the lowest spatial order is 1, and harmonics are spaced by $6k$. In the 8p48s machine, the lowest spatial order is again $p = 4$, with harmonic spacing of $6kp$. These results are consistent with the analytical model. It is also observed that the strongest spatial component in the 10p12s machine occurs at order $p = 5$ rather than at the fundamental spatial order of 1, indicating that the 5th spatial harmonic serves as the effective fundamental component, while the 1st-order component behaves as a lower-order harmonic that may affect mechanical smoothness.

In addition to the dominant components at temporal order p, smaller sideband components appear along shifted diagonal lines in Fig. 5.6. For the 8p12s and 8p48s machines, these sidebands correspond to spatial and temporal shifts of $2kp$. For the 10p12s machine, they correspond to spatial shifts of $2k$ and temporal shifts of $2kp$. These components arise from core saturation induced by the armature current, which periodically modifies the magnetic reluctance.

The results demonstrate that the analytical slotless model accurately captures the simulated magnetic-field behavior. The PM-generated spatiotemporal harmonics remain essentially unchanged across different slot–pole combinations; the main variations arise from the armature-reaction field. In particular, the 10p12s machine introduces a 1st-order spatial harmonic through armature reaction, which becomes a significant consideration in vibration analysis.

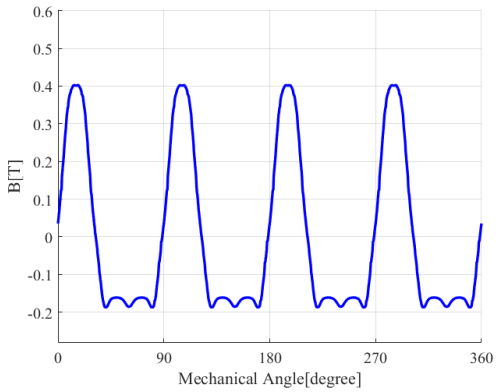

(a) Spatial distribution of B_r^{ARM} in 8p12s motor

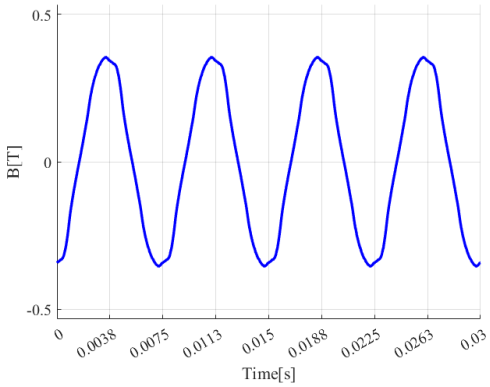

(b) Temporal distribution of B_r^{ARM} in 8p12s motor

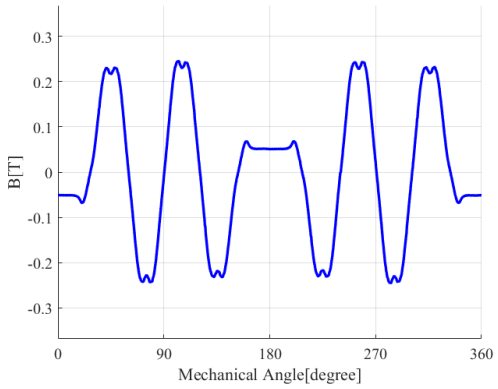

(c) Spatial distribution of B_r^{ARM} in 10p12s motor

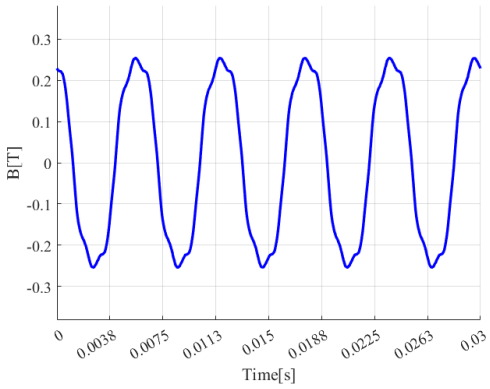

(d) Temporal distribution of B_r^{ARM} in 10p12s motor

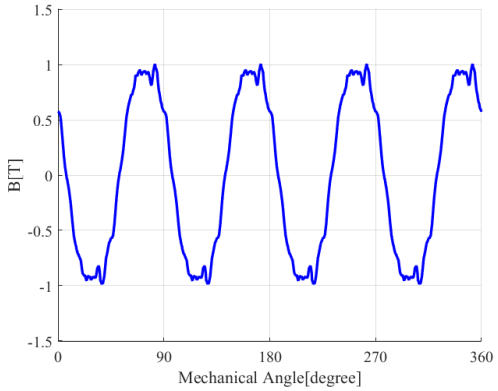

(e) Spatial distribution of B_r^{ARM} in 8p48s motor

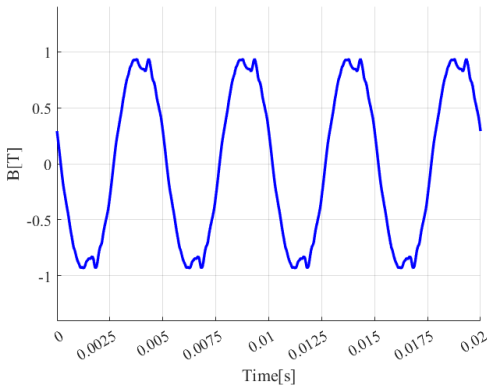

(f) Temporal distribution of B_r^{ARM} in 8p48s motor

Figure 5.5: Spatial and Temporal distributions of armature excited radial flux density in slotless models

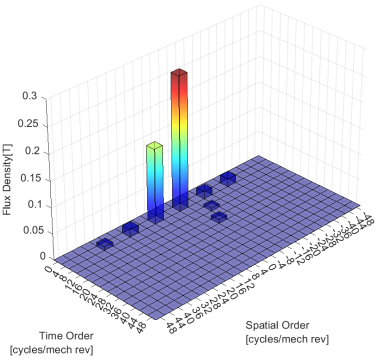

(a) Spatial and Temporal harmonics of B_r^{ARM} in 8p12s motor

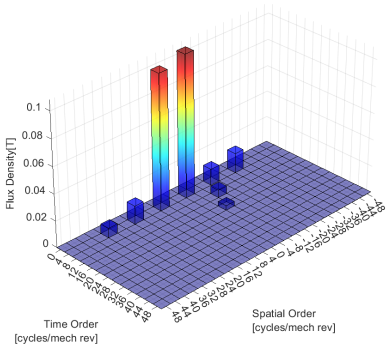

(b) Spatial and Temporal harmonics of B_t^{ARM} in 8p12s motor

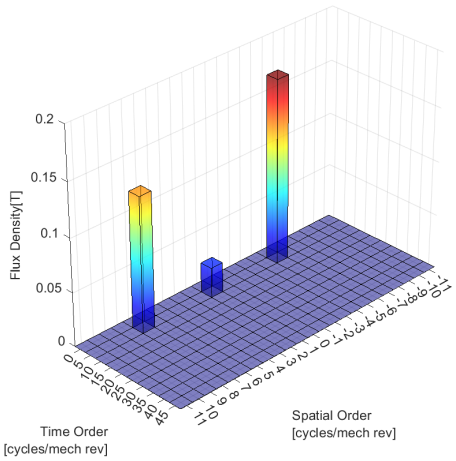

(c) Spatial and Temporal harmonics of B_r^{ARM} in 10p12s motor

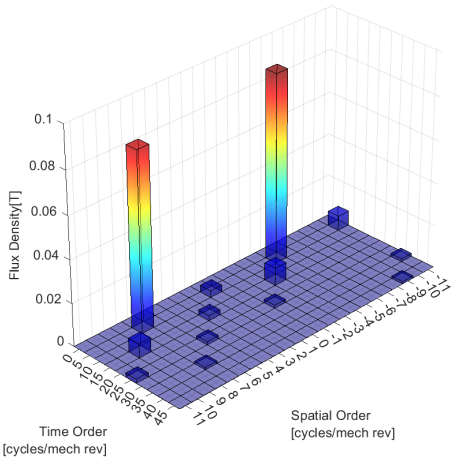

(d) Spatial and Temporal harmonics of B_t^{ARM} in 10p12s motor

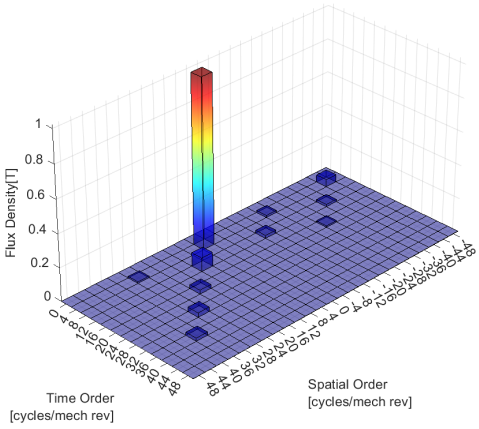

(e) Spatial and Temporal harmonics of B_r^{ARM} in 8p48s motor

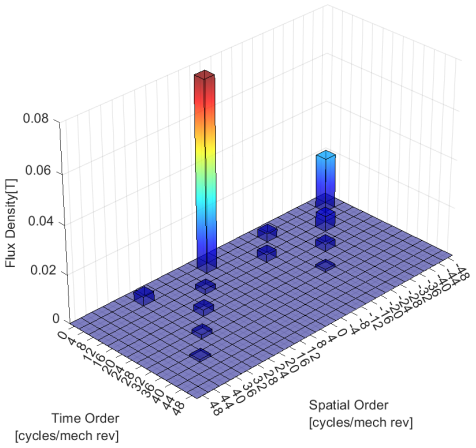

(f) Spatial and Temporal harmonics of B_t^{ARM} in 8p48s motor

Figure 5.6: Spatial and Temporal harmonics of flux density excited by Armature Reaction in slotless models

5.2 Flux density in slotted models

The influence of stator slotting on the air-gap flux density is examined in this section.

5.2.1 Flux density produced by PMs

Fig. 5.7 and Fig. 5.8 present the spatial and temporal distributions of the PM-generated air-gap flux density for the slotted and slotless models. As shown in Fig. 5.7, the presence of slots introduces a distinct spatial modulation: noticeable perturbations arise at each slot opening, leading to N_s fluctuations within one mechanical revolution. In contrast, Fig. 5.8 indicates that slotting does not alter the temporal evolution of the flux density waveform.

Fig. 5.9 provides the 2D–FFT spectra of the air-gap flux density for the two cases. In the slotless configuration, the PM-induced harmonics are primarily confined to the diagonal components. When slots are included, additional harmonic orders appear. These newly generated components are displaced from the original diagonal harmonics by integer multiples of kN_s in space, while their temporal frequencies remain unchanged.

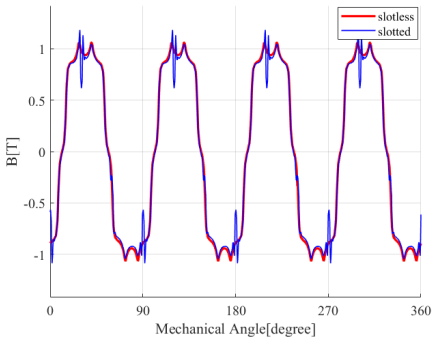

(a) B_r^{PM} vs. B_{sr}^{PM} in 8p12s motor

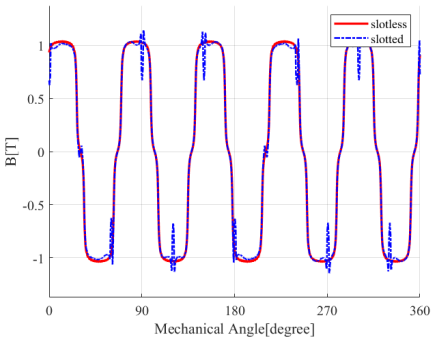

(b) B_r^{PM} vs. B_{sr}^{PM} in 10p12s motor

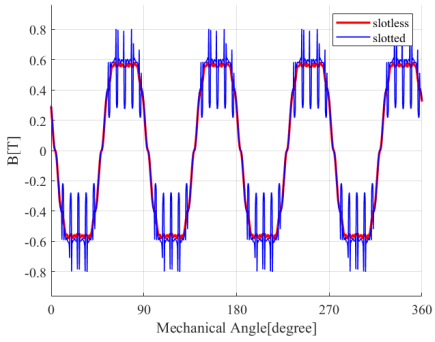

(c) B_r^{PM} vs. B_{sr}^{PM} in 8p48s motor

Figure 5.7: Spatial distributions of radial flux density by PM in slotless and slotted models

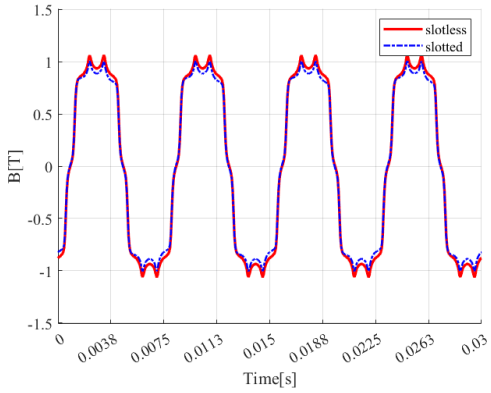

(a) B_r^{PM} vs. B_{sr}^{PM} in 8p12s motor

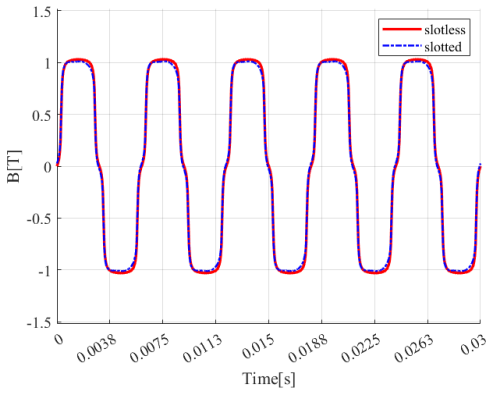

(b) B_r^{PM} vs. B_{sr}^{PM} in 10p12s motor

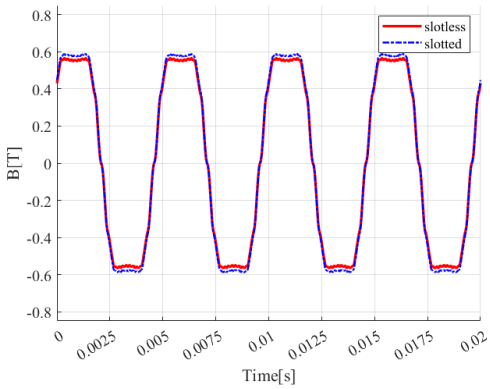

(c) B_r^{PM} vs. B_{sr}^{PM} in 8p48s motor

Figure 5.8: Temporal distributions of radial flux density by PM in slotless and slotted models

5.2.2 Flux density produced by Armature Reaction

The impact of stator slotting on the armature-reaction field is considerably more significant than its influence on the PM field. Fig. 5.10 illustrates the spatial distribution of the armature-reaction flux density with and without slots. After slotting is introduced, the air-gap field becomes significantly stronger. The flux density remains relatively uniform along each tooth surface, whereas sharp fluctuations occur near the interface between teeth tip and slots. The number of such fluctuations within one mechanical period corresponds to the stator tooth count N_s.

Fig. 5.11 compares the temporal waveforms of the armature-reaction field for the two configurations. In both cases, the air-gap flux density retains an approximately sinusoidal temporal profile, indicating that slotting does not affect its time-domain characteristics. However, the presence of slots results in a substantial increase in the amplitude. This occurs because, in the slotless machine, the high permeability of the stator core causes most of the armature flux to remain inside the core, whereas the introduction of slots forces a larger portion of the flux to pass through the air

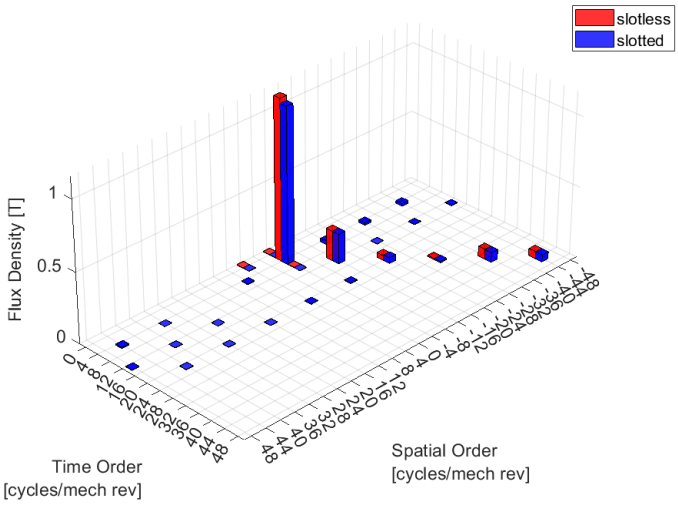

(a) B_r^{PM} vs. B_{sr}^{PM} in 8p12s motor

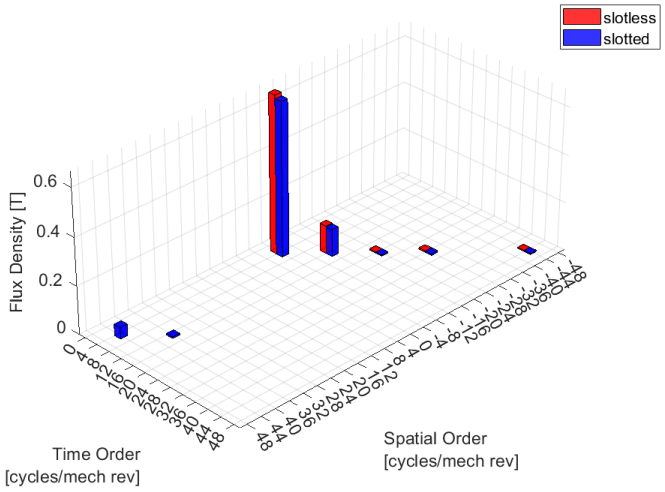

(b) B_r^{PM} vs. B_{sr}^{PM} in 8p48s motor

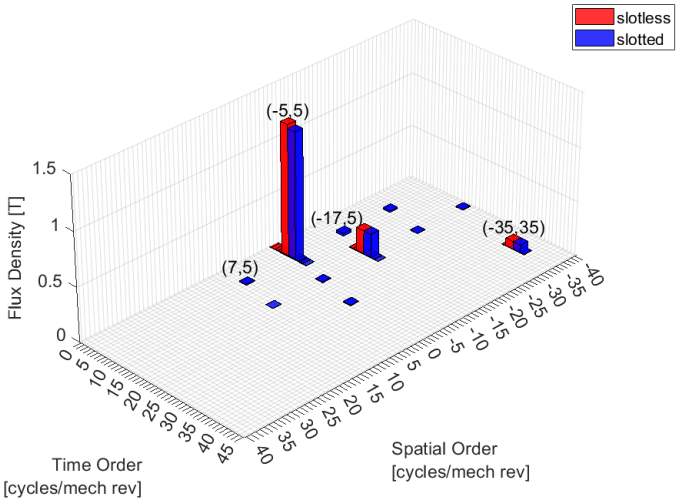

(c) B_r^{PM} vs. B_{sr}^{PM} in 10p12s motor

Figure 5.9: Spatial and Temporal distributions of radial flux density by PM in slotless and slotted models

gap.

The 2D-FFT spectra in Fig. 5.12 further quantify these effects. Although slotting does not generate new harmonic orders for the armature-reaction field, it significantly alters the magnitude distribution of existing harmonics. The spatial fundamental harmonic of the armature reaction (the fourth-order component in the 8p12s and 8p48s machines, and the fifth-order component in the 10p12s machine) is modulated by the stator teeth and redistributed into adjacent spatial orders. This modulation drastically changes the amplitude profile of the spatial harmonic spectrum, with several high-order components exhibiting substantial growth.

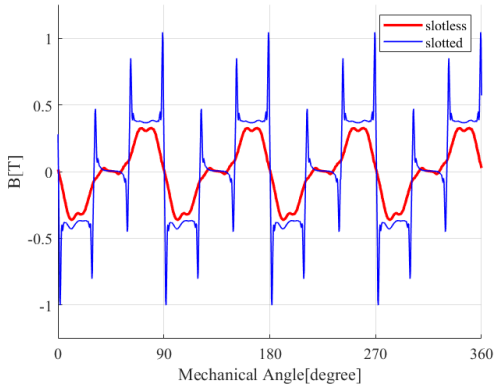

(a) B_r^{ARM} vs. B_{sr}^{ARM} in 8p12s motor

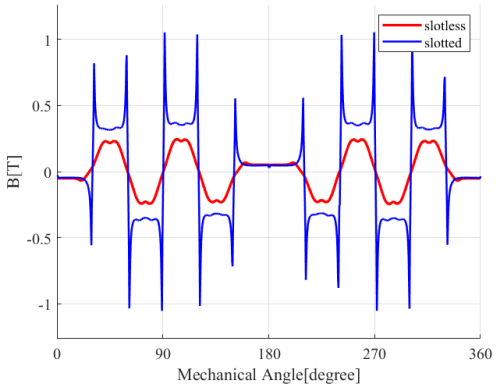

(b) B_r^{ARM} vs. B_{sr}^{ARM} in 10p12s motor

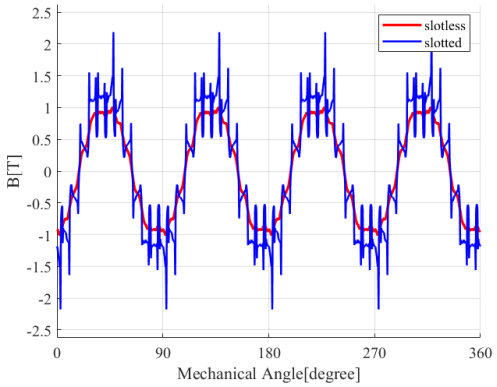

(c) B_r^{ARM} vs. B_{sr}^{ARM} in 8p48s motor

Figure 5.10: Spatial distributions of radial flux density by Armature Reactions in slotless and slotted models

In summary, the introduction of slotting modifies the spatial characteristics of the air-gap field. For the PM field, new harmonic orders are generated, whereas for the armature-reaction field, the magnitudes of existing harmonic orders are redistributed. Moreover, because more flux is compelled to enter the air gap, the overall flux-density level is increased.

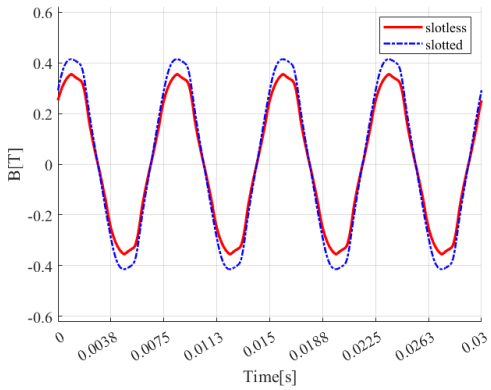

(a) B_r^{ARM} vs. B_{sr}^{ARM} in 8p12s motor

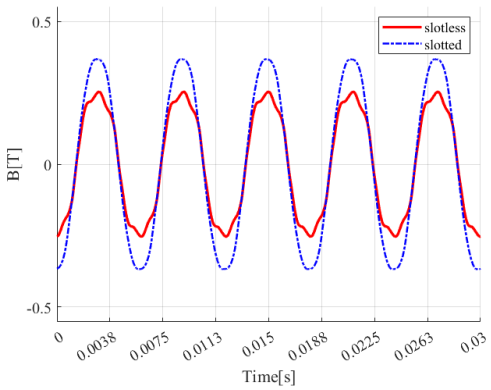

(b) B_r^{ARM} vs. B_{sr}^{ARM} in 10p12s motor

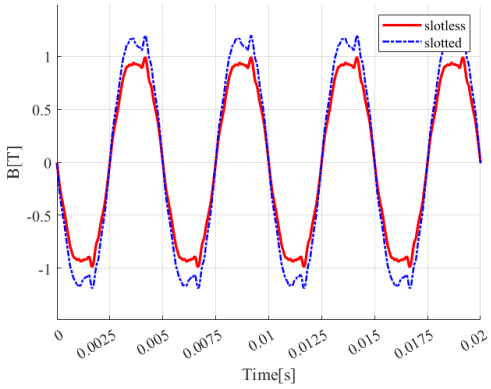

(c) B_r^{ARM} vs. B_{sr}^{ARM} in 8p48s motor

Figure 5.11: Temporal distributions of radial flux density by Armature Reactions in slotless and slotted models

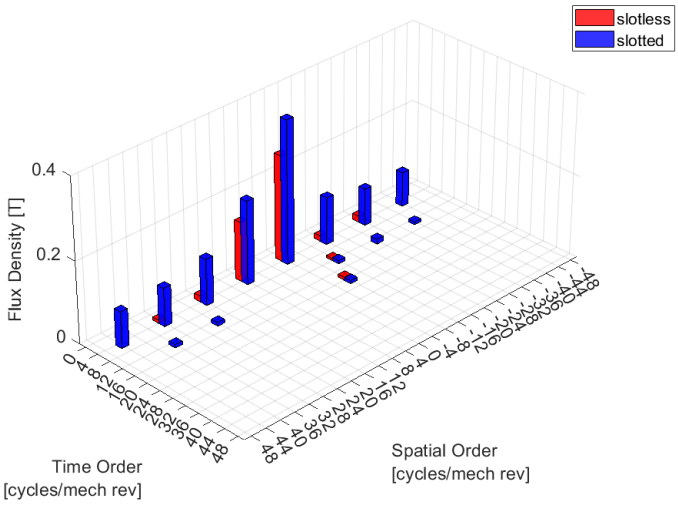

(a) B_r^{ARM} vs. B_{sr}^{ARM} in 8p12s motor

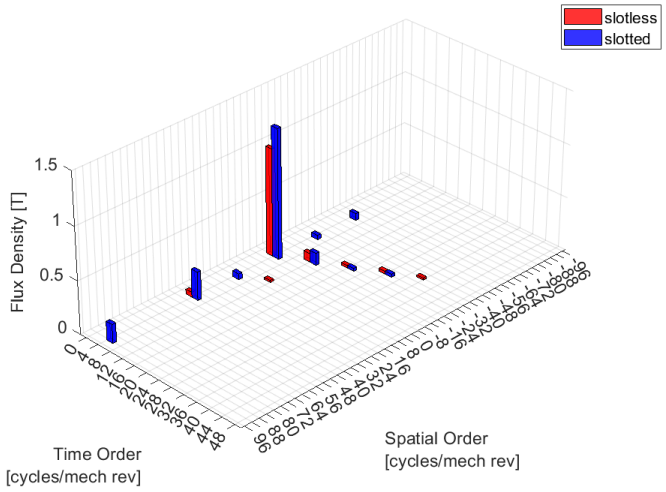

(b) B_r^{ARM} vs. B_{sr}^{ARM} in 8p48s motor

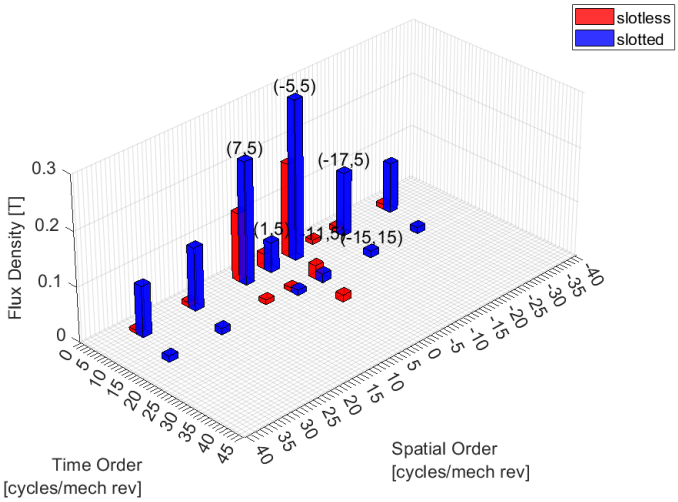

(c) B_r^{ARM} vs. B_{sr}^{ARM} in 10p12s motor

Figure 5.12: Spatial and Temporal distributions of radial flux density by Armature Reactions in slotless and slotted models

5.3 EM force densities in airgap

5.3.1 EM forces generated by interaction between PMs

Fig. 5.13 illustrates the spatiotemporal distribution of the radial EM force waves produced by the no-load magnetic field in the slotted model. As shown, these force waves exhibit clear periodicity in both space and time.

A two-dimensional FFT analysis of the no-load force waves is presented in Fig. 5.14. The radial and tangential components share the same spatiotemporal harmonic orders, differing only in magnitude. For the radial component, the dominant harmonics lie along the diagonal, corresponding to the order $(2kp, 2kp)$. These components originate from the slotless air-gap flux density and are solely excited by the rotor permanent magnets, independent of the stator slotting effect. Additional components influenced by stator-tooth modulation also appear, characterized by the order $(2kp + iNs, 2kp)$. For all three machines, the minimum nonzero spatial order of the electromagnetic force waves is determined by GCD$(2p, Ns)$. This result is consistent with the analytical model introduced in Chapter 2.

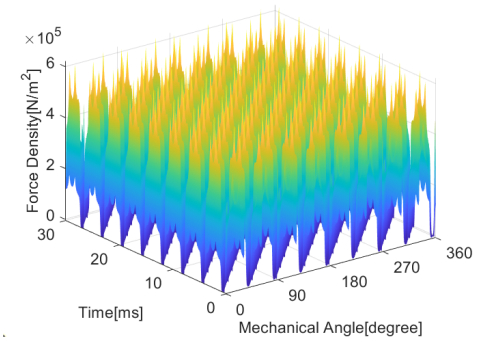

(a) Distribution of $p_{sr}^{\mathrm{PM\times PM}}$ wave in 8p12s motor

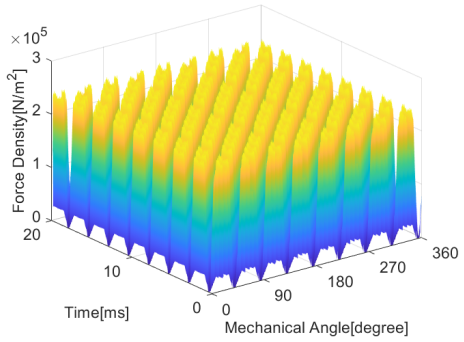

(b) Distribution of $p_{sr}^{\mathrm{PM\times PM}}$ wave in 8p48s motor

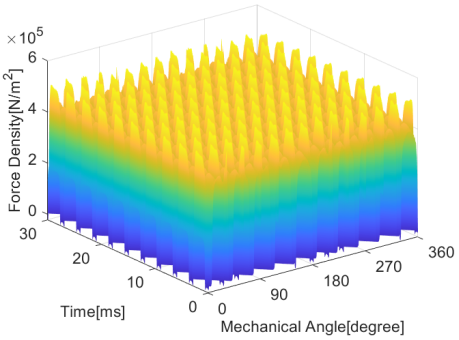

(c) Distribution of $p_{sr}^{\mathrm{PM\times PM}}$ wave in 10p12s motor

Figure 5.13: Distributions of radial force density waves generated by the interaction between PMs in slotted models

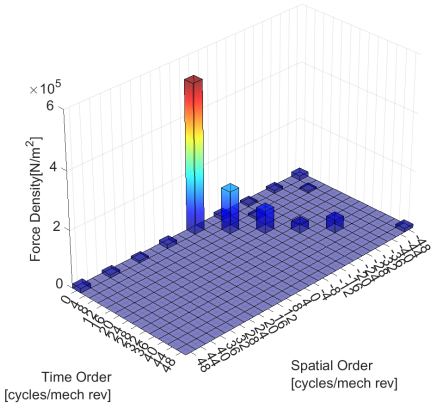

(a) Spatial and Temporal harmonics of $p_{sr}^{\mathrm{PM\times PM}}$ in 8p12s motor

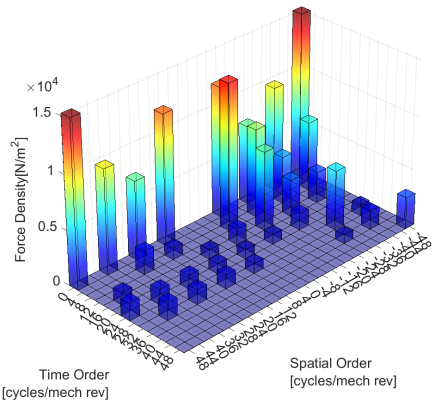

(b) Spatial and Temporal harmonics of $p_{st}^{\mathrm{PM\times PM}}$ in 8p12s motor

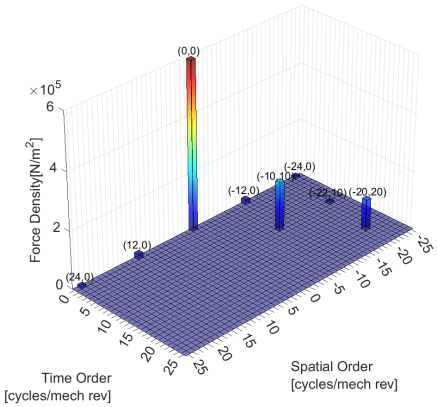

(c) Spatial and Temporal harmonics of $p_{sr}^{\mathrm{PM\times PM}}$ in 10p12s motor

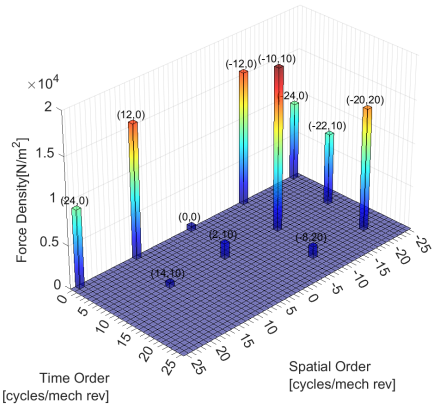

(d) Spatial and Temporal harmonics of $p_{st}^{\mathrm{PM\times PM}}$ in 10p12s motor

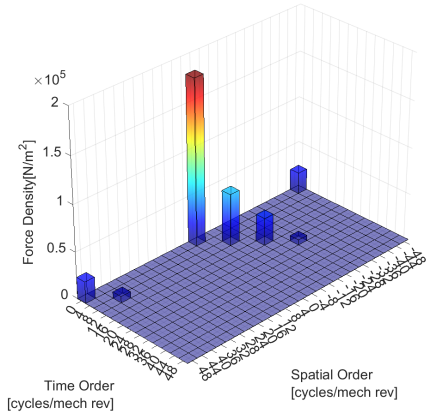

(e) Spatial and Temporal harmonics of $p_{sr}^{\mathrm{PM\times PM}}$ in 8p48s motor

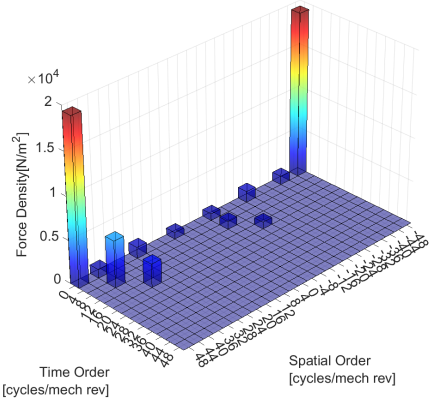

(f) Spatial and Temporal harmonics of $p_{st}^{\mathrm{PM\times PM}}$ in 8p48s motor

Figure 5.14: Spatial and Temporal harmonics of force density generated by the interaction between PMs in slotted motors

5.3.2 EM forces generated by interaction between Armature reactions

Fig. 5.15 presents the distribution of the radial electromagnetic force waves generated by the armature-reaction field in the slotted model. As illustrated, these force waves exhibit periodic behavior in both space and time.

The 2D-FFT results of the armature-reaction force waves are shown in Fig. 5.16. For all three machines, the temporal orders of the force harmonics are concentrated at 0 and $2p$. A few additional components appear around kp due to core saturation, but their magnitudes are sufficiently small to be neglected. In contrast, the spatial distributions differ significantly among the three machines. In the absence of slotting, the spatial orders associated with harmonics of the same temporal order differ by $3kp$, $6k$, and $6kp$ for the three machines, respectively. When slotting is included, no new spatial orders are introduced, although their amplitudes are modified. The lowest nonzero spatial order of the air-gap electromagnetic forces remains $\mathrm{GCD}(2p, Ns)$ for all machines, which is consistent with the analytical model.

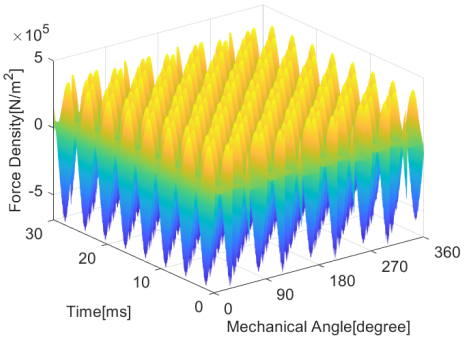

(a) Distribution of $p_{sr}^{\mathrm{ARM}\times\mathrm{ARM}}$ wave in 8p12s motor

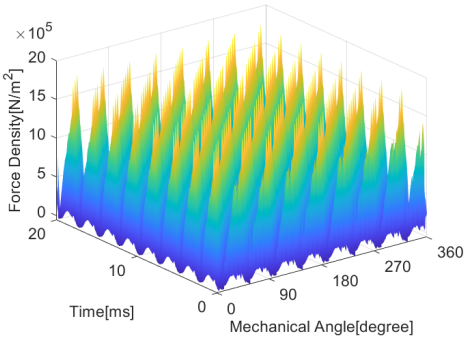

(b) Distribution of $p_{sr}^{\mathrm{ARM}\times\mathrm{ARM}}$ wave in 8p48s motor

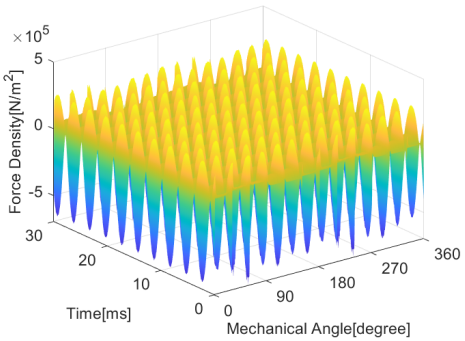

(c) Distribution of $p_{sr}^{\mathrm{ARM}\times\mathrm{ARM}}$ wave in 10p12s motor

Figure 5.15: Distributions of radial force density waves generated by the interaction between Armature Reactions in slotted models

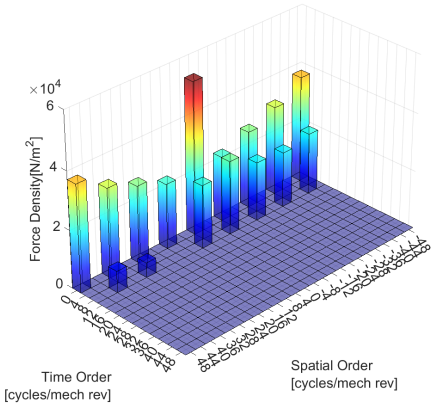

(a) Spatial and Temporal harmonics of $p_{sr}^{\mathrm{ARM}\times\mathrm{ARM}}$ in 8p12s motor

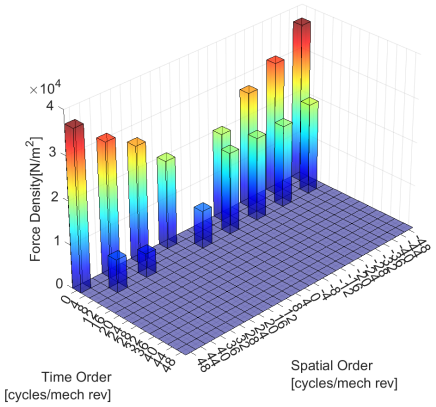

(b) Spatial and Temporal harmonics of $p_{st}^{\mathrm{ARM}\times\mathrm{ARM}}$ in 8p12s motor

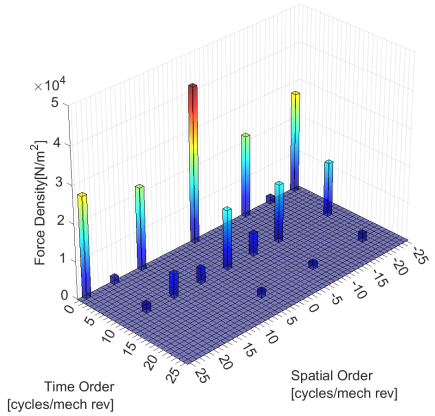

(c) Spatial and Temporal harmonics of $p_{sr}^{\mathrm{ARM}\times\mathrm{ARM}}$ in 10p12s motor

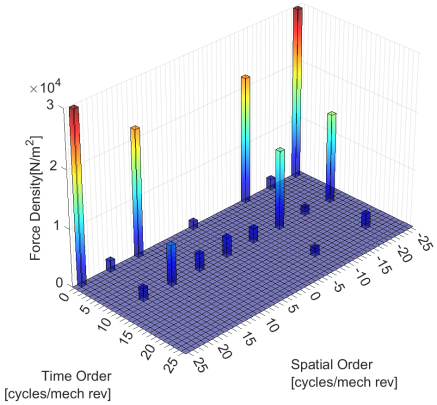

(d) Spatial and Temporal harmonics of $p_{st}^{\mathrm{ARM}\times\mathrm{ARM}}$ in 10p12s motor

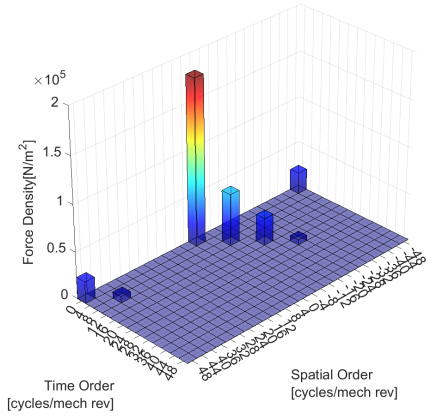

(e) Spatial and Temporal harmonics of $p_{sr}^{\mathrm{ARM}\times\mathrm{ARM}}$ in 8p48s motor

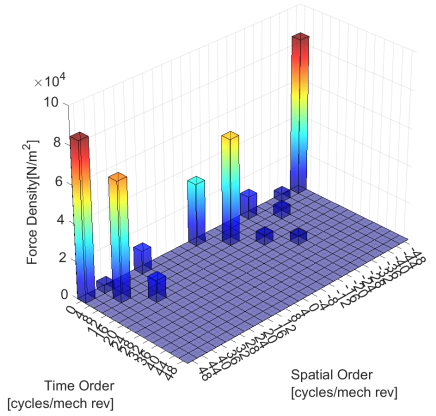

(f) Spatial and Temporal harmonics of $p_{st}^{\mathrm{ARM}\times\mathrm{ARM}}$ in 8p48s motor

Figure 5.16: Spatial and Temporal harmonics of force density generated by the interaction between Armature Reactions in slotted motors

5.3.3 Total EM forces under full load

Fig. 5.17 illustrates the spatiotemporal distribution of the radial electromagnetic force waves under load in the slotted model. As observed, the force waves exhibit periodicity in both space and time.

The corresponding 2D-FFT results are shown in Fig. 5.18. Among the radial force components of the three machines, the dominant contributions appear along the diagonal at the harmonic order $(2kp, 2kp)$. In the absence of slotting, these components mainly arise from arbitrary-order air-gap flux density harmonics generated by the PM and the fundamental air-gap flux produced by the armature reaction. Additional significant components occur at temporal orders 0 and $2p$, which are primarily attributed to the coupling between low-order PM harmonics and arbitrary armature harmonics. Introducing stator slots does not alter the temporal or spatial harmonic orders, although it may influence their amplitudes by shifting high magnitude lower components to higher ones by slot-number orders, i.e, $(12, 0)$ in 8p12s, $(12, 0)$ in 10p12s, and $(48, 0)$ in 8p48s. All prominent harmonics satisfy this condition: they must originate from low-order PM flux components, low-order armature flux components, or low-order slotting harmonics.

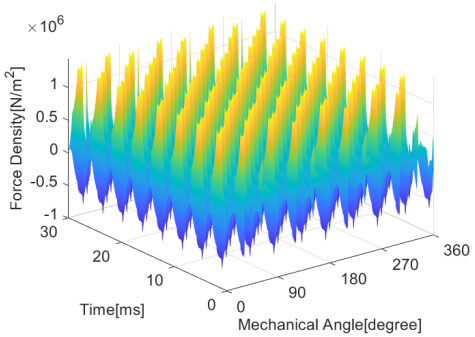

(a) Distribution of p_{sr} wave in 8p12s motor

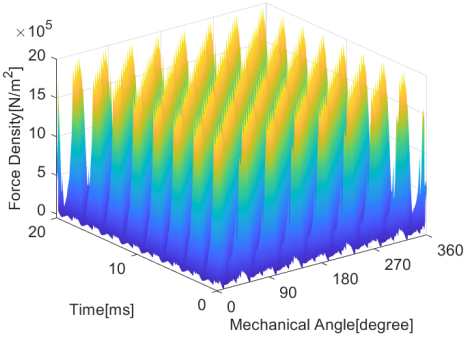

(b) Distribution of p_{sr} wave in 8p48s motor

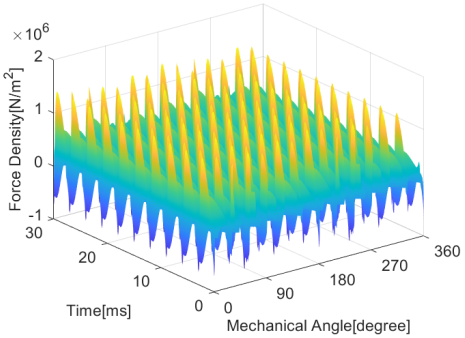

(c) Distribution of p_{sr} wave in 10p12s motor

Figure 5.17: Distributions of total radial force density waves in slotted models

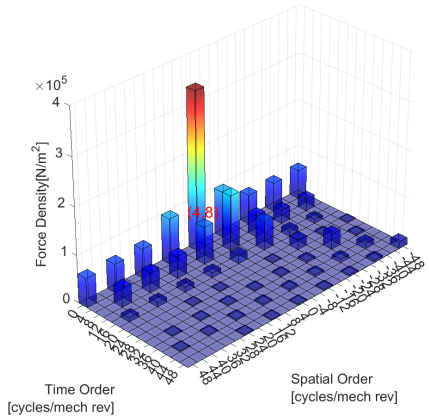

(a) Spatial and Temporal harmonics of p_{sr} in 8p12s motor

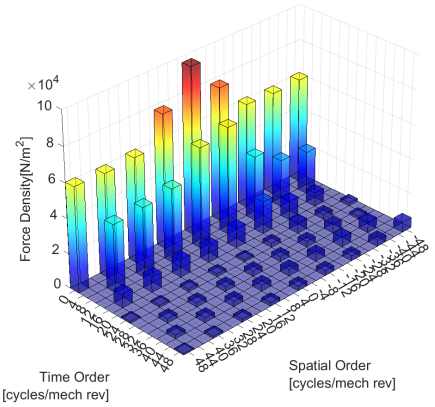

(b) Spatial and Temporal harmonics of p_{st} in 8p12s motor

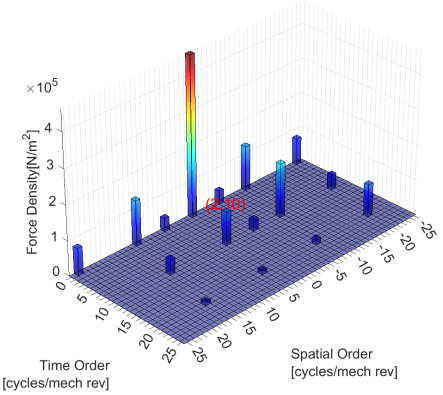

(c) Spatial and Temporal harmonics of p_{sr} in 10p12s motor

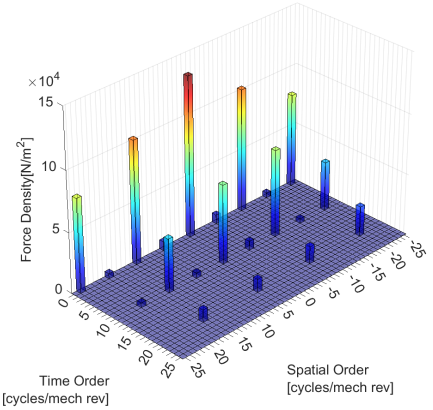

(d) Spatial and Temporal harmonics of p_{st} in 10p12s motor

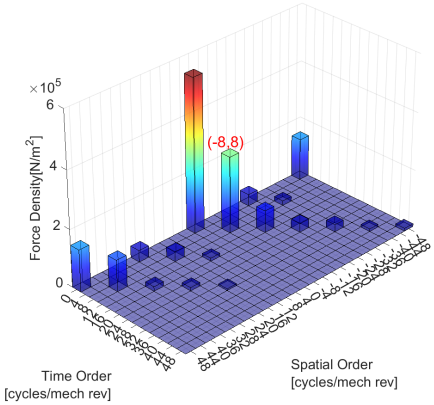

(e) Spatial and Temporal harmonics of p_{sr} in 8p48s motor

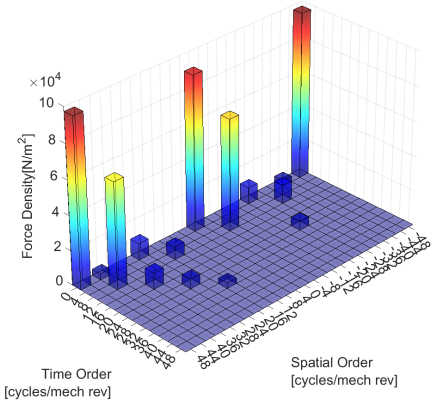

(f) Spatial and Temporal harmonics of p_{st} in 8p48s motor

Figure 5.18: Spatial and Temporal harmonics of total force density in slotted motors

5.3.4 Summary of air-gap EM force distribution

In summary, the following conclusions can be drawn regarding the overall distribution characteristics of the total air-gap electromagnetic forces.

As for the spatiotemporal distribution, for all three machines, the temporal order of the air-gap electromagnetic forces is $2kp$, while the spatial orders differ but can all be expressed as integer multiples of GCD$(2p, N_s)$. The smallest nonzero spatial order remains GCD$(2p, N_s)$, which is consistent with the analytical model. More specifically, the smallest nonzero spatial orders of the three machines are 4, 2, and 8, corresponding respectively to the 8p12s, 10p12s, and 8p48s machines. Tangential and radial components share the same order.

As for the amplitude distribution, it can be observed that the dominant components of the radial electromagnetic force are mainly concentrated along the diagonal of the spectrum . These components are primarily composed of PM flux density harmonics and fundamental components of the armature reaction flux density. In FSCW-machines, low spatial-order EM force wave components formed by the interaction between the PM flux and low-order armature-reaction flux harmonics also exhibit relatively high amplitudes. Moreover, all harmonics may be further modulated by the fundamental component associated with the stator teeth. Recognizing these characteristics provide an important basis for the subsequent analysis of mechanical tooth modulation.

5.4 Torque analysis

5.4.1 Constant torque and torque ripple

Fig. 5.19 presents the torque waveforms obtained from the FEM simulations for the different electromagnetic force components. Performing an FFT on these torque waveforms yields the spectra shown in Fig. 5.20. As illustrated, under no-load conditions, the electromagnetic force generated solely by the PMs in both machines does not contribute to the constant torque component but instead produces exclusively torque ripple, commonly referred to as cogging torque. In contrast, the force component originating solely from the armature windings generates not only torque ripple but also a constant torque component, which corresponds to the reluctance torque.

It is evident that the reluctance torque of the 8p48s machine is significantly larger than that of the 8p12s machine. This is attributed to the fact that the 8p48s machine adopted here is an IPM topology, whereas the 8p12s machine is an SPM design. The IPM rotor exhibits more pronounced saliency, enabling it to generate a higher reluctance torque. Finally, comparing the above torque components with the total torque indicates that the interaction between the PM and armature fields is the dominant contributor to the constant torque output.

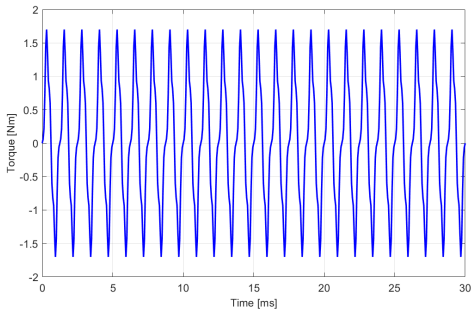

(a) No-load torque $T^{\mathrm{PM}\times\mathrm{PM}}$ in 8p12s motor

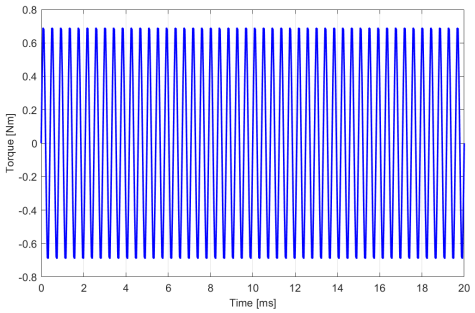

(b) No-load torque $T^{\mathrm{PM}\times\mathrm{PM}}$ in 8p48s motor

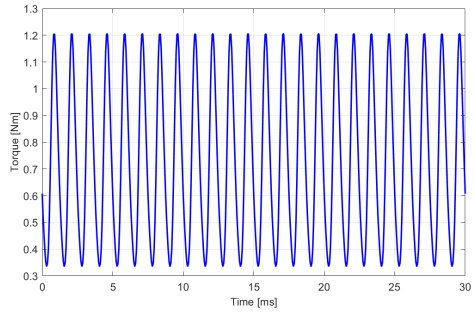

(c) Reluctance torque $T^{\mathrm{ARM}\times\mathrm{ARM}}$ in 8p12s motor

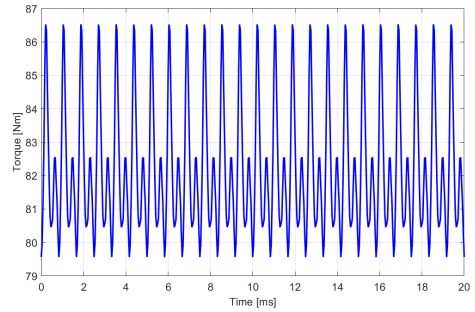

(d) Reluctance torque $T^{\mathrm{ARM}\times\mathrm{ARM}}$ in 8p48s motor

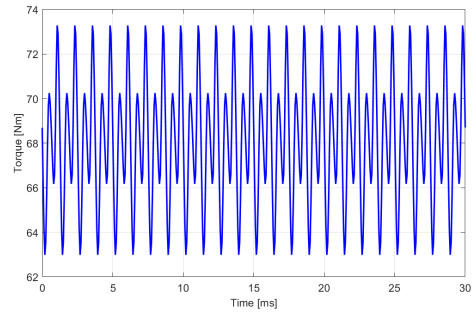

(e) Total torque in 8p12s motor

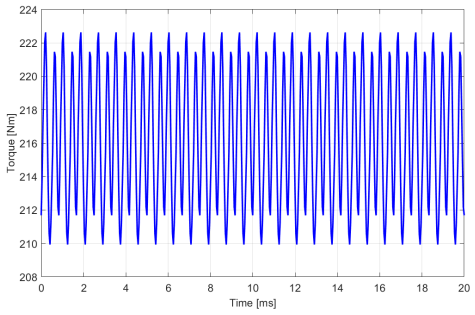

(f) Total torque in 8p48s motor

Figure 5.19: Torque waveforms from different sources in 8p12s and 8p48s motors.

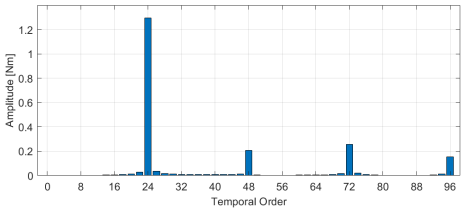

(a) FFT of no-load torque $T^{\mathrm{PM}\times\mathrm{PM}}$ in 8p12s motor

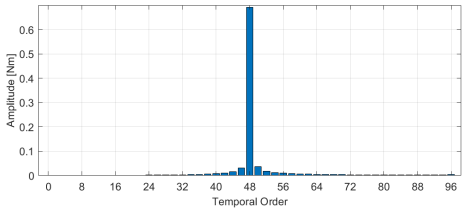

(b) FFT of no-load torque $T^{\mathrm{PM}\times\mathrm{PM}}$ in 8p48s motor

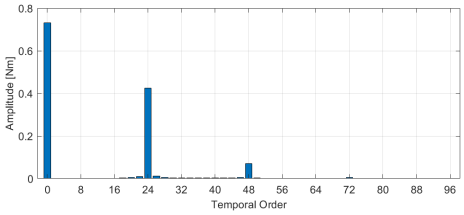

(c) FFT of reluctance torque $T^{\mathrm{ARM}\times\mathrm{ARM}}$ in 8p12s motor

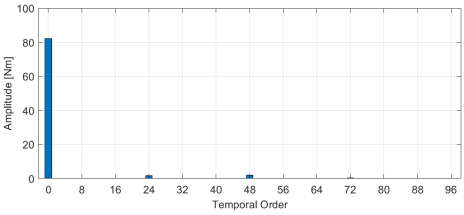

(d) FFT of reluctance torque $T^{\mathrm{ARM}\times\mathrm{ARM}}$ in 8p48s motor

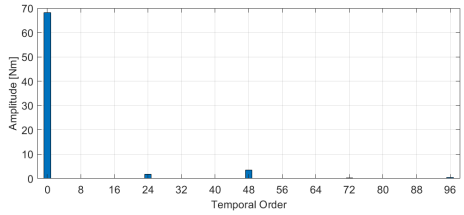

(e) FFT of total torque in 8p12s motor

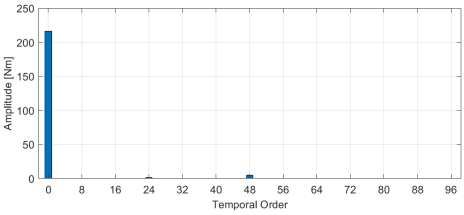

(f) FFT of total torque in 8p48s motor

Figure 5.20: FFT of torque components from different sources in 8p12s and 8p48s motors.

5.4.2 Cogging torque under no-load conditions

Fig. 5.21 compares the cogging torque waveforms of the slotted and slotless models for the three machines, while Fig. 5.22 presents the corresponding FFT spectra. It is evident that the slotless models generate virtually no torque ripple, indicating that cogging torque arises only in the presence of stator slotting. This result is fully consistent with the analytical findings discussed in Chapter 3.

Furthermore, the temporal orders of the cogging torque for the three machines are integer multiples of 24, 48, and 60, respectively, corresponding to LMC($2p, N_s$). This observation agrees with the analytical predictions in Chapter 3.

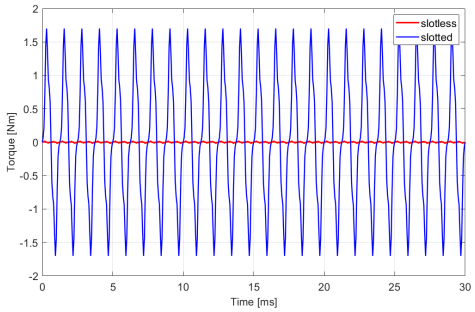

(a) Cogging torque in 8p12s motor

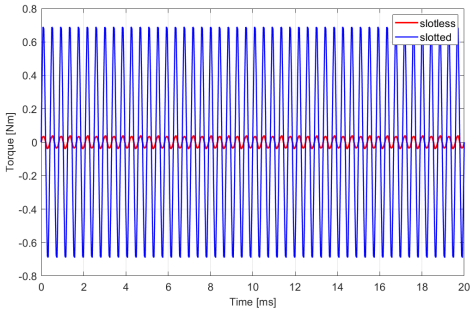

(b) Cogging torque in 8p48s motor

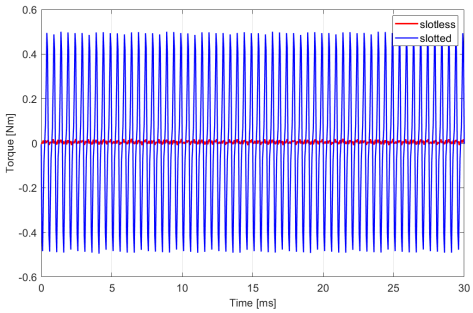

(c) Cogging torque in 10p12s motor

Figure 5.21: Cogging torques in slotless and slotted model

5.4.3 Torque ripple under load

Fig. 5.23 compares the FFT spectra of torque ripple components caused by different sources of electromagnetic forces under load conditions for the three machines. For all three machines, the torque ripple components associated with the armature-reaction-related electromagnetic forces (including $T^{\mathrm{ARM\times ARM}}$ and $T^{\mathrm{PM\times ARM}}$) appear at multiples of 24, 24, and 30, respectively, corresponding to the $6kp$ harmonic order. This observation is consistent with the conclusions presented in Chapter 3.

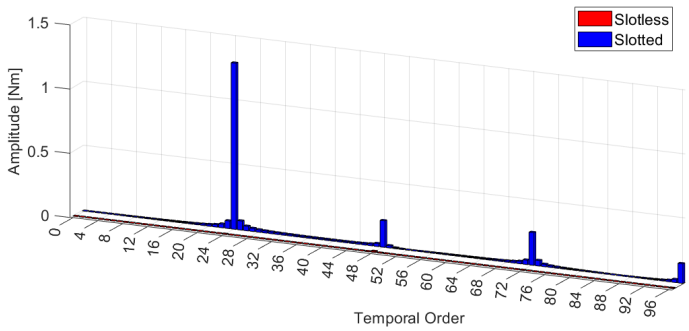

(a) FFT of Cogging torque in 8p12s motor

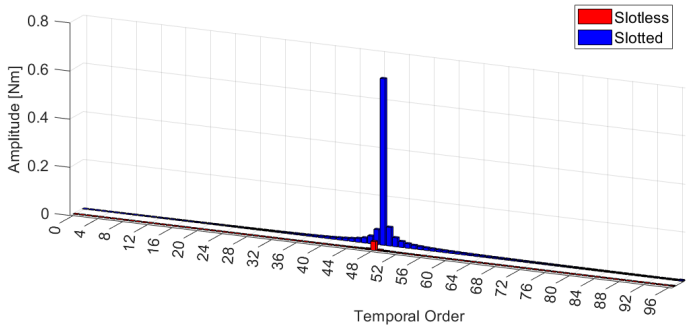

(b) FFT of Cogging torque in 8p48s motor

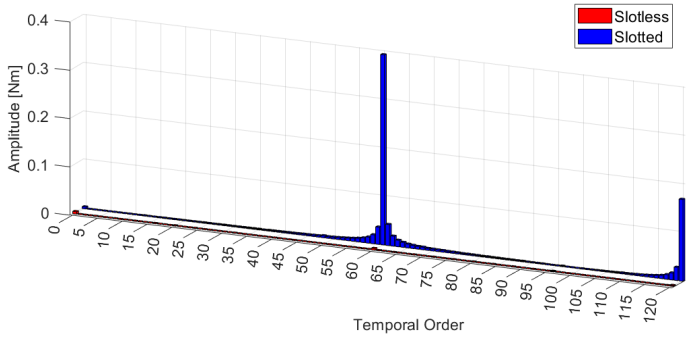

(c) FFT of Cogging torque in 10p12s motor

Figure 5.22: FFT of Cogging torques in slotless and slotted model

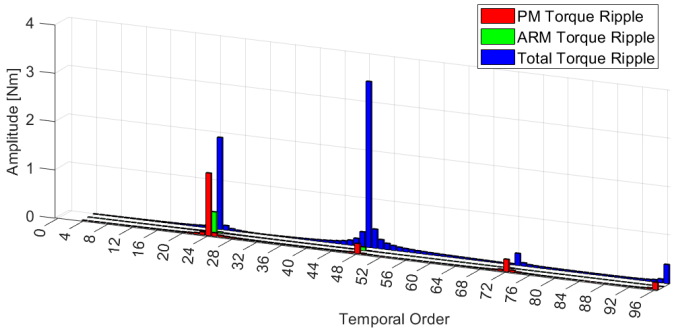

(a) FFT of torque ripples in 8p12s motor

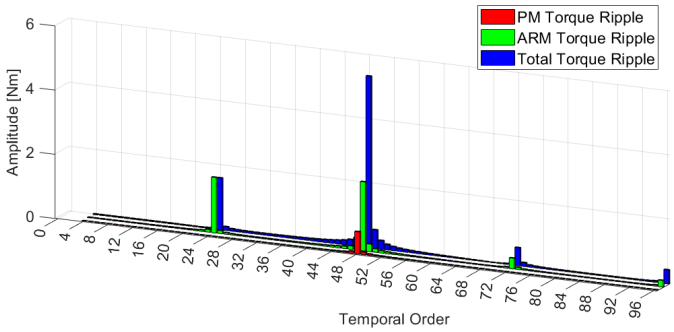

(b) FFT of torque ripples in 8p48s motor

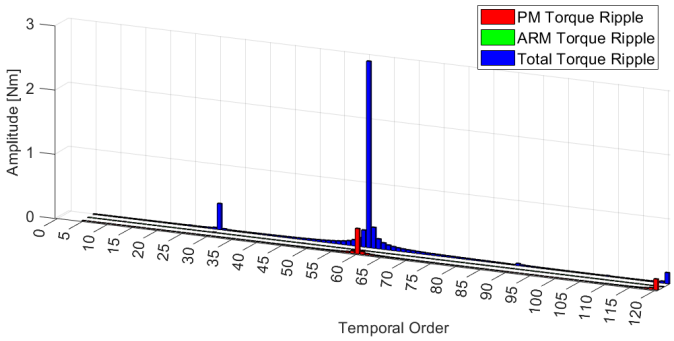

(c) FFT of torque ripples in 10p12s motor

Figure 5.23: FFT comparison of torque ripples originating from different electromagnetic sources in the three machines under load condition.

5.5 Analysis of tooth mechanical modulation

In the following, the mechanical modulation effect of the stator teeth during the transmission process from the air-gap electromagnetic forces to the stator tooth forces in different machines is investigated.

5.5.1 Absolute v.s. Normalized relative Amplitude

Fig. 5.24, Fig. 5.26 and Fig. 5.28 compare, for the three machines considered in this study, the air-gap electromagnetic force density, the distributed stator tooth force density after mechanical modulation by the stator teeth, and the force density corresponding to the tooth-concentrated forces obtained through spatial sampling by the stator teeth.

Fig. 5.24(a),Fig. 5.26(a) and Fig. 5.28(a) present the absolute values of the force densities, which directly illustrate the variations in the amplitudes of the force density components at different harmonic orders before and after the modulation and sampling processes. Fig. 5.24(b), Fig. 5.26(b) and Fig. 5.28(b) show the normalized force density spectra. The normalization is performed independently for each force spectrum, including the air-gap force, the tooth-modulated force, and the tooth-sampled force. Specifically, for a given force spectrum, the force density at each harmonic order is normalized by the maximum value within the same spectrum.

This normalization procedure eliminates the influence of the overall amplitude scaling introduced by the mechanical modulation and spatial sampling processes, thereby shifting the focus of the analysis from absolute magnitudes to the relative distribution of harmonic components. As a result, the relative significance of the same harmonic order within the overall harmonic structure can be meaningfully compared among different stages of force transmission.

Fig. 5.25, Fig. 5.27, and Fig. 5.29 illustrate, for the three machines, the variation of the amplitude ratios of the force densities of the tooth-concentrated forces and the distributed stator tooth forces to that of the original air-gap electromagnetic force density, for several pronounced low-order harmonic components that are likely to induce vibration, as a function of the embrace. Comparisons are performed for both the absolute force density amplitudes and the normalized force density amplitudes. In addition, the corresponding ratio values at the embrace of the machines investigated in this study are also marked.

5.5.2 Common Characteristics

By comparing Figs. 5.24–5.29, several common characteristics can be identified.

As shown in Figs. 5.24, 5.26, and 5.27, the mechanical modulation introduced by the stator teeth alters the amplitude distribution of the force density spectrum across

different harmonic orders. Under the modulation effect, the resulting distributed stator tooth forces do not introduce new spectral components; however, both the absolute amplitudes and the normalized relative amplitudes of the force density components at each harmonic order are modified.

Under the sampling effect, the tooth-concentrated forces exhibit aliasing, and the resulting force density spectrum contains only spatial harmonic components with orders lower than $N_s/2$.

From Figs. 5.25, 5.27, and 5.29, it can be observed that, in general, the sampling effect associated with the tooth-concentrated forces amplifies low-order spatial harmonic components more strongly than the modulation effect associated with the distributed stator tooth forces.

Moreover, when comparing the variations of the amplitude ratios before and after mechanical modulation, the ratios based on the normalized relative amplitudes at the same harmonic order are generally higher than those based on the absolute amplitudes. This indicates that, although mechanical modulation may reduce the total air-gap force density acting on the stator teeth, resulting in little change or even a decrease in the absolute amplitudes of certain low-order harmonics, their relative contributions within the overall harmonic spectrum are nevertheless increased.

The mechanical modulation effects in different machines are analyzed in detail in the following.

5.5.3 Tooth mechanical modulation of 8p12s

For the 8p12s machine, it can be observed from Fig. 5.24 that the harmonic components (−4, 8), (4, 16), and (0, 48) are among the most pronounced low-order components in the force density spectrum.

By further examining Fig. 5.25(a) and Fig. 5.25(c), it is found that the absolute amplitudes of the (−4, 8) and (4, 16) components after mechanical modulation vary with the embrace over a single period, whereas the (0, 48) component varies over four periods with respect to the embrace. This indicates that the mechanically modulated (−4, 8) and (4, 16) components are mainly generated by the original air-gap components (−4, 8) and (4, 16), together with the diagonal air-gap components (8, 8) and (16, 16), through modulation by the first harmonic of the tooth modulation function, which varies over one period. In contrast, the (0, 48) component is produced by the original air-gap (0, 48) component and the diagonal air-gap component (48, 48) through modulation by the fourth harmonic of the tooth modulation function, which varies over four periods.

Since the (−4, 8) and (4, 16) components already exist as relatively strong harmonics in the original air-gap spectrum and the embrace of this machine is 0.93 which close to 1, the modulation effect associated with the first harmonic of the tooth modulation function is weak. As a result, the variations of these components before and after

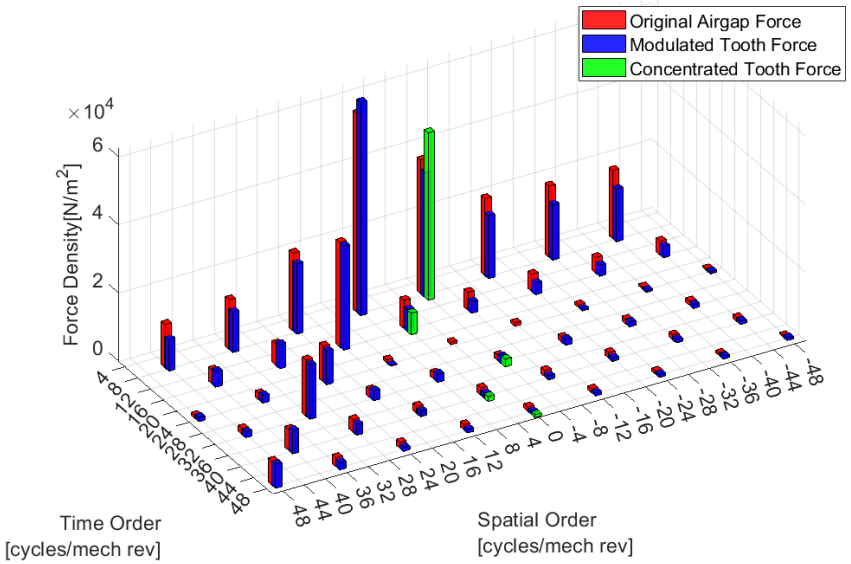

(a) Harmonic components in 8p12s motor

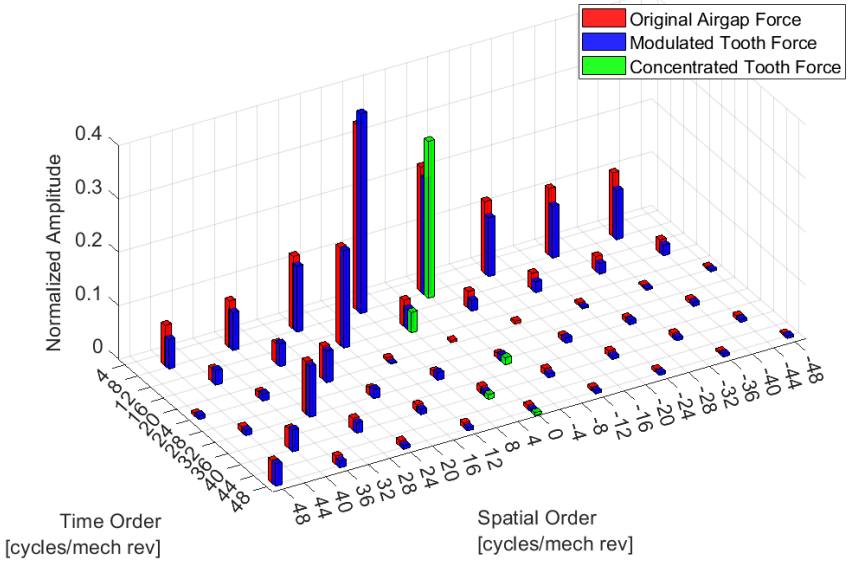

(b) Normalized harmonic components in 8p12s motor

Figure 5.24: Comparison of Spatial and Temporal harmonics of air-gap and tooth force density in 8p12s motor@embrace=0.93

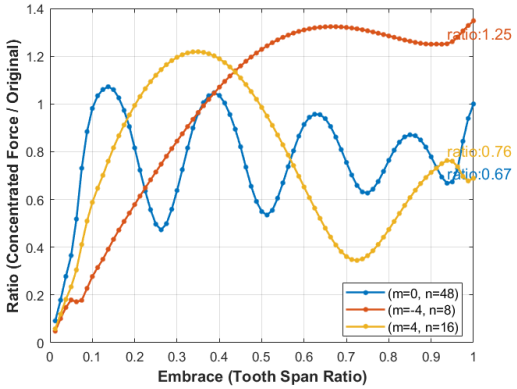

(a) Ratio between Concentrated and Original force varying with embrace in 8p12s motor

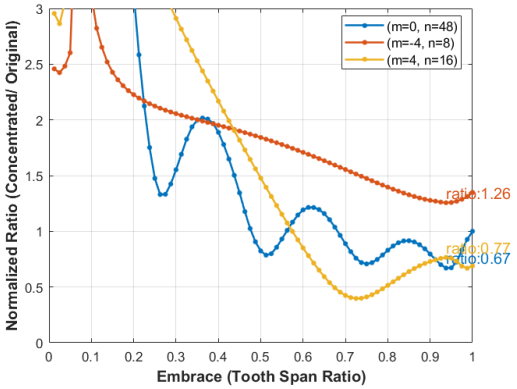

(b) Ratio between Normalized Concentrated and Original force varying with embrace in 8p12s motor

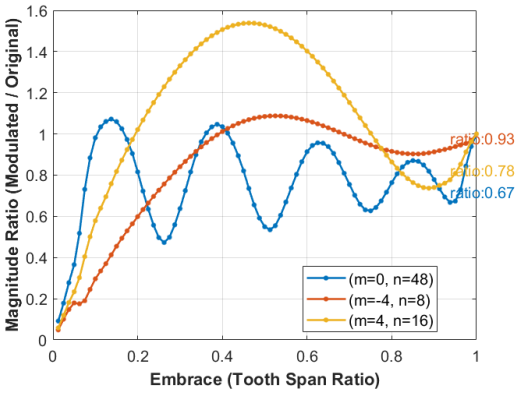

(c) Ratio between Modulated and Original force varying with embrace in 8p12s motor

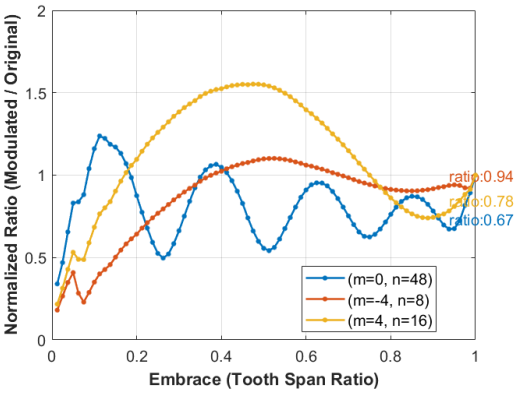

(d) Ratio between Normalized Modulated and Original force varying with embrace in 8p12s motor

Figure 5.25: Ratio between tooth force and air-gap force for key harmonic components varying with tooth embrace in 8p12s motor

modulation are not significant. Although the (0, 48) component is not a pronounced harmonic in the original air-gap spectrum, however, its newly generated contribution is modulated by the fourth harmonic of the tooth modulation function, and owing to the embrace being close to 1, the resulting variation remains small.

By further examining Fig. 5.25(b) and Fig. 5.25(d), it can be observed that, due to the aliasing effect associated with the tooth-concentrated forces, a larger portion of the spectral content is shifted toward lower spatial orders. Consequently, the normalized relative amplitudes of the low-order components of the tooth-concentrated forces are generally higher than those of the distributed stator tooth forces.

5.5.4 Tooth mechanical modulation of 10p12s

For the 10p12s machine, it can be observed from Fig. 5.26 that the harmonic components (−2, 10) and (−4, 20) are among the most pronounced low-order components in the force density spectrum.

By further examining Fig. 5.27(a) and Fig. 5.27(c), it is found that the absolute amplitude of the (−2, 10) component after mechanical modulation varies with the embrace over a single period, whereas the (−4, 20) component varies over two periods. This indicates that the mechanically modulated (−2, 10) component is mainly generated by the original air-gap (−2, 10) component together with the diagonal air-gap component (10, 10) through modulation by the first harmonic of the tooth modulation function, which varies over one period. In contrast, the (−4, 20) component is generated by the original air-gap (−4, 20) component together with the diagonal air-gap component (20, 20) through modulation by the second harmonic of the tooth modulation function, which varies over two periods.

Since the (−2, 10) component already exists as a relatively strong harmonic in the original air-gap spectrum and the embrace of this machine is close to 1, the modulation effect associated with the first harmonic of the tooth modulation function is weak, and therefore the variation before and after modulation is not significant. The (−4, 20) component, however, is not a pronounced harmonic in the original air-gap spectrum; consequently, its sampling effect in the tooth-concentrated forces is more evident and leads to an amplification of approximately 1.7 times. Nevertheless, its newly generated contribution in the distributed stator tooth forces is modulated by the second harmonic of the tooth modulation function, and owing to the embrace being close to 1, the modulation effect remains weak. In addition, since the spatial order of the (−4, 20) component is four, the vibration that it can practically induce is still smaller than that associated with second-order spatial harmonics.

By further examining Fig. 5.27(b) and Fig. 5.27(d), it can likewise be observed that, due to the aliasing effect associated with the tooth-concentrated forces, a larger portion of the spectral content is shifted toward lower spatial orders. Consequently, the normalized relative amplitudes of the low-order components of the tooth-concentrated forces are higher than those of the distributed stator tooth forces.

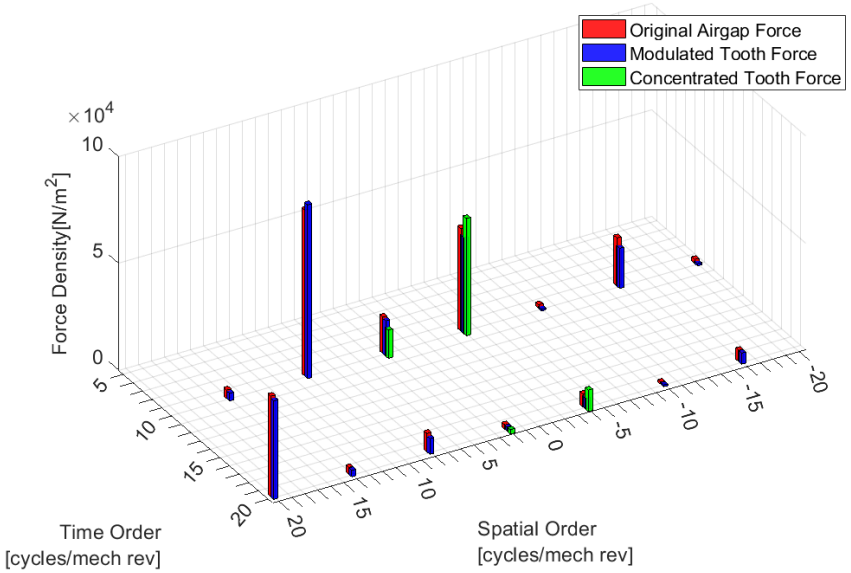

(a) Harmonic components in 10p12s motor

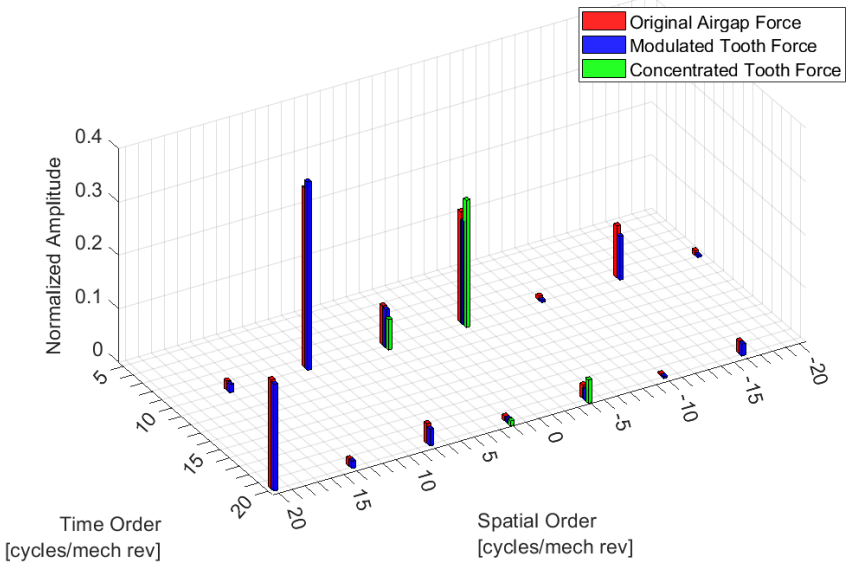

(b) Normalized harmonic components in 10p12s motor

Figure 5.26: Spatial and Temporal harmonics of air-gap and tooth force density in 10p12s motor@embrace=0.93

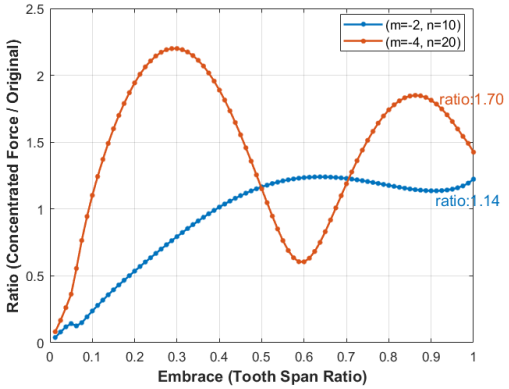

(a) Ratio between Concentrated and Original force varying with embrace in 10p12s motor

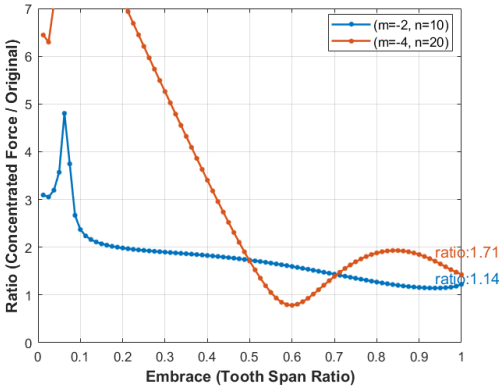

(b) Ratio between Normalized Concentrated and Original force varying with embrace in 10p12s motor

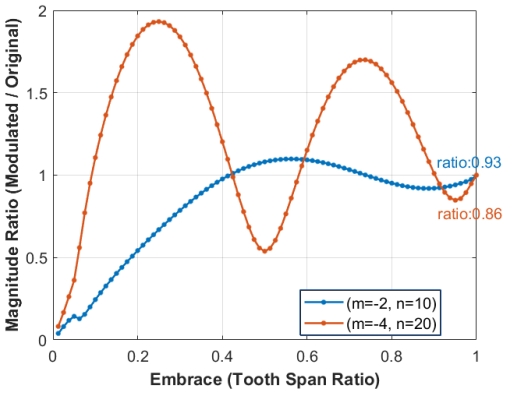

(c) Ratio between Modulated and Original force varying with embrace in 10p12s motor

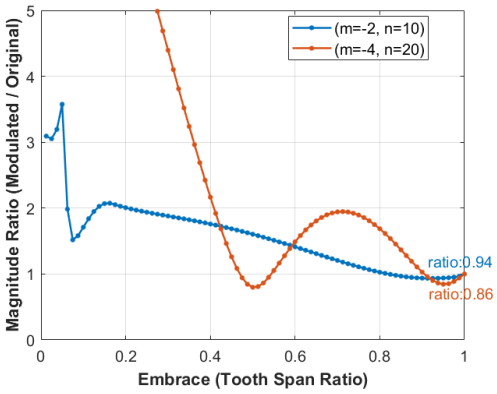

(d) Ratio between Normalized Modulated and Original force varying with embrace in 10p12s motor

Figure 5.27: Ratio between tooth and air-gap force varying with tooth embrace in 10p12s motor

Overall, mechanical modulation increases the relative amplitudes of low-order harmonics. However, since the embrace of this machine is close to 1, the variations in the relative amplitudes remain limited.

5.5.5 Tooth mechanical modulation of 8p48s

For the 8p48s machine, it can be observed from Fig. 5.28 that the harmonic components (0, 48) and (8, 8) are among the most pronounced low-order components in the force density spectrum.

By further examining Fig. 5.29(a) and Fig. 5.29(c), it is found that the absolute amplitudes of the (0, 48) and (−8, 8) components after mechanical modulation both vary with the embrace over a single period. This indicates that the mechanically modulated (0, 48) and (−8, 8) components at these orders are formed by the superposition of contributions originating from the original components at the same orders and from higher-order components, both being modulated to these orders through the first harmonic of the tooth modulation function.

However, since the (−8, 8) component itself is a relatively strong diagonal component in the original air-gap spectrum, the modulated amplitude is dominated by the original (−8, 8) component. Moreover, because the zeroth-order coefficient of the tooth modulation function satisfies $M_0 = \text{embrace}$ and the embrace of this machine is relatively small (embrace = 0.76), the absolute amplitude of this harmonic is effectively reduced after modulation.

In contrast, the (0, 48) harmonic is not a dominant component in the original air-gap spectrum. The modulation effect transfers the diagonal harmonic (−48, 48) to this order, and since the embrace of this machine (embrace = 0.76) lies in the range where the first harmonic coefficient M_1 of the tooth modulation function has a relatively large magnitude, the (0, 48) component is significantly amplified. Furthermore, because its spatial order is zero, this harmonic can have a considerable impact on the vibration behavior of the machine.

By further examining Fig. 5.29(b) and Fig. 5.29(d), it can be observed that the normalized relative amplitude of the (0, 48) harmonic after mechanical modulation is consistently amplified, indicating that this harmonic is significantly enhanced by the tooth modulation effect.

Moreover, by comparing Fig. 5.29(a) and Fig. 5.29(b) with Fig. 5.29(c) and Fig. 5.29(d), it is found that, in the 8p48s machine, the effects of the modulation of distributed force and sampling of concentrated force are nearly equivalent, both in terms of the absolute amplitudes and the normalized relative amplitudes. This behavior can be explained by the fact that, when the number of stator teeth is sufficiently large, the tooth pitch becomes small and the distributed forces acting on each tooth tend to approach concentrated forces. As a result, the mechanical modulation effect of

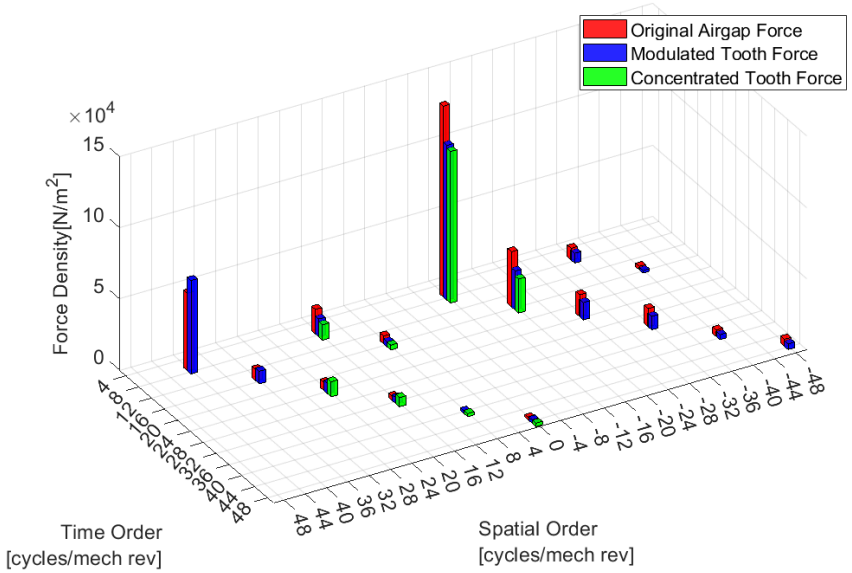

(a) Harmonic components in 8p48s motor

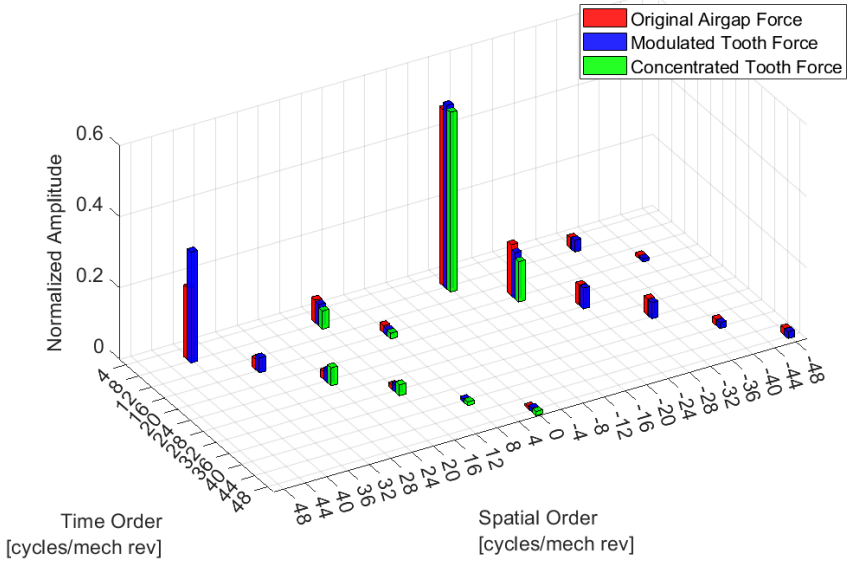

(b) Normalized harmonic components in 8p48s motor

Figure 5.28: Spatial and Temporal harmonics of air-gap and tooth force density in 8p48s motor@embrace=0.76

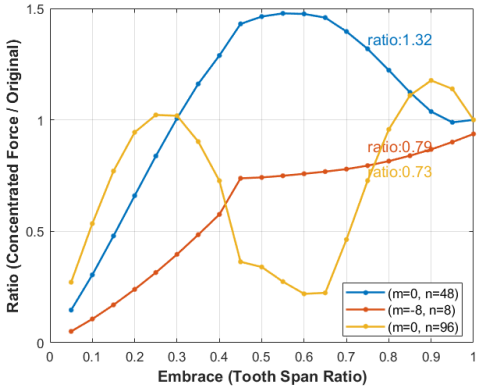

(a) Ratio between Concentrated and Original force varying with embrace in 8p48s motor

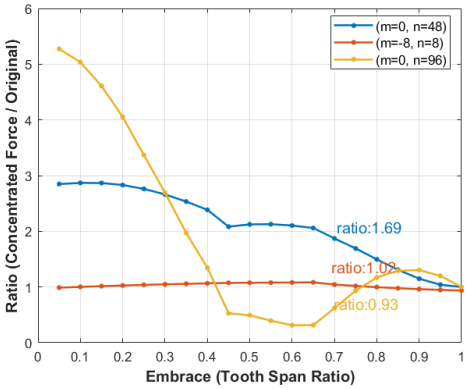

(b) Ratio between Normalized Concentrated and Original force varying with embrace in 8p48s motor

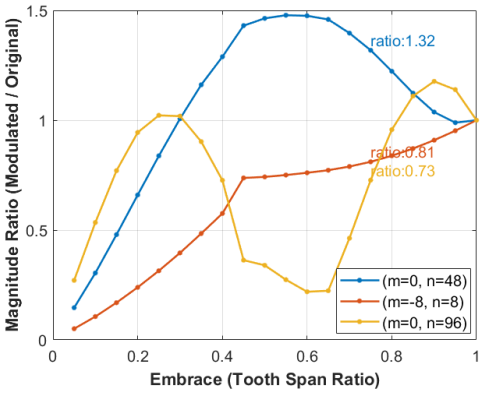

(c) Ratio between Modulated and Original force varying with embrace in 8p48s motor

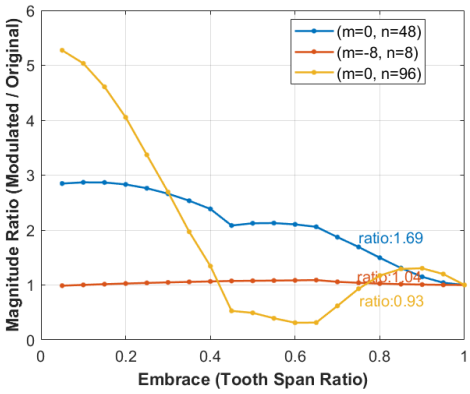

(d) Ratio between Normalized Modulated and Original force varying with embrace in 8p48s motor

Figure 5.29: Ratio between tooth and air-gap force varying with tooth embrace in 8p48s motor

the stator teeth exhibits a stronger sampling characteristic, and low-order spatial harmonics are more likely to be amplified.

5.5.6 Summary of tooth mechanical modulation effect

In summary, among the machines investigated in this study, the 8p48s machine is more strongly affected by the mechanical modulation of the air-gap electromagnetic forces introduced by the stator teeth, compared with the 8p12s and 10p12s machines. Consequently, the dominant low-order electromagnetic forces and the resulting mechanically forced vibrations in this machine are more likely to originate from the mechanical modulation effects of the stator teeth. The underlying reasons for this behavior can be summarized as follows.

First, the difference is partially determined by the original distribution of the air-gap electromagnetic force spectrum. In the 8p12s and 10p12s machines, the dominant low-order harmonics already possess relatively large amplitudes in the air-gap force spectrum. In contrast, the (0, 48) harmonic in the 8p48s machine is originally weak in the air-gap spectrum and is therefore more susceptible to enhancement through mechanical modulation.

Second, the numbers of stator teeth in the 8p12s and 10p12s machines are significantly smaller than that in the 8p48s machine. As a result, during the mechanical modulation process, the low-order harmonics in the former machines are predominantly influenced by the modulation effect associated with distributed stator tooth forces. In the 8p48s machine, however, the mechanical modulation behavior is more strongly characterized by the sampling effect of the tooth-concentrated forces, which leads to a more pronounced amplification of low-order harmonic components.

Third, both the 8p12s and 10p12s machines have stator tooth embraces close to 1, which substantially attenuates the amplitudes of the low-order harmonics of the tooth modulation function and thereby weakens the modulation effect. In contrast, the stator tooth embrace of the 8p48s machine is 0.76, which is more favorable for modulating adjacent higher-order components and transferring their energy to lower-order harmonics.

5.6 Results of Modal analysis

The modal analysis results of the stator and the housing for the three machines are shown in Fig. 5.30 and Fig. 5.31.

Since the stators of the 8p12s and 10p12s machines share identical geometric dimensions, only one of them is analyzed in detail. It can be observed that, compared with the SPM machine, the IPM machine has larger geometric dimensions and higher mass, which results in lower natural frequencies for all modal orders.

For a given structural model, the natural frequencies of the non-zero-order modes increase with increasing mode order. In contrast, the zero-order modes generally

exhibit higher natural frequencies than other modes.

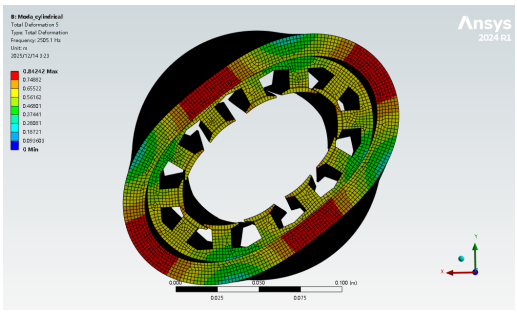

(a) 2*nd* mode, 2505.1 Hz

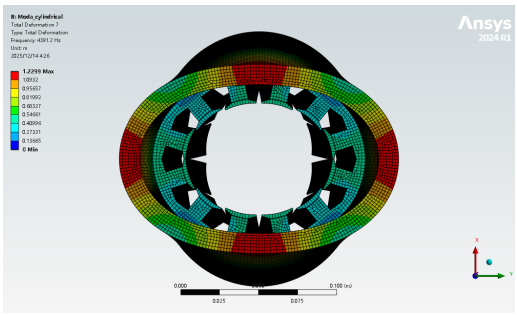

(b) 2*nd* mode, 4391.2 Hz

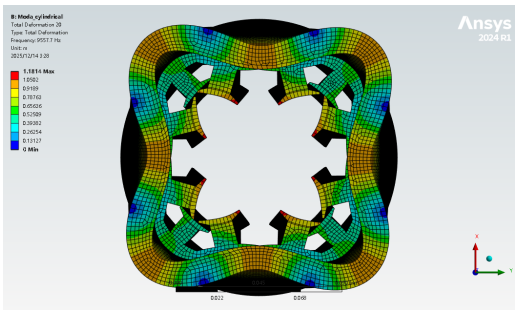

(c) 4*th* mode, 9557.7 Hz

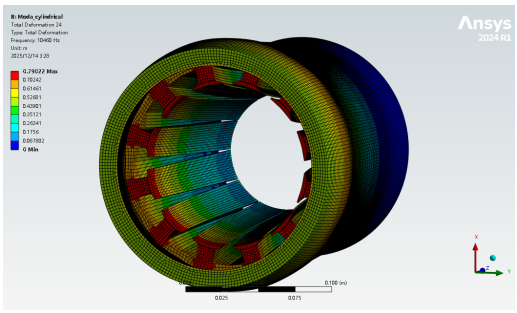

(d) 0*th* mode, 10460 Hz

Figure 5.30: Mode shapes of SPM and Natural frequency

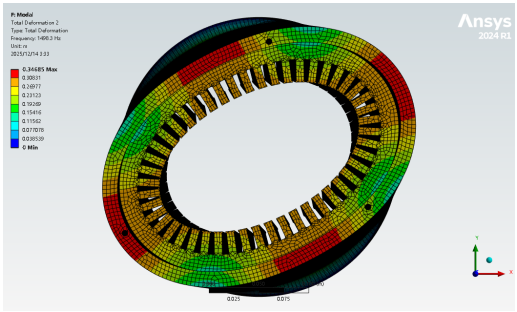

(a) 2*nd* mode, 1498.3 Hz

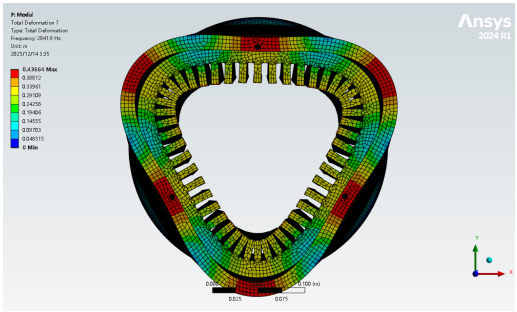

(b) 3*rd* mode, 2841.9 Hz

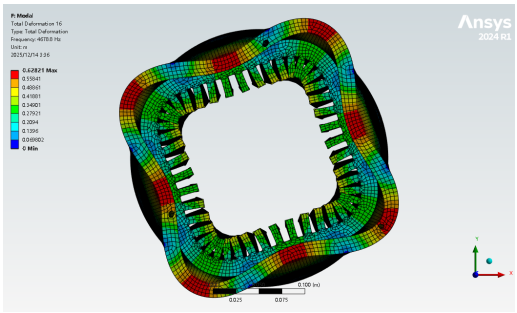

(c) 4*th* mode, 4678.8 Hz

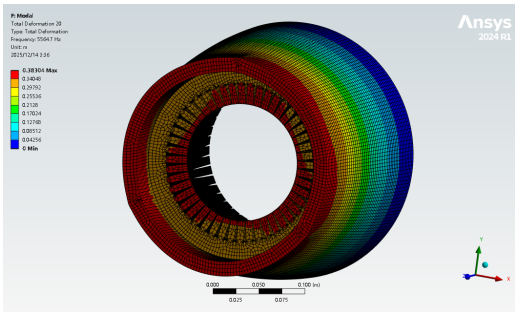

(d) 0*th* mode, 5564.7 Hz

Figure 5.31: Mode shapes of IPM and Natural frequency

5.7 Vibration analysis

In this section, a harmonic response analysis is conducted to investigate the vibration and noise induced by electromagnetic excitation. The magnitude of vibro-acoustic response is evaluated using the equivalent radiated power (ERP).

ERP represents the rate at which a vibrating structure injects acoustic energy into the surrounding air, it enables a quantitative characterization of the actual contributions of vibrations at different frequencies and circumferential orders to structural noise, without relying on explicit sound-field modeling. ERP provides an intuitive representation of the vibration energy associated with different frequencies from the perspective of the vibration source, while the ERP Level, as its logarithmic representation, is more consistent with the human auditory perception of noise.

5.7.1 Harmonic response of 8p12s motor

Fig. 5.32 illustrates the harmonic response of the outer surface of the housing of the 8p12s motor under load conditions over the entire operating speed range, expressed in terms of the ERP Level. Fig. 5.33 presents a detailed view of the ERP and ERP Level at a rotational speed of 2000 rpm.
Fig. 5.32 indicates that the vibro-acoustic response is mainly concentrated at the 8th, 16th, 24th, and other temporal orders corresponding to multiples of $2k_p$, which is consistent with the electromagnetic force model. From Fig. 5.33(a) the maximum erp and erp level is observed at the 8th temporal order, corresponding to the $(-4, 8)$ stator tooth force component identified in Section 5.5. This suggests that the 8th temporal-order response is primarily dominated by the $(-4, 8)$ spatio-temporal tooth force, while tooth force components associated with higher spatial orders at the same temporal order also contribute to the response.

According to the analysis presented in Section 5.5, the lowest spatial order of the electromagnetic force in this machine is 4, which is relatively high. The natural frequency of the structural mode corresponding to this spatial order is 9557.7 Hz, representing the lowest frequency at which resonance could potentially occur in the motor, as the natural frequencies associated with zero-order or higher spatial-order modes are even higher. Due to the limitations imposed by the operating speed range and the sampling frequency, no electromagnetic force component with the corresponding spatio-temporal order intersects this natural frequency throughout the entire operating range. Consequently, no resonance is observed within the investigated speed range.

As a result, the relatively large ERP Level responses are predominantly distributed at lower temporal orders, namely the multiples of $2k_p$, rather than being associated with structural resonances.

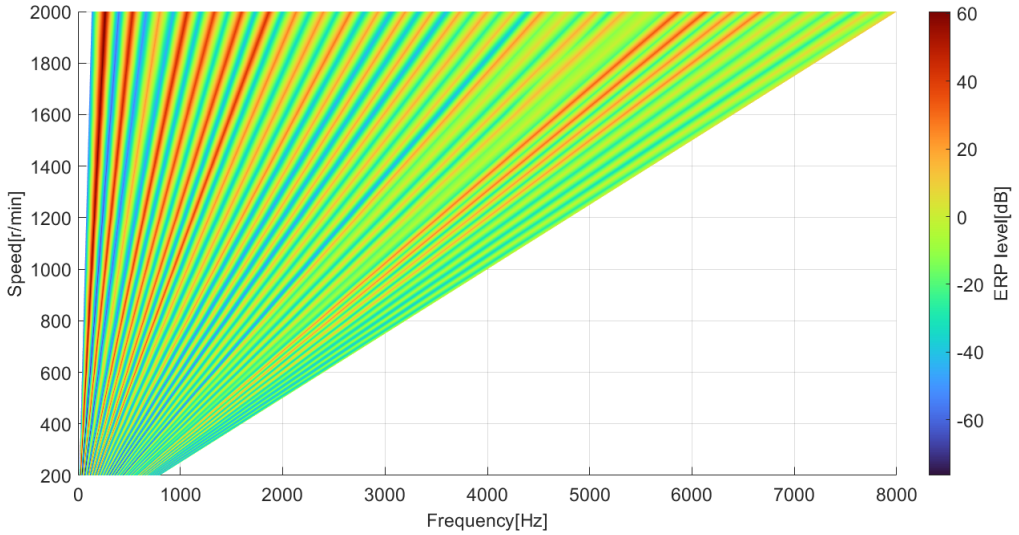

Figure 5.32: Waterfall plot of ERP level for 8p12s @34.9A

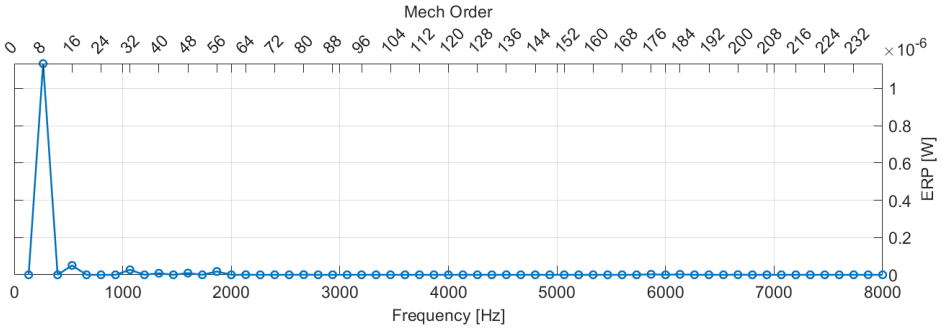

(a) ERP @2000rpm

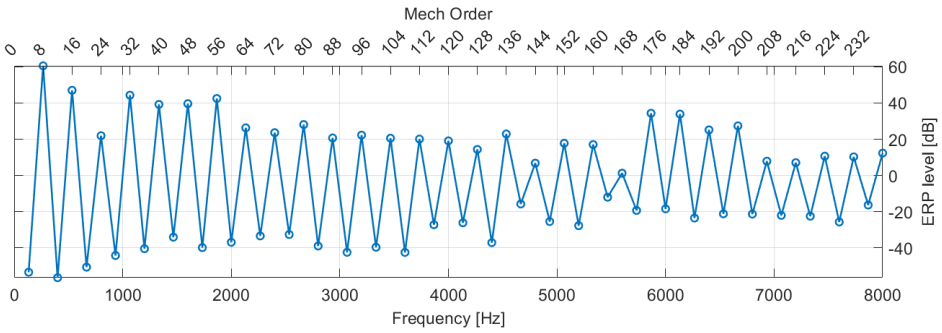

(b) ERP level @2000rpm

Figure 5.33: ERP and ERP level of 8p12s @34.9A

5.7.2 Harmonic response of 10p12s motor

Fig. 5.34 illustrates the harmonic response of the outer surface of the housing of the 10p12s motor under load conditions over the entire operating speed range, expressed in terms of the ERP Level. Fig. 5.35 presents the ERP and ERP Level at rotational speeds of 200 rpm and 2000 rpm, respectively.

Fig. 5.34 shows that, under load conditions, the harmonic response of the motor is still mainly distributed at the temporal orders of 10, 20, 30, and other multiples of $2k_p$. However, the responses at the 10th, 70th, and 130th temporal orders exhibit significantly higher amplitudes at certain operating speeds.

As shown in Fig. 5.35(a), when the rotational speed is 200 rpm, only the 10th temporal-order response is pronounced, corresponding to the (2, 10) spatio-temporal component of the stator tooth force. At this low speed, the excitation frequency does not intersect the natural frequency of the second spatial-order mode, and therefore no resonance occurs.

Further observations from Fig. 5.35(c) and (d) indicate that, at a rotational speed of 2000 rpm, the harmonic responses at the 10th, 70th, and 130th temporal orders all become significant. The frequencies corresponding to the 70th and 130th temporal orders are 2333 Hz and 4333 Hz, respectively. According to the modal analysis results, these frequencies are located in the vicinity of the second spatial-order natural frequencies at 2505.1 Hz and 4391.2 Hz. This demonstrates that the spatio-temporal stator tooth force components (2, 70) and (2, 130) excite resonant responses of the same structural mode. The maximum ERP Level reaches 80 dB, indicating a significant contribution of this resonant response to the vibration and noise performance of the motor.

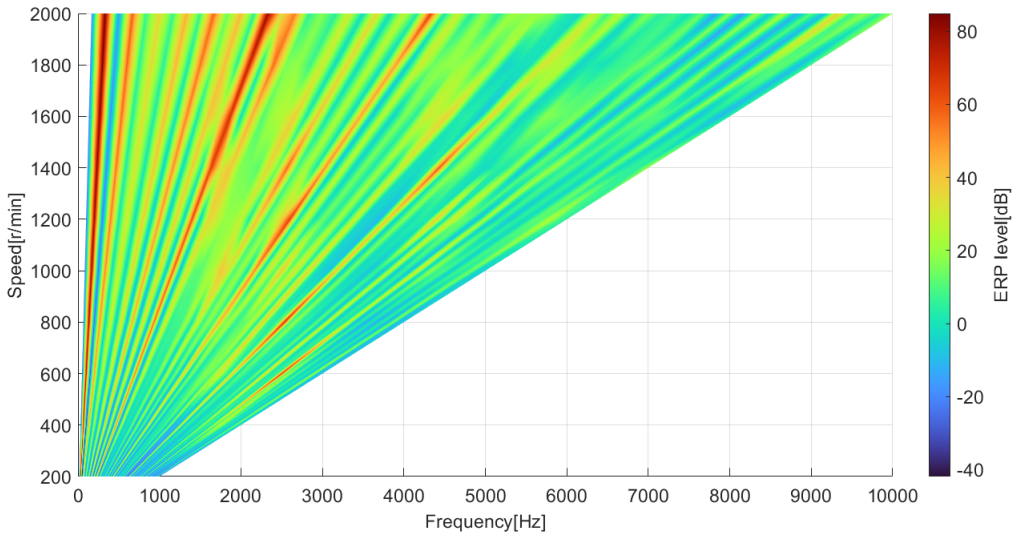

Figure 5.34: Waterfall plot of ERP level for 10p12s @34.9A

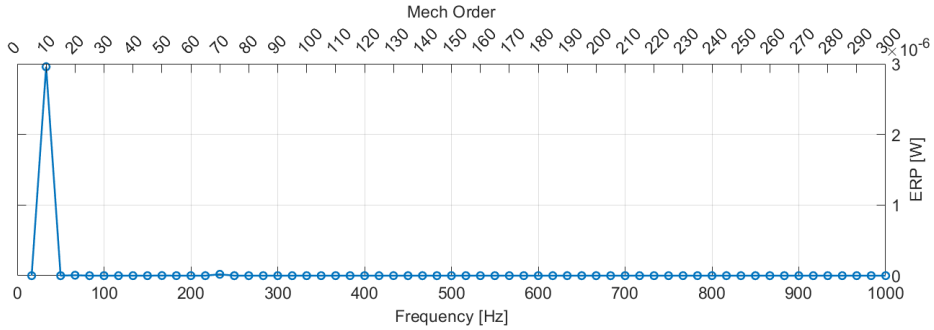

(a) ERP @200rpm

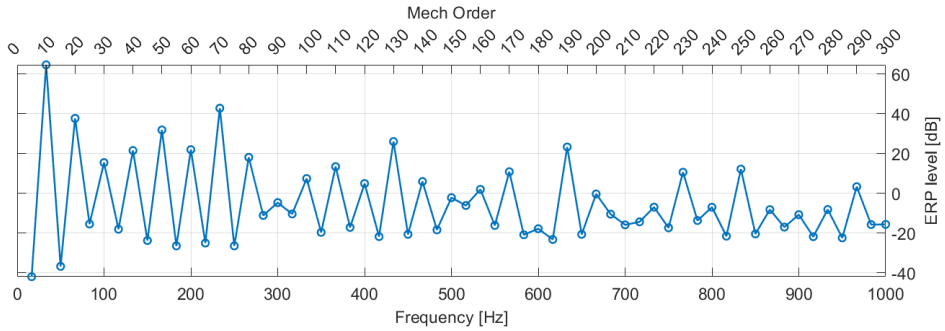

(b) ERP level @200rpm

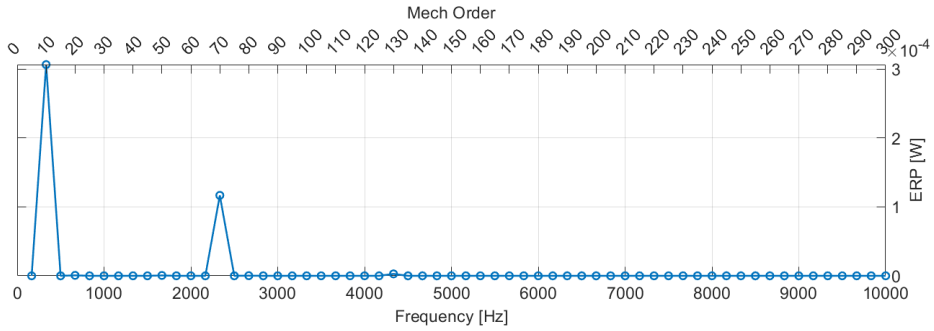

(c) ERP @2000rpm

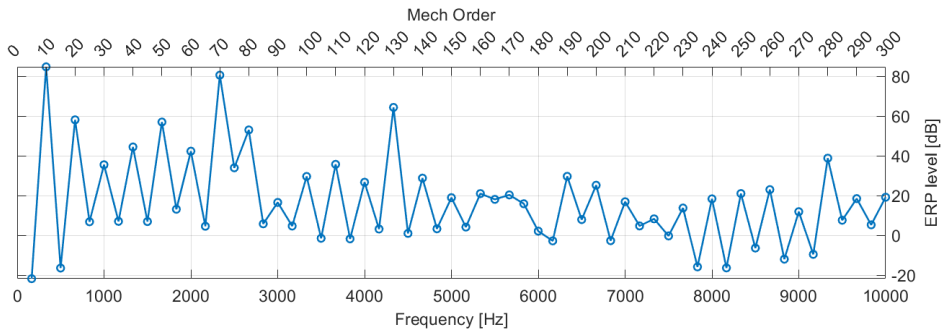

(d) ERP level @2000rpm

Figure 5.35: ERP and ERP level of 10p12s @34.9A

These results indicate that, due to the presence of lower spatial-order vibration modes, the motor is more likely to experience resonance when operating at low

speeds, as the corresponding temporal orders intersect the natural frequencies of these modes. Lower spatial orders not only lead to larger electromagnetic force amplitudes, but also increase the likelihood of resonance, thereby significantly increasing the ERP and adversely affecting the vibration and noise performance of the motor.

5.7.3 Harmonic response of 8p48s motor

Fig. 5.36 shows that the harmonic response of the motor is still mainly distributed at the 8th, 16th, and 48th temporal orders, corresponding to multiples of $2k_p$. Among them, the 48th temporal-order response exhibits relatively larger amplitudes at certain frequencies under high-speed operating conditions.

As shown in Fig. 5.37, when the rotational speed is 500 rpm, the harmonic responses at the 8th, 16th, and 48th temporal orders are all pronounced, corresponding to the $(-8, 8)$, $(8, 16)$, and $(0, 48)$ spatio-temporal components of the stator tooth force, respectively. At this low speed, the excitation frequencies do not intersect any structural natural frequencies, and therefore no resonance occurs. Under this condition, the harmonic response is mainly governed by the magnitude of the stator tooth forces and their spatial modes, rather than by the natural frequencies of the structure.

It is noteworthy that the pronounced response associated with the $(0, 48)$ spatio-temporal component is somewhat unexpected. Although zero spatial-order electromagnetic force components are also present in the other two motors, they do not constitute dominant vibration sources. For the 8p48s motor, however, the $(0, 48)$ stator tooth force component is significantly amplified due to the mechanical tooth modulation effect, thereby becoming one of the primary vibration excitation sources of the motor.

Fig. 5.38 shows that, when the rotational speed reaches 7000 rpm, the harmonic response at the 48th temporal order becomes particularly pronounced. The corresponding frequency is 5600 Hz. According to the modal analysis results, this frequency is located in the vicinity of the zero spatial-order natural frequency of the structure at 5564.7 Hz, indicating that the observed harmonic response is caused by resonance excitation of the zero spatial-order mode induced by the $(0, 48)$ spatio-temporal component of the stator tooth force. Under this condition, the ERP Level reaches 85 dB, demonstrating that the resonance significantly enhances the acoustic energy radiated by the structure. These results indicate that, with increasing rotational speed, the zero spatial-order electromagnetic force reaches its corresponding resonant frequency earlier than higher spatial-order forces (e.g., the 8th spatial order), since the natural frequency of the zero-order mode is lower. This further confirms that the zero spatial-order electromagnetic force is the dominant excitation source of vibration and noise in this motor in the speed range of 0–8000 rpm.

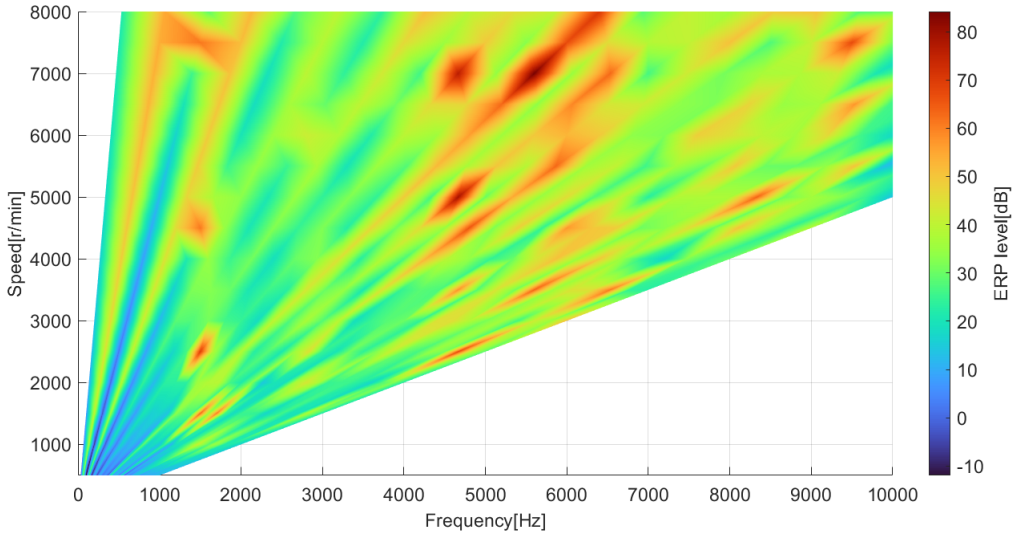

Figure 5.36: Waterfall plot of ERP level for 8p48s@100A

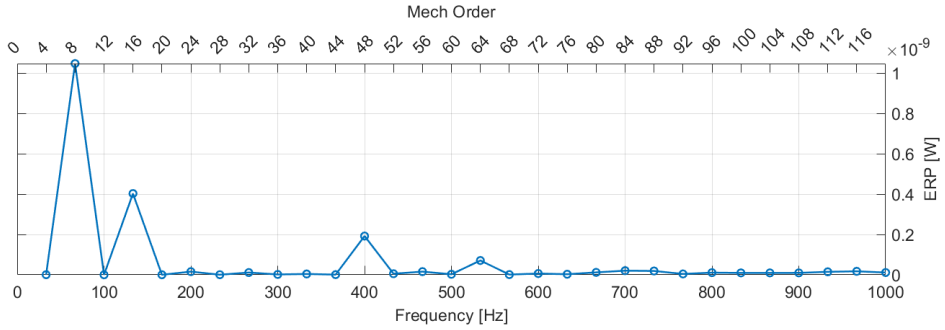

(a) ERP @500rpm

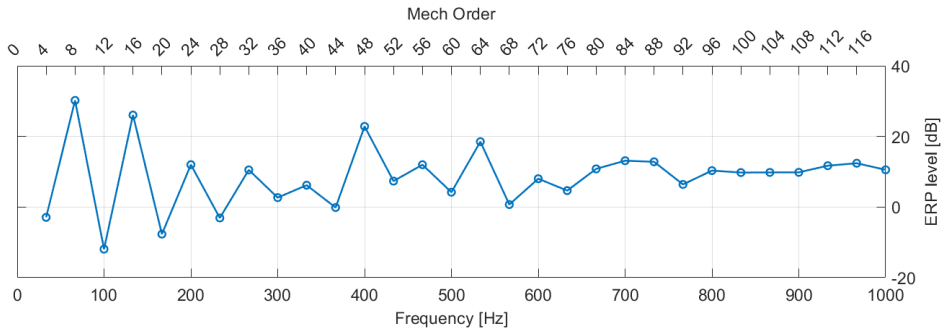

(b) ERP level @500rpm

Figure 5.37: ERP and ERP level of 8p48s @100A

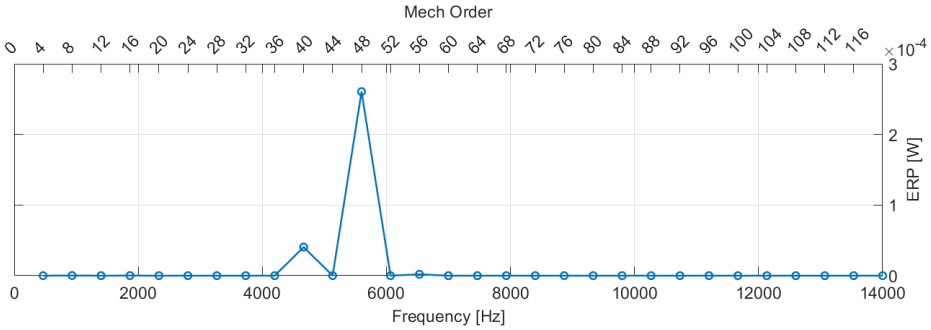

(a) ERP @7000rpm

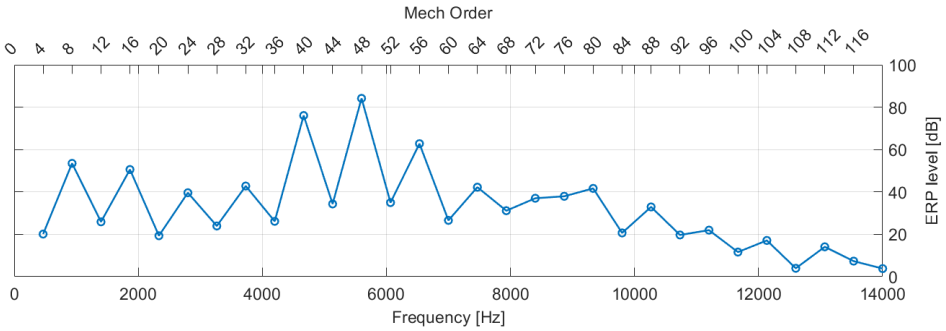

(b) ERP level @7000rpm

Figure 5.38: ERP and ERP level of 8p48s @100A

5.7.4 Summary of the harmonic response analysis

In this section, the predictions presented in previous sections are validated from the perspective of the vibration radiated energy (ERP) on the outer surface of the housing and its corresponding noise indicator, the ERP Level. The results demonstrate that the (4, 8), (2, 10), and (0, 48) spatio-temporal harmonic components in the stator tooth force spectra become the dominant sources of vibration and noise in the 8p12s, 10p12s, and 8p48s motors, respectively, thereby confirming the validity of the air-gap electromagnetic force model and the tooth modulation model.

In addition, the results further reveal the potential influence of structural modes on vibration and noise over the entire operating speed range. As the rotational speed varies, resonance is induced when the frequencies of the stator tooth force harmonics intersect the natural frequency of the same structural mode, leading to a significant amplification of vibration response and noise radiation.

6

Conclusion and Future work

6.1 Conclusion

This thesis presents a systematic analytical and numerical investigation of electromagnetic tooth forces in permanent magnet synchronous machines (PMSMs) with different pole–slot combinations. By establishing unified analytical models for air-gap flux density, electromagnetic force generation, and force transmission, and by combining finite-element-based vibration and harmonic response analyses, the influence of pole–slot combinations on air-gap magnetic fields, electromagnetic force harmonics, torque ripple, and vibro-acoustic characteristics is comprehensively examined. The physical process through which electromagnetic forces are generated, modulated, and ultimately transformed into vibration and noise is fully elucidated. The main conclusions are summarized as follows.

Magnetic field analysis shows that differences in electromagnetic force harmonics among machines are mainly determined by the armature reaction magnetic fields in the air gap. Fractional-slot machines exhibit richer spatial harmonic contents in the winding field. In particular, low-order electromagnetic force waves formed by the interaction between the PM fundamental flux and low-order non-fundamental winding flux components—such as the $(4, 8)$ component in the 8p12s machine and the $(2, 10)$ component in the 10p12s machine—dominate the vibration behavior of these machines. For distributed-winding machines, the lowest non-zero electromagnetic force component arises from the interaction between the PM fundamental flux and the winding fundamental flux, i.e., the $(2p, 2p)$ component. Although its amplitude is relatively large, its spatial order is generally high, which weakens its contribution to vibration. In addition, when stator slotting is considered, spatial modulation is introduced without affecting the temporal harmonic orders.

A major contribution of this work is the systematic analysis of the mechanical modulation effect of stator teeth during the transmission of air-gap electromagnetic forces to tooth forces. The results demonstrate that this modulation process can significantly reshape the force spectrum, with varying impacts across different machines. Among the investigated machines, the 8p48s machine is most strongly affected due to its larger number of stator teeth, smaller tooth pitch, and lower tooth embrace. In this machine, tooth forces exhibit a pronounced "sampling effect," which significantly amplifies low-order spatial harmonics, especially the $(0, 48)$ component that is weak in the air-gap force spectrum. In contrast, the 8p12s and 10p12s machines are dominated by distributed tooth forces, and their tooth embraces close to unity ef-

fectively suppress low-order modulation effects. Moreover, the relative relationships among air-gap force components induced by pole–slot combinations also influence the effectiveness of the modulation process.

Modal and harmonic response analyses indicate that the vibration and noise characteristics of the machine are governed by the interaction between dominant stator tooth force harmonics and the structural modes of the stator–housing assembly. The presence of resonance can significantly alter the vibration and noise patterns of the machine. In distributed-winding machines, stator tooth modulation shifts the dominant excitation from the $(8, 8)$ force component to a higher-order zero-mode force component $(0, 48)$, which makes the machine more prone to resonance compared with the unmodulated case. In fractional-slot concentrated winding machines, vibration is dominated by the lowest non-zero spatial-order force component. Owing to its smaller non-zero spatial order, the 10p12s machine is more susceptible to resonance than the 8p12s machine.

In summary, this study establishes a clear physical link from air-gap flux density and electromagnetic forces, through mechanical modulation by stator teeth, to torque ripple, structural vibration, and noise radiation. The results demonstrate that both directly generated low-order spatial electromagnetic forces and low-order spatial components indirectly introduced by stator tooth mechanical modulation are key factors governing the vibro-acoustic performance of electrical machines.

6.2 Future Work

Based on the results of this thesis, the following topics are identified as potential directions for future research:

- **Rotor topology effects:** A systematic comparison between interior permanent-magnet (IPM) and surface-mounted permanent-magnet (SPM) machines should be conducted, with particular emphasis on the influence of flux barriers, magnetic saturation, and spatial shifts between rotor magnetic fields and stator slotting on electromagnetic force spectra and force transmission mechanisms.
- **Vibration and noise comparison under equal torque:** Vibration and noise levels of different pole–slot combinations and machine topologies should be compared under identical torque conditions, enabling a fair assessment of vibro-acoustic performance independent of torque-dependent operating points.
- **Influence of current harmonics:** The effect of current harmonics introduced by pulse-width modulation (PWM) has not been considered in this work. Future studies could investigate how inverter-fed excitation and high-frequency current harmonics affect electromagnetic forces and vibro-acoustic behavior.
- **Role of tangential forces:** While this thesis focuses mainly on radial electromagnetic forces, the contribution of tangential force components to structural vibration and noise generation should be investigated to achieve a more complete understanding of excitation mechanisms.

Bibliography

[1] S. Zhu, W. Zhao, J. Ji, G. Liu, and C. H. T. Lee, "Generation mechanism and suppression measure of electromagnetic vibration in permanent magnet synchronous machine: A review," *IEEE Transactions on Transportation Electrification*, vol. 10, no. 4, pp. 9513–9534, 2024.

[2] H. Jordan, *Geraüscharme Elektromotoren*. Essen, Germany: Verlag W. Giradet, 1950.

[3] A. Hofmann, F. Qi, T. Lange, and R. W. De Doncker, "The breathing mode-shape 0: Is it the main acoustic issue in the pmsms of today's electric vehicles?," *Proceedings of the International Conference on Electrical Machines and Systems (ICEMS)*, pp. 1–7, 2014.

[4] Z. Q. Zhu, D. Howe, E. Bolte, and B. Ackermann, "Instantaneous magnetic field distribution in brushless permanent magnet dc motors, part i: Open-circuit field," *IEEE Transactions on Magnetics*, vol. 29, no. 1, pp. 124–135, 1993.

[5] Z. Q. Zhu, D. Howe, and C. C. Chan, "Instantaneous magnetic field distribution in brushless permanent magnet dc motors, part ii: Armature-reaction field," *IEEE Transactions on Magnetics*, vol. 29, no. 1, pp. 136–142, 1993.

[6] Z. Q. Zhu and D. Howe, "Instantaneous magnetic field distribution in brushless permanent magnet dc motors, part iii: Effect of stator slotting," *IEEE Transactions on Magnetics*, vol. 29, no. 1, pp. 143–151, 1993.

[7] Z. Q. Zhu and D. Howe, "Instantaneous magnetic field distribution in brushless permanent magnet dc motors, part iv: Magnetic field on load," *IEEE Transactions on Magnetics*, vol. 30, no. 1, pp. 152–159, 1994.

[8] D. Zarko, D. Ban, and T. A. Lipo, "Analytical calculation of magnetic field distribution in the slotted air gap of a surface permanent-magnet motor using complex relative air-gap permeance," *IEEE Transactions on Magnetics*, vol. 42, no. 7, pp. 1828–1837, 2006.

[9] A. M. El-Refaie, "Fractional-slot concentrated-windings synchronous permanent magnet machines: Opportunities and challenges," *IEEE Transactions on Industrial Electronics*, vol. 57, no. 1, pp. 107–121, 2010.

[10] H. Fang, D. Li, R. Qu, and P. Yan, "Modulation effect of slotted structure on vibration response in electrical machines," *IEEE Transactions on Industrial Electronics*, vol. 66, no. 4, pp. 2998–3007, 2019.

[11] W. Liang, J. Wang, P. C. K. Luk, and W. Fei, "Analytical study of stator tooth modulation on electromagnetic radial force in permanent magnet synchronous machines," *IEEE Transactions on Industrial Electronics*, vol. 68, no. 12, pp. 11731–11740, 2021.

[12] H. Fang, D. Li, J. Guo, Y. Xu, and R. Qu, "Hybrid model for electromagnetic vibration synthesis of electrical machines considering tooth modulation and tangential effects," *IEEE Transactions on Industrial Electronics*, vol. 68, no. 8, pp. 7284–7295, 2021.

DEPARTMENT OF SOME SUBJECT OR TECHNOLOGY
CHALMERS UNIVERSITY OF TECHNOLOGY
Gothenburg, Sweden
www.chalmers.se

CHALMERS
UNIVERSITY OF TECHNOLOGY